UNIVERSITEIT VAN PRETORIA
UNIVERSITY OF PRETORIA
YUNIBESITHI YA PRETORIA

IN-SITU ALLOYING OF AISI 410L MARTENSITIC STAINLESS STEEL WITH NITROGEN DURING LASER CLADDING

by

Cornelis Janse van Niekerk

Submitted in partial fulfillment of the requirements for the degree

Master of Engineering (Metallurgical)

in the Faculty of Engineering, the Built Environment and Information Technology, University of Pretoria

January 2016

ACKNOWLEDGEMENTS

For my supervisor and mentor, Professor Madeleine du Toit, I have the highest praise. Her optimism, insights and dedication to excellence guided this work to completion. I want to thank her for her patience, sharing her vast knowledge and experience to overcome the inevitable obstacles of research, and her compassionate approach in creating an environment for progress.

Professor Pieter Pistorius also has my gratitude in seeing this work through its final stages of completion. His insights and experience added significant value to the work. I want to thank him for making countless arrangements (both practical and administrative), support, communications and endless patience.

I want to thank Corney van Rooyen for his exceptional supervision of my work at the National Laser Centre of the CSIR. I want to thank him also for sharing his knowledge and experience in steering this work in the appropriate direction. His humility and willingness to guide, teach, and assist (beyond what was expected) was the fuel that drove this work forward.

Herman Burger, Maritha Theron, and Herman Rossouw at the NLC (CSIR) also deserve my gratitude and acknowledgement. Their general advice, support, sharing of experience, and friendship made every day of work at the NLC a joy and a privilege. Thank you.

To my good friend Markus Erwee, I owe a large debt of gratitude for his endless support. I want to thank him for his assistance and insights in the use of the Thermocalc™ software used in this study. He is also an incomparable source of inspiration and a true and valued friend. Thank you.

I want to thank Sarah Havenga for her support in an all-encompassing capacity. She was a rock and a steady anchor in often turbulent waters and her friendship and advice on a daily basis gave me the encouragement needed to complete any task.

To the most important people in my life, my parents, Cornelia and Oostewald van Niekerk, I want to dedicate this work. A mere thank you could never suffice for the love, support, and sacrifices on your part. In who I am and who I hope to become, I strive only to make you proud and wish you to be happy.

> “I am become a name; for always roaming with a hungry heart
> Much have I seen and known; myself not least, but honour’d of them all.
> I am a part of all that I have met; yet all experience is an arch wherethro’
> Gleams that untravell’d world whose margin fades for ever and forever when I move.
> How dull it is to pause, to make an end, to rust unburnishe’d, not to shine in use!
> As tho’ to breathe were life! Life piled on life
> Were all too little, and of one to me little remains: but every hour is saved
> From that eternal silence, something more, a bringer of new things;
> And this grey spirit yearning in desire to follow knowledge like a sinking star,
> Beyond the utmost bound of human thought.” — Lord Alfred Tennyson (Ulysses)

ABSTRACT

The feasibility of *in-situ* alloying of AISI 410L martensitic stainless steel with nitrogen during Nd-YAG laser cladding was investigated with the aim of achieving a nitrogen content of at least 0.08 wt% and fully martensitic microstructures in the final clad deposit. Two *in-situ* nitrogen alloying techniques were studied.

In the first set of experiments, the absorption of nitrogen from nitrogen-rich gas atmospheres was studied. Laser cladding with commercially available AISI 410L powder was performed using nitrogen-rich shielding and carrier gas. A marginal increase in deposit nitrogen content was observed, with the clad deposit displaying low hardness and mostly ferritic microstructures. Poor nitrogen absorption from nitrogen-containing atmospheres during Nd-YAG laser cladding is generally attributed to the short thermal cycle and to suppression of plasma formation above the weld pool.

In the remaining experiments, Si_3N_4 powder was investigated as an alternative source for nitrogen during cladding. The addition of Si_3N_4 to the AISI 410L powder feed resulted in clad microstructures consisted of columnar δ-ferrite grains with martensite on the grain boundaries, higher hardness and an increase in deposit nitrogen content (to a maximum of 0.064 wt% nitrogen). Higher nitrogen contents in the clad deposit, however, significantly increased the volume percentage porosity in the clad layer. This prompted an investigation into the feasibility of raising the nitrogen solubility of the alloy through additions of manganese and nickel to the powder feed.

Thermodynamic modelling revealed that the addition of manganese to AISI 410L powder increases the nitrogen solubility limit due to its negative interaction parameter with nitrogen. The addition of up to 3.5 wt% manganese to AISI 410L powder containing Si_3N_4 significantly increased the nitrogen solubility in the deposit. A martensitic microstructure with 0.12 wt% nitrogen and a peak hardness of 410 HV was achieved without any adverse increase in porosity in the clad layer. The clad nitrogen content easily exceeded the minimum requirement of 0.08 wt%.

High nickel concentrations in AISI 410L stainless steel expand the austenite phase field at the expense of δ-ferrite and alter the solidification mode from ferritic to austenitic-ferritic. The addition of up to 5.5 wt% nickel, or combinations of nickel and manganese, to the nitrogen-alloyed AISI 410L powder feed raised the deposit nitrogen content, but not to the same extent as those deposits alloyed with manganese only. Since more austenite is present on cooling in nickel-alloyed AISI 410L deposits, less nitrogen is rejected to the liquid phase on solidification, resulting in higher nitrogen contents and less porosity in the room temperature microstructures.

The amount of dilution during single-track laser cladding is mainly influenced by the specific energy per unit mass delivered by the laser beam. The clad height is strongly influenced by the powder deposition rate, whereas the bead width is influenced by the wettability of the deposits during laser cladding. During multi-track cladding, the observed percentage porosity is a function of the aspect ratio of the individual beads

making up the clad layer, the deposition rate and the clad height. High deposition rates result in thicker layers, increasing the distance that N_2 gas bubbles have to travel to escape to the atmosphere, while a high aspect ratio favours interbead porosity. The results suggest that *in-situ* nitrogen alloying during laser cladding should preferably be performed at low deposition rates to ensure higher clad nitrogen contents and hardness, lower clad heights, less dilution and less porosity.

KEYWORDS

Laser cladding; martensitic stainless steels; nitrogen; solubility.

TABLE OF CONTENTS

CHAPTER 1

BACKGROUND

1.1 INTRODUCTION

Laser powder cladding with martensitic stainless steel provides a fast and cost effective method of improving the hardness, wear resistance and corrosion resistance of a carbon steel substrate. During laser cladding a thin layer of hard, wear resistant martensitic stainless steel is deposited on the substrate with little distortion and minimal thermal damage to the underlying material. This method also finds application in the repair of martensitic stainless steel components with tight dimensional tolerances [1-3].

The rapid cooling rates associated with laser cladding may, however, suppress the formation of austenite on cooling, resulting in excessive ferrite contents in the clad layer, or depress the M_s (martensite start) temperature to such an extent that high levels of retained austenite are present in the surface deposit [4-8]. To obtain fully martensitic deposits after cladding, modification of the chemistry of the martensitic stainless steel may be required. Alloying with nitrogen holds considerable promise in this regard. Nitrogen is not only a strong austenite-former, expanding the austenite phase field on cooling and promoting the formation of austenite even at high cooling rates, but it also improves hardness, strength and pitting corrosion resistance when dissolved interstitially in the martensitic stainless steel matrix [7-9].

The *in-situ* alloying of martensitic stainless steel with nitrogen during laser cladding is therefore likely to increase the hardness, wear resistance and corrosion resistance of the deposited layer, while also improving the likelihood of obtaining a fully martensitic microstructure after cladding. This study therefore investigated the *in-situ* alloying of AISI 410L low-carbon martensitic stainless steel with nitrogen during laser cladding.

Various methods of introducing nitrogen during laser welding and cladding processes have been considered to date. Published research [10-12] shows that laser welding of pure iron and stainless steel in nitrogen-rich Ar-N_2 gas mixtures promotes considerably less nitrogen dissolution in the weld metal than during arc welding in nitrogen-containing shielding gas mixtures. This can be attributed to the short thermal cycle during laser welding not allowing enough time for nitrogen absorption from the atmosphere. In addition, a highly concentrated metallic vapour forms above the weld pool during laser processing, delaying nitrogen absorption. An additional drawback of welding and cladding with a Nd:YAG laser, as opposed to a CO_2 laser, is its short wavelength. During arc and CO_2 laser welding and cladding operations in Ar-N_2 shielding gas mixtures, plasma with a high monatomic nitrogen content forms over the weld pool. This enhances nitrogen absorption from the atmosphere. During Nd:YAG laser welding and cladding, insufficient absorption of the laser beam occurs in the gaseous atmosphere, resulting in lower temperatures above the welding pool with only a slight probability of plasma formation.

Published literature [13-20] suggests the co-feeding of nitrided powders with stainless steel powder as an alternative technique for *in-situ* alloying of stainless steel with nitrogen during laser cladding. Silicon nitride (Si_3N_4) powder serves as an excellent source of nitrogen. The Si_3N_4 powder dissociates during the cladding process to introduce nitrogen and silicon into the clad layer. The oxidation behaviour and pitting corrosion resistance of these nitrogen-alloyed layers also show marked improvement due to the reported increase in the deposit silicon and nitrogen contents.

The benefits associated with nitrogen alloying can, however, only be realized if the nitrogen is in solid solution in the martensitic matrix. The solubility of nitrogen in ferritic and martensitic stainless steels is very low compared to that of the austenitic grades, with excess nitrogen creating porosity or precipitating as harmful nitrides [21]. Successful use of *in-situ* nitrogen alloying during laser cladding therefore requires the nitrogen to remain in solid solution in the stainless steel matrix. To increase the solubility of nitrogen in martensitic stainless steel, austenite must be present at elevated temperatures during cooling (austenite has a high solubility for nitrogen), and the steel should be alloyed with elements that have negative interaction parameters with nitrogen. The addition of manganese is known to increase the solubility limit of nitrogen in stainless steel, thereby enhancing nitrogen pick-up [21-22]. Alloying with manganese should, however, be done with care as it is known to decrease the corrosion resistance of stainless steels [23]. During the course of the investigation the addition of alloying elements to increase nitrogen solubility was therefore kept to a minimum and their effects assessed through careful design of theoretical alloy systems.

1.2 AIMS OF THE INVESTIGATION

The National Laser Centre (NLC) of the Council for Scientific and Industrial Research (CSIR) in Pretoria, South Africa, has done extensive research on the hardfacing of components with martensitic stainless steel overlays for the manufacturing, mining and paper industries. The Laser Metal Processing Group have, to date, aligned the hardfacing capabilities of the NLC to industry needs through hardfacing of components with supermartensitic stainless steels, modified to fully martensitic microstructures through the additions of molybdenum and nickel to these alloys. On-going research at the NLC focuses on improving the hardness and pitting corrosion resistance of martensitic stainless steel overlays and extending its application to the power generation and petrochemical industries.

This study, therefore, aims at extending the research conducted by the NLC in the field of laser cladding of martensitic stainless steels. It concentrates on developing a method of *in-situ* alloying of low-carbon martensitic stainless steel with nitrogen during laser cladding using the Nd:YAG laser facilities of the CSIR. In addition to the technical project objectives, which focus on the microstructure, mechanical properties and corrosion behaviour of the clad layers, several additional requirements have to be met:

- the alloying process must be simple and cost-effective,
- the alloying method must be practical and functional within the industry requirements set forth by the NLC,

- the work should contribute to the on-going research programme of the Laser Metal Processing Group of the NLC, and
- a thorough literature review should be conducted to evaluate the advantages and disadvantages of existing *in-situ* alloying techniques and to investigate the practical implementation of the preferred technique within the facilities and capabilities of the Laser Metal Processing Group of the NLC.

A detailed review of the available published literature is given in Chapter 2, while the objectives and targeted outcomes of this study are outlined in Chapter 3.

1.3 REFERENCES

[1] ASM International. *Laser surface hardening*, in ASM Handbook, Volume 4A - Steel Heat Treating Fundamentals and Processes, eds. Dossett, J.L. and Totten, G.E. ASM International, Materials Park, OH. 2013. pp. 481.

[2] Sexton, C.L., Byrne, G., Watkins, K.G. *Alloy development by laser cladding: An overview*. Journal of Laser Applications, vol. 13, no. 1. 2001. pp. 2-11.

[3] Ion, J. *Laser Processing of Engineering Materials*. Elsevier Butterworth-Heinemann, Oxford. 2005. pp. 296-326.

[4] David, S.A., Vitek, J.M., Hebble, T.L. *Effect of rapid solidification on stainless steel weld metal microstructures and its implications on the Schaeffler diagram*. Welding Journal, vol. 66, no. 10. 1987. pp. 289s-300s.

[5] Van Rooyen, C., Burger, H.P., Kazadi, B.P. *Microstructure of laser cladded martensitic stainless steel*. IIW document IX-H-636-06. International Institute of Welding, Paris. 2006.

[6] Hemmati, I., Ocelík, V., De Hosson, J.T.M. *Microstructural characterization of AISI 431 martensitic stainless steel laser-deposited coatings.* Journal of Materials Science, vol. 46, no. 10. 2011. pp. 3405-3414.

[7] Leda, H. *Nitrogen in martensitic stainless steels.* Journal of Materials Processing Technology, vol. 53, no. 1-2. 1995. pp. 263-272.

[8] Simmons, J.W. *Overview: High-nitrogen alloying of stainless steels.* Materials Science and Engineering A, vol. 207, no. 2. 1996. pp. 159-169.

[9] Hänninen, H., Romu, J., Ilola, R., Tervo, J., Laitinen, A. *Effects of processing and manufacturing of high nitrogen-containing stainless steels on their mechanical, corrosion and wear properties.* Journal of Materials Processing Technology, vol. 117, no. 3. 2001. pp. 424-430.

[10] Sato, Y., Dong, W., Kokawa, H., Kuwana, T. *Nitrogen absorption by iron and stainless steels during YAG laser welding.* Transactions of the Iron and Steel Institute of Japan, vol. 40. 2000. pp. S20-S24.

[11] Dong, W., Kokawa, H., Sato, Y.S., Tsukamoto, S. *Nitrogen absorption by iron and stainless steels during CO_2 laser welding.* Metallurgical and Materials Transactions B, vol. 34, no. 1. 2003. pp. 75-82.

[12] Dong, W., Kokawa, H., Tsukamoto, S., Sato, Y.S., Ogawa, M. *Mechanism governing nitrogen absorption by steel weld metal during laser welding.* Metallurgical and Materials Transactions B, vol. 35, no. 2. 2004. pp. 331-338.

[13] Huang, C.-C., Tsai, W.-T., Lee, J.-T. *Laser surface alloying of carbon steel with FeCrSi3N4 powders.* Scripta Metallurgica et Materialia, vol. 30, no. 11. 1994. pp. 1461-1466.

[14] Huang, C.-C., Tsai, W.-T., Lee, J.-T. *Electrochemical and surface studies on the passivity of nitrogen and molybdenum containing laser cladded alloys in 3.5 wt% NaCl solution.* Corrosion Science, vol. 37, no.5. 1995. pp. 769-780.

[15] Huang, C.-C., Tsai, W.-T., Lee, J.-T. *Effects of N and Mo on the electrochemical behavior of laser-alloyed stainless steels in a 3.5 wt.% NaCl solution.* Materials Chemistry & Physics, vol. 42, no. 4. 1995. pp. 280-284.

[16] Huang, C.-C., Tsai, W.-T., Lee, J.-T. *Microstructure and electrochemical behavior of laser treated FeCr and FeCrSiN surface alloyed layers on carbon steel.* Materials Science and Engineering A, vol. 190, no. 1-2. 1995. pp. 199-205.

[17] Huang, C.-C., Tsai, W.-T., Lee, J.-T. *Microstructure and electrochemical behavior of laser cladded Fe-Cr-Mo-Si-N surface alloys on carbon steel.* Materials Science and Engineering A, vol. 196, no. 1-2. 1995. pp. 243-248.

[18] Huang, C.-C., Tsai, W.-T., Lee, J.-T. *The effect of silicon nitride on the laser surface alloying with Fe-Cr-Si3N4 powders.* Scripta Metallurgica et Materialia, vol. 32, no. 9. 1995. pp. 1465-1470.

[19] Huang, C.-C., Tsai, W.-T., Lee, J.-T. *Surface modification of carbon steel with laser treated nitrogen-containing stainless steel layers.* Surface and Coatings Technology, vol. 79, no. 1-3. 1996. pp. 67-70.

[20] Sha, C.-K., Tsai, H.-L. *Hardfacing characteristics of S42000 stainless steel powder with added silicon nitride using a CO_2 laser.* Materials Characterization, vol. 52, no. 4-5. 2004. pp. 341-348.

[21] Lai, J.K.L., Lo, K.H., Shek, C.H. *Stainless steels: An introduction and their recent developments.* Bentham Science Publishers, Beijing. 2012, pp. 72-89.

[22] Pistorius, P.C., Du Toit, M. *Low-nickel austenitic stainless steels: Metallurgical constraints.* Proceedings of the 12th International Ferroalloys Congress (INFACON 2010), held in Helsinki, Finland, on 6-9 June 2010. pp. 911-917.

[23] Speidel, M.O. *Nitrogen containing austenitic stainless steels.* Materialwissenschaft und Werkstofftechnik, vol. 37, no. 10. 2006. pp. 875-880.

CHAPTER 2

LITERATURE REVIEW

2.1 LASER CLADDING

2.1.1 Introduction

Laser surface modification is a versatile technique for altering the properties of the surface layers of metallic components for enhanced physical and mechanical properties such as hardness, wear resistance and corrosion resistance. It finds application in a wide variety of industries and includes processes such as laser shock processing (the introduction of negative residual stresses in surface layers through hydrodynamic expansion of plasma), laser transformation hardening (the transformation of surface layers to higher hardness and wear resistance), laser remelting (the refinement of surface microstructures), laser alloying (the alteration of the chemical composition of surface layers) and laser cladding (the deposition of a functional surface layer through the fusion of consumables) [1,2]. Figure 2.1.1 contains a schematic summary of the main differences between the more widely used laser surfacing techniques.

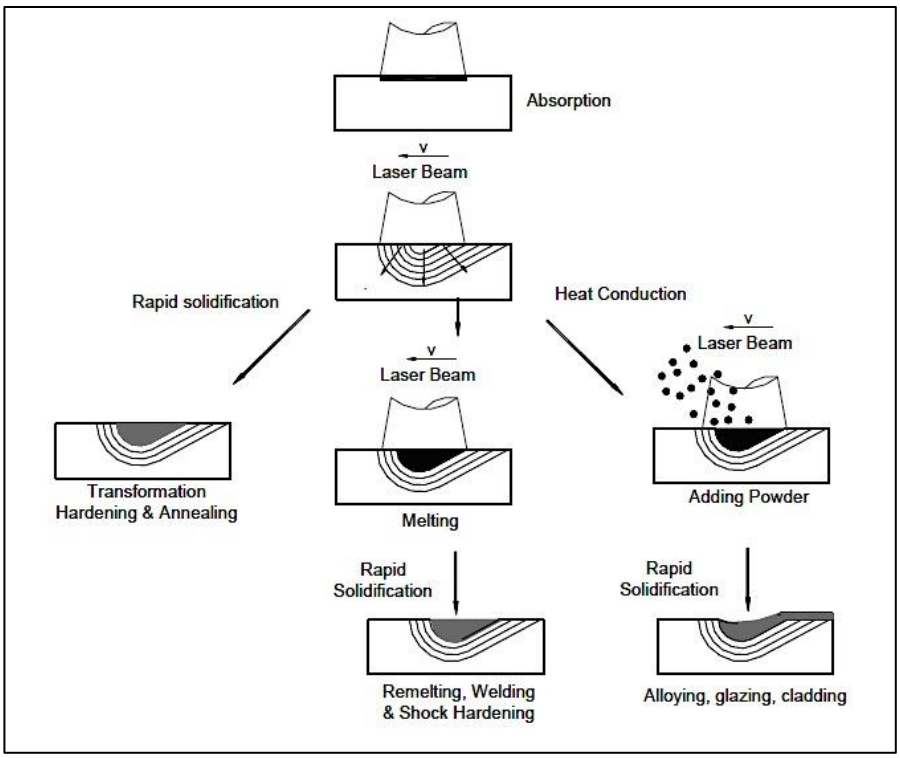

Figure 2.1.1. Schematic representation of the principles governing different laser surfacing techniques [3].

Laser cladding, as illustrated in Figure 2.1.2, utilises the heat of a laser beam to deposit a metallic layer onto the surface of a suitable substrate material. Consumables for the process are in the form of filler wires, fed directly into the melt pool, or metallurgical powders, either preplaced on the surface of the substrate or injected into the laser beam. In the powder injection method, powder delivery to the melt pool is achieved by

means of an inert carrier gas such as argon or helium. This method is more efficient, versatile and reproducible than any other delivery method. The powder absorbs part of the laser energy and is fused with a thin layer of the substrate surface to create a metallurgically bonded surface layer. A clad bead is formed either by means of a moving laser attached to a robotic arm, continuously scanning the surface of the substrate, or by having the laser stationary with the substrate in motion. Additional inert shielding gas may be added to the system, if required [3-7].

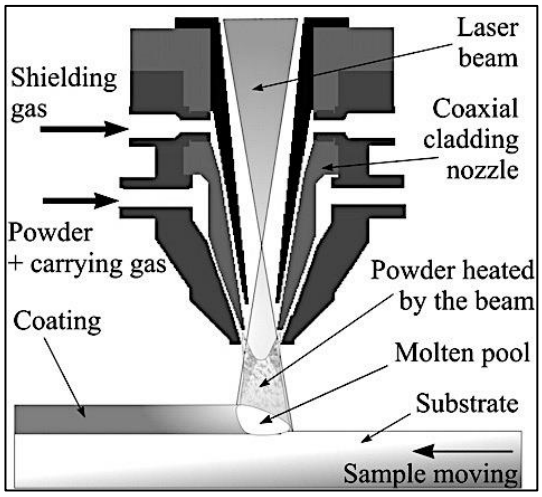

Figure 2.1.2. Process principles for laser cladding [8].

Laser cladding has several advantages over conventional overlay techniques using submerged arc welding (SAW) or gas tungsten arc welding (GTAW) procedures. The focused heat source during laser cladding ensures lower heat input levels, resulting in rapid cooling rates compared to arc cladding processes. Laser cladding exhibits lower levels of dilution between the consumable and the substrate, thermal distortion is minimised and lower levels of residual stress develop during treatment. Due to the low heat input levels and rapid cooling rates achieved with laser processing, finer metallurgical microstructures and narrower heat-affected zones form in the laser treated regions. More uniform compositions, and hence, more uniform hardness levels, are formed across the surfaces of laser treated materials. Laser cladding generally results in high wear resistance, improved corrosion resistance and good high-temperature oxidation properties. A hard surface layer can be formed while the core material retains its load-bearing capability [5,6,9,10].

Laser cladding finds application in life extension, maintenance, repair and refurbishment of components exposed to abrasive, erosive and adhesive wear, high temperature oxidation, corrosion and fatigue. Various industries make use of laser cladding, including the steel, aerospace, medical, automotive and mining industries. Typical examples of laser cladding applications include the hardfacing of tools, cladding of hydraulic pump components, refurbishment of gas turbines, moulds and continuous caster rolls, and the cladding of shafts, valve parts, sealing joints and exhaust valves in engines [3,9-12].

Although laser cladding holds promise for various surfacing applications, a number of challenges exist on a production level. These include the high running, operating and maintenance costs associated with laser processing technologies. There is a shortage of technical knowledge in the field of laser engineering and

processing, which often leads to unforeseen technical obstacles associated with the integration of new technologies into an application-driven industry [13].

The current investigation examined *in-situ* nitrogen alloying during the laser cladding of martensitic stainless steel onto a carbon steel substrate. A short description of the laser cladding process, the equipment used and the process parameters is given below, followed by a discussion of the laser cladding of martensitic stainless steels and the techniques available for introducing nitrogen during the cladding process.

2.1.2 The Nd:YAG laser

Two types of lasers are used in most laser cladding applications: the CO_2 laser and the solid-state Nd:YAG laser, with wavelengths of 10.6 μm and 1.06 μm, respectively. Both lasers are reliable, have high power outputs and high beam efficiencies. Beam delivery from the laser to the workpiece in the case of a CO_2 laser is through a laser beam duct containing a series of mirrors which directs the laser. In the case of a Nd:YAG laser, beam delivery is accomplished by means of flexible fibre optic cables [14]. A 4.4 kW continuous wave Nd:YAG laser is used at the NLC to conduct most cladding operations. It is the laser at the NLC with the widest power range (and hence, the widest range of application) and is, therefore, the laser used in this study.

The word “laser” is an acronym for “light amplification by stimulated emission of radiation”. To produce a laser beam, an active laser medium is excited and stimulated to emit photons with a specific wavelength. In the case of a Nd:YAG laser, the active medium is a rod-shaped neodymium (Nd)-doped yttrium-aluminium-garnet (YAG) crystal. Photons are excited by means of xenon or krypton flash lamps. Once the crystal is optically active, it emits light at a wavelength of 1.06 μm. The light signal passes through a two-mirror resonator, which enhances the signal. The beam is then focussed by means of conventional optics [15,16].

To achieve high power outputs, several Nd:YAG crystals may be used within the resonator. Beam divergence increases with increasing power output, which limits the minimum laser beam diameter and reduces the propagation distance. For this reason a Nd-YAG laser is transmitted by means of optical fibres and focused on the workpiece surface using optical lenses [16,17].

2.1.3 Powder feed nozzles

During laser cladding, the quality of the clad layer is highly dependent on the powder delivery system. The interaction of the laser beam, the injected powder and the inert carrier gas with the melt pool determines the final product quality. It is important to optimise variables such as the intersection of the laser beam with the injected powder stream, the focal point diameter and the position of the powder stream for different nozzle configurations [3].

Different powder feed nozzle designs are currently in use. The most widely used designs are the coaxial-feeding nozzle and the lateral-feeding nozzle, as illustrated in Figure 2.1.3. The lateral or off-axis nozzle has higher powder efficiencies than the coaxial nozzle, as defined by the ratio of powder melted by the laser to

the powder delivered by the powder feeder. On the other hand, it is more sensitive to the cladding direction than the coaxial nozzle [3].

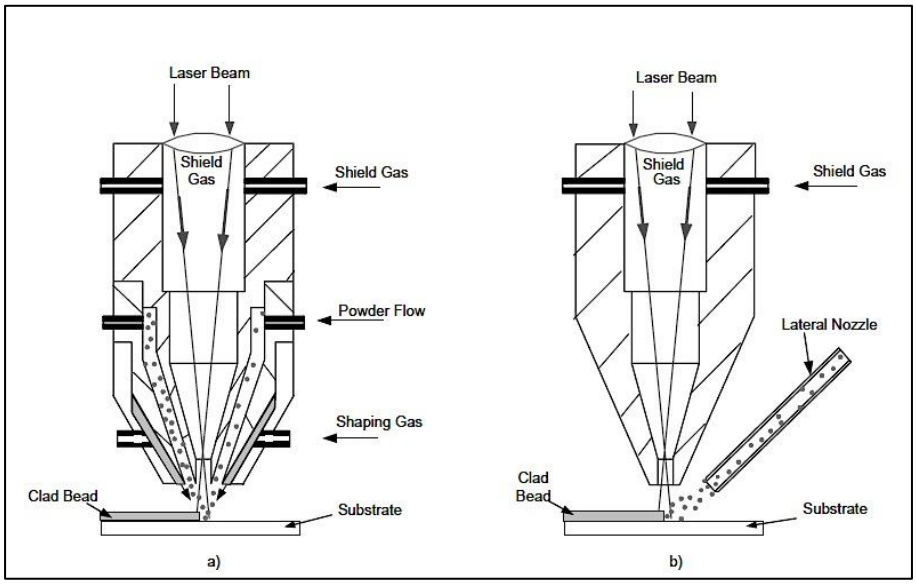

Figure 2.1.3. Powder feed nozzle configurations for: (a) coaxial powder feeding; and (b) lateral powder feeding [3].

In this study, coaxial nozzles were used to accommodate multi-directional laser cladding. The high volume of the metallurgical powders utilised prompted the use of two types of coaxial nozzles. Selection of either a continuous coaxial nozzle or a discontinuous coaxial nozzle, as illustrated in Figures 2.1.4(a) and (b), was based on powder-carrying capacity.

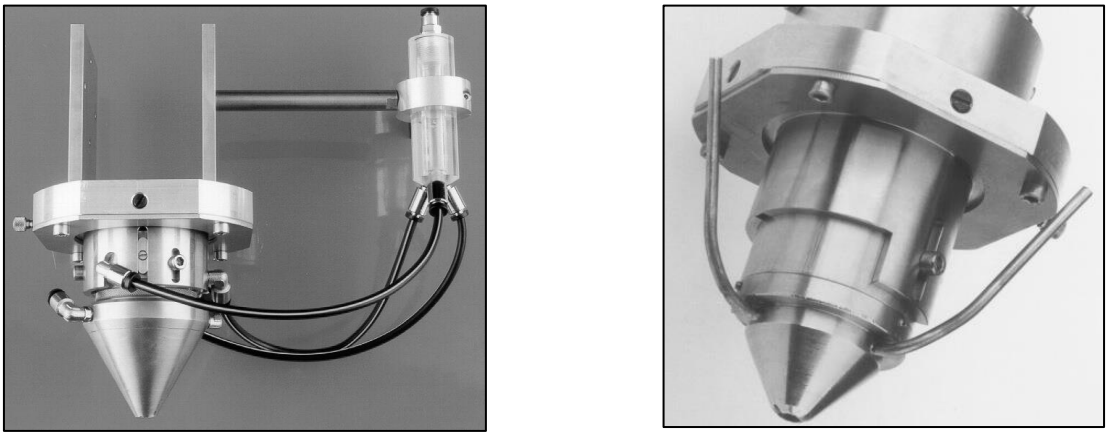

(a) (b)

Figure 2.1.4. Nozzle configurations for: (a) continuous coaxial nozzle; and (b) discontinuous coaxial nozzle (three-way nozzle) [18].

In the continuous coaxial or powder injection nozzle (Figure 2.1.4(a)), the laser beam is projected through the central cone of the nozzle. Inert carrier gas transports powder from the powder feeder into a splitter that divides the powder into three identical streams. From there, it moves into a circular chamber where it expands into a homogeneous cloud of powder. The powder stream then moves through an enclosed cone-shaped chamber and exits the nozzle in a conical shape. The profile of the conical powder flow is mainly

dependent on the apex angle of the inner cone. The focal point diameter, d_p, shown in Figure 2.1.5(a), is dependent on the exit-slit diameter, the nozzle tip-to-workpiece distance or focal point of the cone, f_p, the particle feed rate and the size distribution of the powder. A focal point distance, f_p, of 11 mm generally ensures optimal powder efficiency [18].

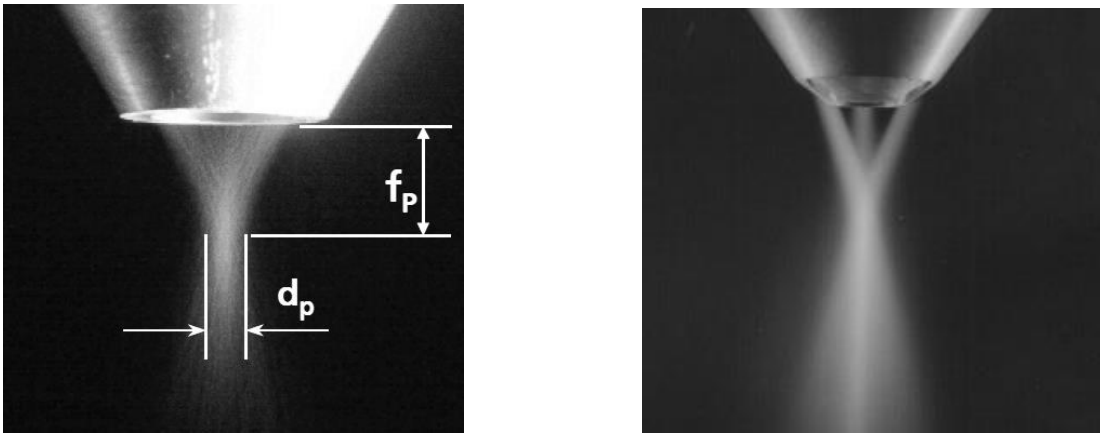

(a) (b)

Figure 2.1.5. Exit-cone shapes of powder streams for: (a) the continuous coaxial nozzle; and (b) the discontinuous coaxial nozzle (three-way nozzle) [18].

In the discontinuous coaxial or three-way nozzle, three powder streams exit the nozzle tip through identical holes around the laser beam in a cone-shaped profile, as shown in Figure 2.1.5(b). The cone's focal point diameter at the surface of the workpiece is dependent on the exit-hole diameters in the nozzle tip, the exit-angle of the powder streams, the nozzle tip-to-workpiece distance or focal point distance, f_p, the powder feed rate and the size distribution of the powder. A focal point distance, f_p, of 12 mm generally ensures optimal powder efficiency. The diameters of the hollow chambers and exit holes through which the powder is transported limit the powder-carrying capacity of the nozzle [18].

2.1.4 Optimisation of laser cladding parameters

The quality of any deposited layer depends on a number of process parameters and their complex interactions. Before cladding can commence, these parameters require detailed optimisation. Parameters that need to be considered include the relative laser beam-to-workpiece speed or cladding speed, the interaction time of the laser beam on the substrate surface, the laser power output, the powder feed rate, the powder stream profile and the laser beam diameter at the interaction level (or laser spot size). These parameters affect the quality of the clad bead in terms of clad geometry, dilution, microstructure, surface roughness, hardness, residual stress, crack-sensitivity and porosity [3,19].

Figure 2.1.6 shows a typical cross-sectional profile of a clad bead:

where: w is the bead width,
h is the clad height,
b is the depth of penetration, and
θ is the contact angle between the clad bead and substrate surface.

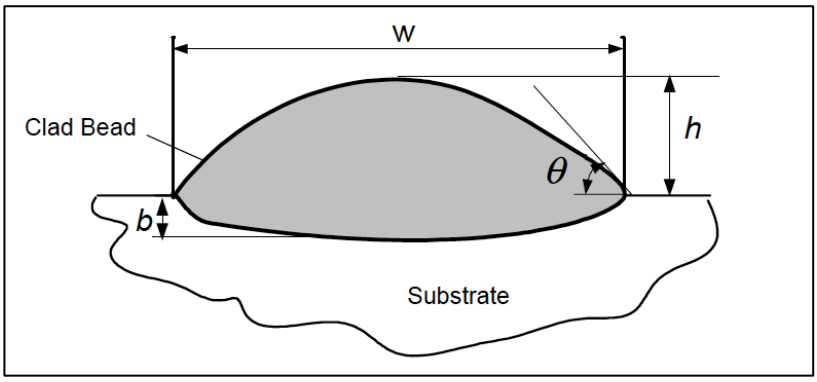

Figure 2.1.6. Typical cross-sectional clad bead profile [3].

According to Toyserkani [3], equation (2.1.1) defines the geometrical dilution of a clad bead, or the degree of mixing between the melted substrate material and the deposited layer.

$$\text{Dilution} = \frac{b}{h+b} \quad \ldots (2.1.1)$$

Kathuria [20] and Huang *et al.* [21] showed that an increase in laser scanning speed, which correlates to a decrease in interaction time, leads to refinement of the bead microstructure. A more refined microstructure increases the hardness of clad layers. Huang *et al.* [21] also observed that an increase in powder feed rate leads to a refinement in the bead microstructure due to a reduction in the specific energy per unit mass. A portion of the laser power is absorbed by the additional powder entering the laser beam, resulting in less heat being absorbed by the substrate and hence, a higher cooling rate.

Qian *et al.* [22] further noted that a complex situation arises when the cladding speed increases at a constant powder feed rate. They reported an increase in dilution as the cladding speed increases and attributed this to less powder deposited per unit area of the clad layer for a constant powder feed rate. This demonstrates a reduced dependency on interaction time, with dilution levels influenced by the absorbed power per volume of deposited powder, as shown in Figure 2.1.7 for three different powder feed rates.

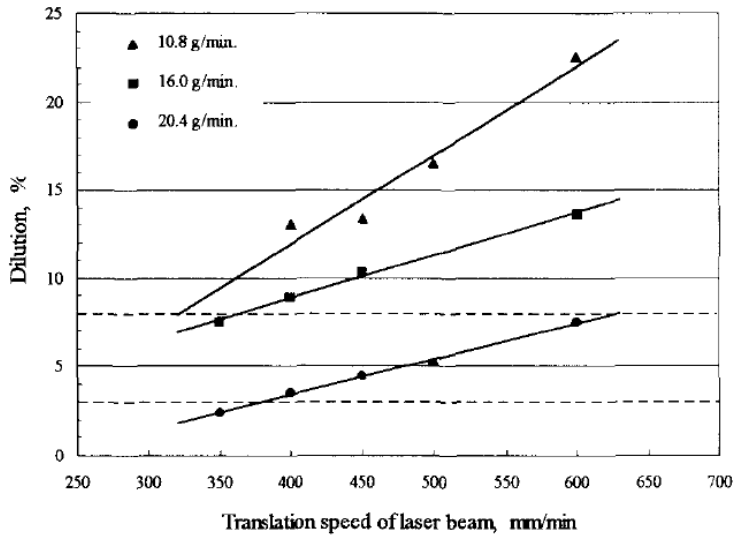

Figure 2.1.7. Dilution (%) as influenced by cladding speed (mm/min) and powder feed rate (g/min) [22].

Also evident from Figure 2.1.7 is a reduction in percentage dilution with an increase in powder feed rate, attributed to the increased powder volume consuming additional laser power. Pelletier and Sahour [23] observed the same trend, shown in Figure 2.1.8. According to Sexton and Byrne [24], the maximum amount of dilution tolerable in laser cladding is approximately 5%.

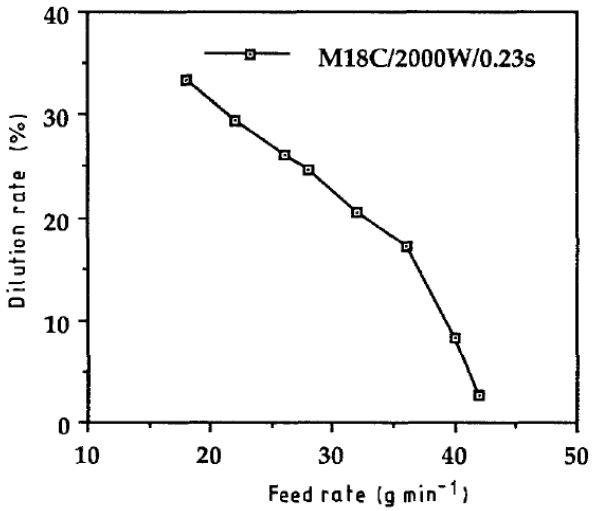

Figure 2.1.8. Dilution (%) as a function of powder feed rate (g/min) [23].

Several authors [23,25-26] observed that the bead dimensions, in particular the clad height, increase with an increase in the powder feed rate with a consequent decrease in dilution, as illustrated in Figure 2.1.9(a). Figure 2.1.9(b) shows the influence of the parameter *F*/*S*, or the ratio of powder feed rate to cladding speed, on the clad height.

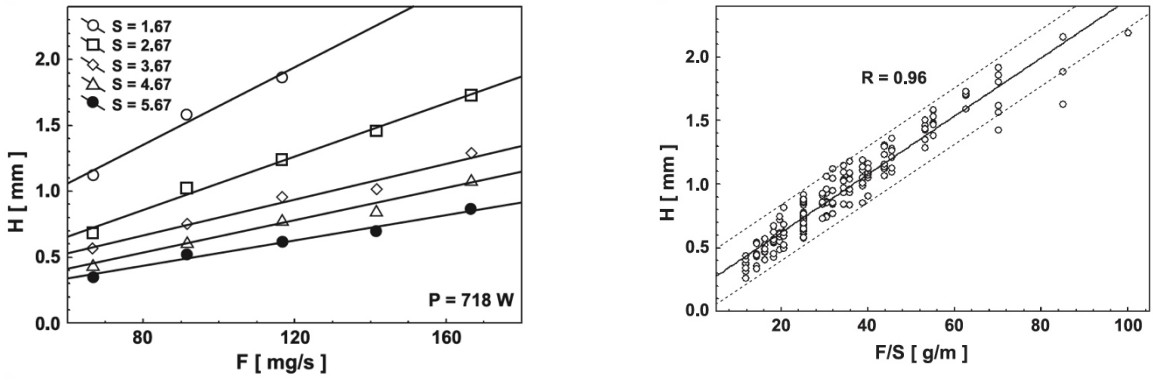

(a) (b)

Figure 2.1.9. Clad height *H* (mm) as a function of: (a) powder feed rate *F* and cladding speed *S*; and (b) the combined parameter *F*/*S* [25].

Chryssolouris *et al.* [27] reported the same dependence of clad height on powder feed rate and scanning speed. These authors also observed that the width of the clad bead is solely dependent on the laser spot size or laser beam diameter. This is contradictory to the findings of De Oliveira *et al.* [25], who reported the relationships shown in Figure 2.1.10 for clad width, laser power and scanning speed.

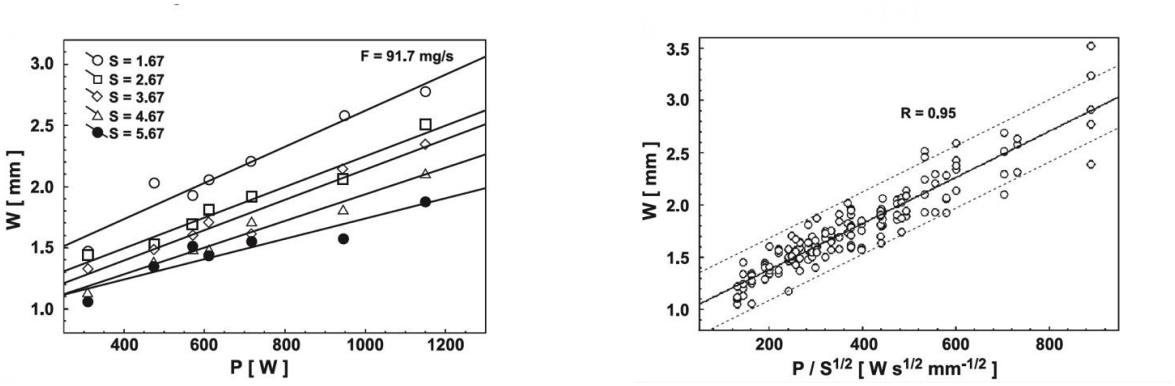

(a) (b)

Figure 2.1.10. Clad width *W*, as influenced by: (a) laser power *P* and cladding speed *S*; and (b) the combined parameter $P/\sqrt{S}$ [25].

Li *et al.* [28] concluded that the clad width is dependent on the laser spot diameter, the cladding speed and the powder feed rate. They also found that nearly all processing parameters have an influence on the bead dimensions, including such variables as the powder injection point, making it difficult to quantify the effect of laser processing parameters on bead height and dimensions.

According to Sexton and Byrne [24], the aspect ratio, or bead width/height ratio, is important especially in the case of interbead porosity when gas bubbles are trapped between overlapping beads. This occurs when the aspect ratio of a single-track bead is less than five, i.e. $W/H \leq 5$.

Steen and Courtney [29] showed that, due to the complex nature of laser-parameter interactions, combining parameters for optimisation was more effective. They demonstrated that for a certain cladding speed, *S*, there is a minimum value of the combined parameter P/d_p, the ratio of laser power to laser beam diameter, where a transition from discontinuous to continuous clad beads occurs. They also showed that the amount of dilution and the aspect ratio *W*/*H* increase linearly with an increase in the combined parameter *P*/*S*, which is the ratio of laser power to cladding speed.

Wu *et al.* [30] defined two terms related to the quality of a clad bead: the specific energy *E* and the powder density *G*, given by equations (2.1.2) and (2.1.3), respectively. The specific energy defines the laser energy contained within the laser beam diameter in terms of the cladding speed or interaction time. The powder density is the amount of powder delivered to the area where the laser power is consumed by the powder and the substrate.

$$E = \frac{P}{V d_p} \quad (\text{J/mm}^2) \qquad \ldots (2.1.2)$$

$$G = \frac{F}{V d_p} \quad (\text{g/mm}^2) \qquad \ldots (2.1.3)$$

where: P is the laser power (W),
V is the cladding speed (mm/s),
F is the powder flow rate, and
d_p is the laser spot size or beam diameter.

Figure 2.1.11 shows two conditions, defined by Wu *et al.* [30] in relation to *E* and *G*: a critical condition and a fine condition. The critical condition describes a point in the combination of laser parameters where a transition takes place from a discontinuous to a continuous bead. The fine condition marks the transition from a continuous bead to a good quality bead.

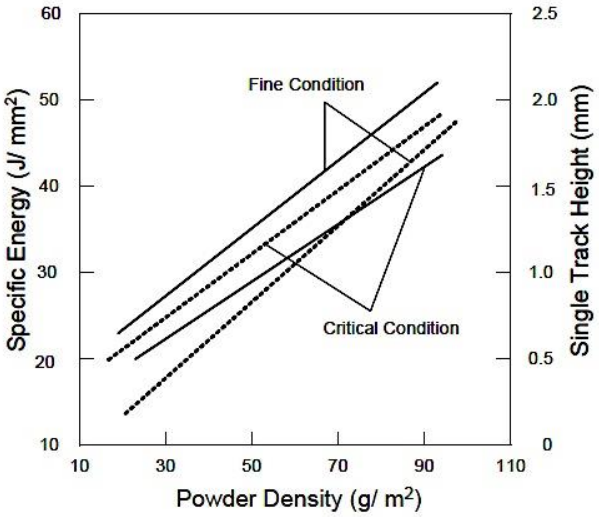

Figure 2.1.11. Specific energy (*E*) required as a function of powder density (*G*) to achieve critical and fine conditions (____), and the clad height dependence on powder density (-----) [30].

This discussion suggests that the laser cladding process is sensitive to various parameters and parameter interactions and highlights the need for parameter optimisation. More information on the parameter optimisation performed during this investigation is given in Chapter 4.

2.2. LASER CLADDING OF MARTENSITIC STAINLESS STEELS

2.2.1 Introduction

In a growing number of industries, increasing demands on resource efficiencies place high requirements on the performance of components. The quality of the materials used is a critical factor in optimising industrial processes. Emphasis is therefore placed on material selection with regards to improved mechanical and physical properties, novel manufacturing techniques and improved design of components to achieve high-quality products. The cost and availability of materials are also of major concern with regards to material selection. In applications where light weight and increased strength are important, martensitic stainless steels are often preferred on account of their high strength, high as-quenched hardness and good toughness in the tempered condition [31,32].

Martensitic stainless steels typically contain between 11.5% and 18% chromium, and are deliberately alloyed with up to 0.6% carbon. The development of this family of stainless steels was prompted by the need for corrosion resistant stainless steels that are hardenable by heat treatment. Martensitic stainless steels are austenitic at elevated temperatures and are usually hardened by heating above the transformation range to temperatures in the region of 1000°C, followed by cooling in air or oil to transform the austenite to

martensite. Time at temperature must be minimised to prevent decarburisation or excessive grain growth. In order to obtain mechanical properties suitable for engineering applications, the steels are tempered after quenching. This results in an excellent combination of moderate to good corrosion resistance, high hardness and strength, good resistance to thermal and mechanical fatigue and excellent wear resistance. Martensitic stainless steels are magnetic, can be cold-worked and hot-worked (especially at lower carbon contents), can be machined satisfactorily, display high toughness and possess good corrosion resistance to weather and some chemicals. They attain their best corrosion resistance in the hardened condition [33].

For a martensitic stainless steel to possess adequate hardness, wear resistance and corrosion resistance, no δ-ferrite should be present at the austenitising temperature (950°C to 1010°C), the martensite transformation range should be above room temperature (to reduce the risk of retained austenite) and the steel should exhibit maximum temper resistance. As the martensitic transformation is the dominant strengthening mechanism in these steels, processing must be designed to ensure that no, or at best, minimal retained austenite is present after cooling [34].

12% Chromium martensitic stainless steels, such as modified AISI 410 and AISI 420, are often used in the repair and refurbishment of gas turbine blades in steam power plants and continuous caster rolls in the steel industry. Gas tungsten arc welding (GTAW) and submerged arc welding (SAW) cladding processes are widely used. As these components experience failure through several mechanisms inherent in and caused by the operating and service conditions, the purpose of repair and refurbishment is to increase the operational life as much as possible [35-37].

In the case of turbine blades, failure may occur during high-pressure cycles due to condensed water droplet erosion, also known as cavitation erosion. Liquid droplets impinge on the surface of the blade's leading edge where rotational speeds are at a maximum. During low-pressure cycles, erosion can be caused by foreign solid particles at the blade's lower trailing edge, resulting in surface roughness and erosion grooves. Furthermore, steam purity is of cardinal importance as impurities such as chloride ions affect the corrosion behaviour of the blades. These impurities do not affect the general corrosion behaviour of the material to any significant extent, but localised corrosion such as pitting corrosion can occur on the surfaces. These wear and corrosion mechanisms promote the formation of surface discontinuities that act as stress raisers, ultimately leading to fatigue failure of the turbine blades. Creep rupture can also occur due to the high operating temperatures and pressures of steam turbines [34,38-40]. High-nitrogen martensitic stainless steels are finding increasing application in the steam-turbine industry where erosion, erosion-corrosion, cavitation erosion, fatigue and sliding wear are caused by the harsh operating conditions [41,42].

Due to the extreme operating environment, continuous caster rolls in steel mills can experience failure due to a number of mechanisms. Operating conditions include high fluctuating surface temperatures, often exceeding 600°C, high fluctuating contact pressures and low pH environments. This leads to failure due to adhesive and abrasive wear, general and localised corrosion, thermal and mechanical fatigue and stress corrosion cracking. In this application martensitic stainless steel is beneficial as a surfacing material on

account of its high hardness, strength and low coefficient of thermal expansion. It has been shown that the use of high-nitrogen martensitic stainless steel enhances the resistance of rolls to pitting and intergranular corrosion, and leads to increased strength, hardness, wear resistance and high-temperature oxidation resistance [43,44].

Several authors [10,38,39,45-47] have reported that laser cladding produces coatings with superior physical and mechanical properties compared to conventional coating and overlay procedures, such as arc welding and plasma cladding. In addition, the risk of porosity and crack formation is reduced in aerospace materials, turbine blades and continuous caster rolls coated by laser cladding. As Rombouts *et al.* [48] put forward, laser cladding with martensitic stainless steel can be applied successfully in the repair of turbine and other high-quality components such as heat and deformation sensitive materials.

As stated by Kathuria [38], laser cladding enhances several mechanical properties and optimises certain physical and microstructural features of deposited layers compared to conventional overlay techniques. Laser cladding uses a lower heat input and brings about higher hardness and lower levels of dilution with a sharp transition in hardness between the surface coating and base material. An even and uniform deposition of the consumable is achieved and reduced distortion results from the focused and low heat input provided by the laser beam. These inherent benefits to laser cladding were successfully demonstrated in the repair of turbine blades.

2.2.2 Effect of rapid solidification on microstructure

The rapid cooling rates associated with laser cladding may alter the phase constitution of the final microstructure obtained at room temperature from that obtained during conventional arc cladding. The cooling rate can change the primary solidification mode of martensitic stainless steels predicted from thermodynamic considerations; from primary ferritic to primary austenitic. In addition, it can alter the temperature at which the diffusionless transformation from austenite to martensite occurs, the martensite-start (M_s) temperature, and affect the high-temperature austenite grain size, which, in turn, also affects the M_s temperature [49].

Several authors [49-51] have reported that as the cooling rate during laser welding and laser cladding increases, the M_s temperature steadily decreases. Figure 2.2.1 shows the influence of cooling rate on the M_s temperature of AISI 410 martensitic stainless steel after austenitising at four different temperatures. Lower M_s temperatures are obtained after austenitising at higher temperatures. The austenitising temperature affects the M_s temperature by altering the high temperature austenite grain size and the amount of alloying elements dissolved in the matrix [50].

The reduction in the M_s temperature with a decrease in the prior austenite grain size has been studied in detail [51,52]. Figure 2.2.2(a) shows the influence of grain size on the M_s temperature as determined from dilatometric data for a martensitic steel, whereas Figure 2.2.2(b) shows the same dependence determined from a mathematical model based on the grain size variation, *D*, of AISI 431 martensitic stainless steel. It is

evident from Figures 2.2.2(a) and (b) that the influence of grain size on the M_s temperature is more significant at the lower end of the grain size spectrum, i.e. at extremely small prior austenite grain sizes.

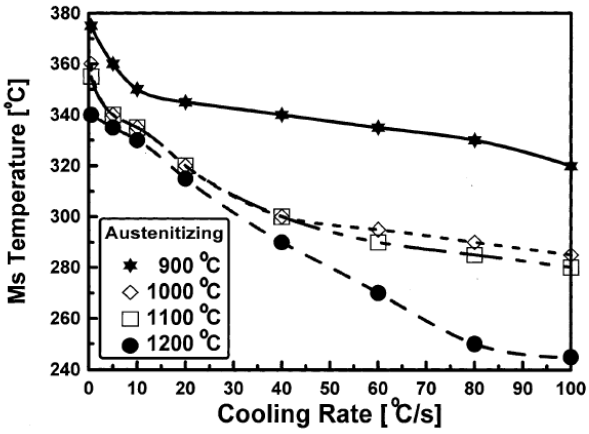

Figure 2.2.1. The influence of cooling rate on the M_s temperature of laser processed AISI 410 martensitic stainless steel for different austenitising temperatures [50].

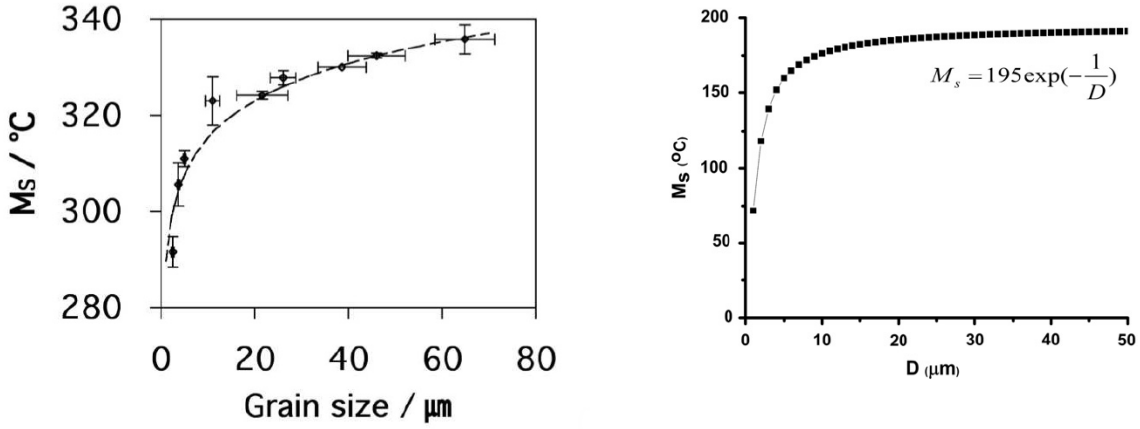

(a) (b)

Figure 2.2.2. The influence of prior austenite grain size (µm) on the M_s temperature (°C): (a) as determined by dilatometric data [52]; and (b) calculated using a mathematical model [51] for different ferrous alloys.

The austenite dendrite arm spacing has the same effect as the prior austenite grain size, i.e. smaller dendrite arm spacings reduce the M_s temperature. Hemmati *et al.* [51] illustrated the influence of cooling rate on the austenite dendrite arm spacing by increasing the cladding speed while holding all other laser parameters constant. This resulted in an increased cooling rate as the effective heat input was decreased, inhibiting dendritic growth as less time was spent at high temperatures. This effect is illustrated in Figure 2.2.3.

The influence of grain size on the M_s temperature can be explained by considering that the martensite transformation is accompanied by 3 different deformation reactions known as the Bain distortion, a shear deformation parallel to the transformation interface, and a lattice rotation of the transformed martensite [53]. Since this involves plastic deformation of the austenite lattice, it is reasonable to assume that the yield strength of the austenite should be taken into account when considering the strain energy necessary for this transformation to proceed. The yield strength increases with decreasing grain size as shown by the Hall-

Petch relationship [50-53], therefore, the martensite transformation occurs at increasing strain energies only available at lower temperatures.

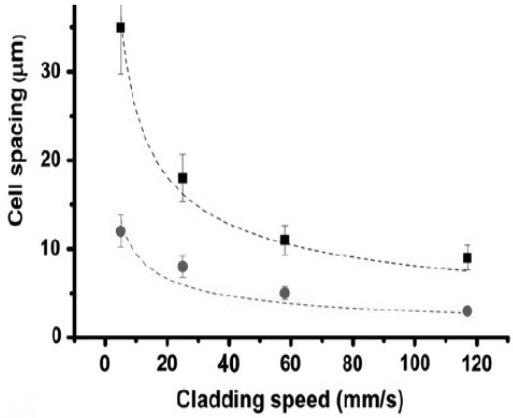

Figure 2.2.3. Cell spacing of austenite dendrites as a function of the speed of cladding [51].

Several authors [54-56] have reported that a sharp increase in cladding speed or a drastic decrease in laser power resulted in lower hardness values due to higher percentages of retained austenite in the final clad layers. This effect is extensive and cannot completely be ascribed to a decrease in the M_s temperature with a reduction in austenite grain size. David *et al.* [57] reported that an increase in cooling rate during laser welding gradually changes the solidification mode from primary ferritic to primary austenitic. The dependence of solidification mode on chemical composition shifts to a dependence on nucleation kinetics. Austenite nucleation occurs more rapidly than ferrite nucleation and at large supercoolings the kinetic-dependent solidification mode therefore favours austenite nucleation. This was confirmed by Van Rooyen *et al.* [58] and Hemmati *et al.* [55] who reported that the amount of observed delta ferrite (δ) decreased and even disappeared completely at increased cooling rates, even when the predicted solidification mode was primary ferritic.

The influence of primary solidification mode and M_s temperature on microstructure is depicted in the modified Schaeffler diagram for laser welding applications developed by David *et al.* [57] and shown in Figure 2.2.4. This diagram takes into account the higher cooling rates associated with laser processing and shows a shift in the phase boundaries and a narrowing of the dual-phase austenite+ferrite (A + F) phase field. This modified Schaeffler diagram was used in the design of experimental alloys for laser cladding applications in this study, as described in more detail in Chapter 4.

2.2.3 Effect of alloying elements on microstructure

Although the cooling rate, the austenitising time and temperature, the stress state and prior deformation may have discernible effects on the M_s temperature [54], the main factor determining the microstructure of stainless steel is the chemical composition [60]. All alloying elements have the effect of reducing the M_s temperature, with the exception of cobalt and aluminium. Those elements that form interstitial solid solutions have the greatest effect on the M_s temperature [49].

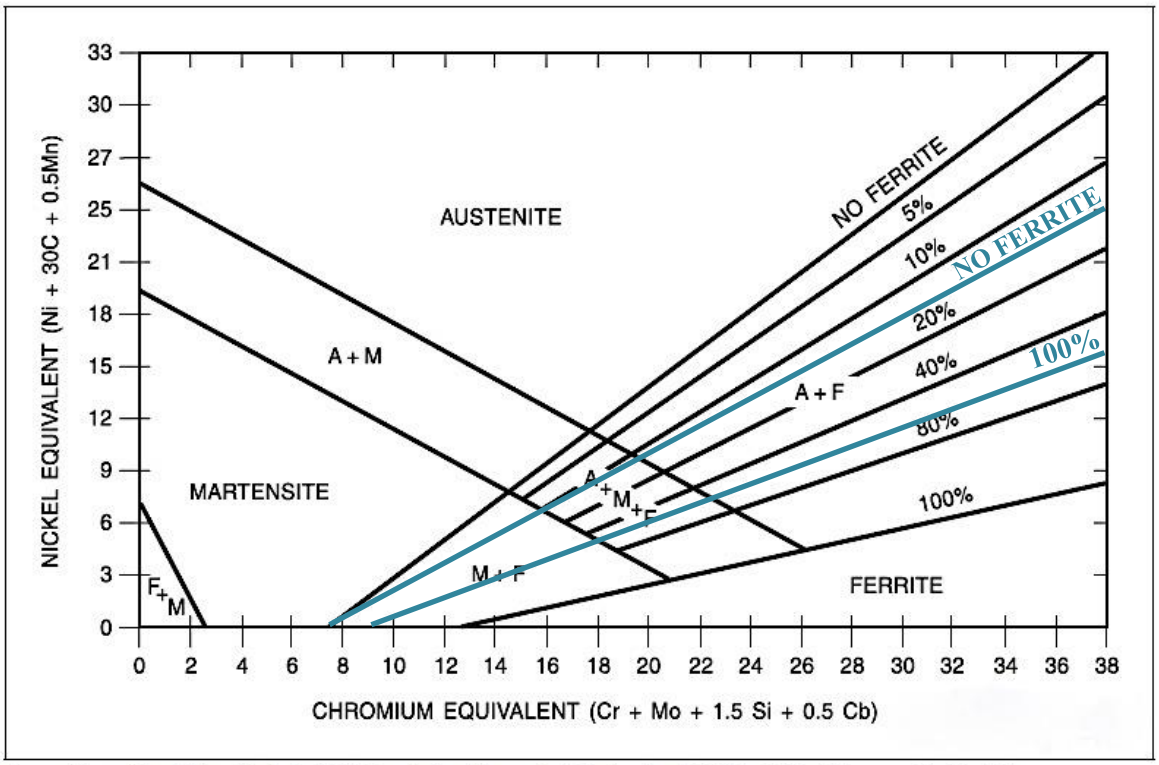

Source: Adapted from Schaeffler, A. L., 1949, Constitution Diagram for Stainless Steel Weld Metal, *Metal Progress* 56: 560–560B.

Figure 2.2.4. Modified Schaeffler diagram for laser welding processes. Adapted from the AWS Welding Handbook [59] according to David *et al.* [57].

The M_s temperature of steels and stainless steels is an important factor in the design of new alloys, processing techniques and in determining the weldability of alloys. Several authors [60-67] have produced mathematical equations for predicting the M_s temperature based on the chemical composition of iron-based alloys, using either empirical methods or calculations based on thermodynamic data. These equations have found widespread application, although they all suffer from the drawback of being applicable only within the compositional limits set by the range of experimental alloys used in their derivation.

Equation (2.2.1) shows the equation for determining the M_s temperature that was used in the design of the experimental alloys in this study, as described in Chapter 4. Capdevila *et al.* [67] developed this equation using a neural network analysis based on non-linear regression modelling and experimental data. Table 2.2.1 shows the compositional limits that ensure the accuracy of equation (2.2.1).

$$M_s\,(K) = 767.7 - 305[C] - 30.6[Mn] - 14.5[Si] - 8.9[(Cr] - 16.6[(Ni] + 2.4[Mo] + 5.3[V] + 8.58[Co] + 40.4[Al] + 7.4\,[W] - 11.3[Cu] + 510.4[Nb] \quad \ldots (2.2.1)$$

where: M_s is the martensite start temperature in Kelvin (K), and
[M] is the amount of each alloying element in wt%.

Table 2.2.1. Maximum compositional limits for accurate use of equation (2.2.1) (wt%) [67].

C	Mn	Si	Cr	Ni	Mo	V
1.62	3.76	3.4	17.9	27.2	5.1	4.55
Co	Al	W	Cu	Nb	B	N
30.0	1.1	12.9	0.98	0.23	0.01	0.06

2.2.4 Alloy design of martensitic stainless steel for laser cladding applications

This study focused on the development of low cost martensitic stainless steels with moderate corrosion resistance, high hardness and good wear resistance for laser cladding applications. Potential applications include the surfacing and repair of steam turbine blades and continuous caster rolls. To achieve this objective, the investigation examined the addition of nitrogen to type AISI 410L martensitic stainless steel. Table 2.2.2 gives the specified chemical composition of commercially available type AISI 410L.

Table 2.2.2. The specified (nominal) chemical composition of type AISI 410L (weight percentage, wt%) [68].

Fe	C	Cr	Mn	Si	Ni	P	S
Balance	0.03 max	12.0-13.0	1.00 max	1.00 max	0.5 max	0.04 max	0.03 max

AISI 410L, with a maximum carbon content of 0.03%, is the low-carbon version of martensitic stainless steel AISI 410, with a maximum carbon content of 0.15%. The lower carbon content of AISI 410L results in a ferritic microstructure at room temperature [68]. Due to its low price and moderate corrosion resistance, AISI 410L is widely used in the powder metallurgical industry where a number of applications require the use of ferritic stainless steel [69].

The chemical composition of type AISI 410L consists of a narrow range of alloying elements that do not induce complex phase transformations on cooling. The main alloying elements in ferritic and martensitic grades of stainless steel are carbon and chromium. Chromium is added to ensure corrosion resistance through the formation of a thin hydrated oxide layer on the surface (of stoichiometric form Cr_2O_3) which acts as a diffusion barrier to oxygen in the atmosphere. Chromium is a strong ferrite-promoting element [70]. Carbon is added as a solid solution strengthening agent and in the case of martensitic stainless steels, also to ensure the diffusionless transformation from austenite to martensite on cooling. Carbon is a strong austenite-forming element and enlarges the austenite phase field at high temperatures at the expense of ferrite. High temperature austenite transforms to martensite below the M_s temperature. In stainless steels, the carbide-forming tendency of carbon can be problematic, especially during welding when chromium-rich carbides of the form $M_{23}C_6$ or $(Fe,Cr)_{23}C_6$ precipitate with relative ease. Precipitation of $M_{23}C_6$ carbides results in chromium depletion of the surrounding matrix, referred to as sensitisation, which leads to a loss of passivation. The consequent loss in corrosion resistance prompted the development of low-carbon (L) stainless steel grades [70].

In the absence of high levels of carbon, additional alloying is required to ensure full transformation to martensite during cooling after laser cladding of AISI 410L. The nickel equivalents of the Schaeffler diagram shown in Figure 2.2.4 and the Balmforth diagram in Figure 2.2.5, used to predict room temperature microstructures in welds, can be used to indicate possible alloying routes to ensure a fully martensitic microstructure in the clad layers. These nickel equivalents are given in equations (2.2.2) [59] and (2.2.3) [71]. The amounts of alloying elements are in weight percentage.

$$\text{Ni-equivalent (Schaeffler)} = [\text{Ni}] + 30[\text{C}] + 0.5[\text{Mn}] \quad \ldots (2.2.2)$$

$$\text{Ni-equivalent (Balmforth)} = [\text{Ni}] + 35[\text{C}] + 20[\text{N}] \quad \ldots (2.2.3)$$

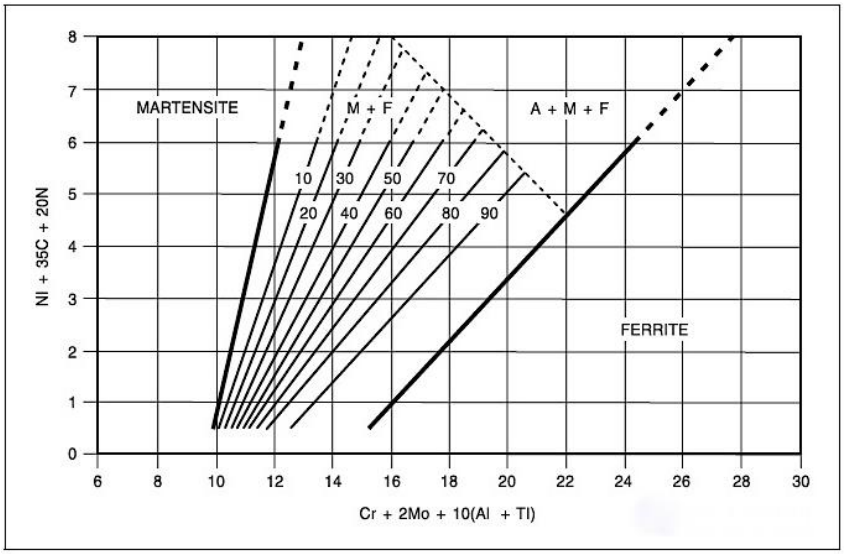

Figure 2.2.5. Balmforth diagram [71].

From the Schaeffler and Balmforth diagrams and their respective nickel equivalents, it can be seen that carbon, nickel, nitrogen, and to a lesser extent, manganese, can be used to promote the formation of austenite at elevated temperatures, restrict the formation of excessive δ-ferrite levels and consequently ensure a fully martensitic microstructure at room temperature, granted that these elements are in solid solution and the M_s temperature is not too low.

In addition to carbon, nickel and nitrogen are strong austenite-formers [70]. The role of manganese is more controversial and contradiction exists in published data concerning its role as an austenite-former. Many authors have reported that the addition of manganese has no effect on austenite formation, but merely acts as an austenite-stabiliser by lowering the M_s temperature, thus stabilising austenite at low temperatures [72], while others claim that manganese is a weak austenite-former [73]. Hull [74], on the other hand, found that manganese acts as a ferrite-former at concentrations of 2.5% and above, while Kemp *et al.* [75] found that at low interstitial carbon and nitrogen levels, manganese is indeed an austenite-former, regardless of its concentration. The reported influence of manganese on the formation of austenite at elevated temperatures can be attributed to its influence on the solubility of nitrogen in stainless steels. Manganese increases the solubility of nitrogen, a strong austenite-former, and higher austenite levels with an increase in manganese content may simply be the result of higher dissolved nitrogen levels in the alloy.

Manganese is therefore not favoured as an austenite-former in most stainless steels. Its attraction, however, lies in its negative interaction parameter with nitrogen. As described earlier, it increases nitrogen solubility in ferrous alloys [72,73,76]. Figure 2.2.6 shows data compiled by Pistorius and Du Toit [73] concerning nitrogen solubility in 17% chromium ferritic stainless steel at 1600°C with no other alloying elements in significant quantities, except for manganese and nitrogen, gathered from literature and compared with FactSage™ thermodynamic calculations.

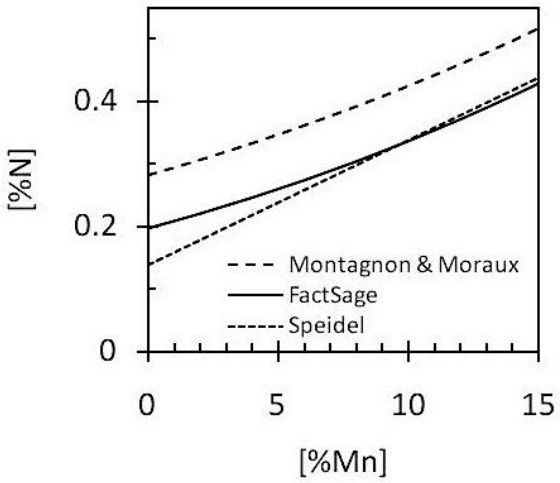

Figure 2.2.6. Nitrogen solubility data as a function of Mn content, gathered from literature and compared with FactSage™-based calculations at 1600°C [73].

This effect is discussed in more detail in section 2.3.4. On the other hand, manganese has a deleterious effect on the general and localised corrosion resistance of steels and stainless steels [73,77] as evidenced by the MARC rule shown in equation (2.2.4). The acronym "MARC" refers to the "measure of alloying for resistance to corrosion" and the equation represents an alloy's resistance to localised corrosion based on its alloying element content. The amounts of alloying elements are in weight percentage.

$$MARC = Cr + 3.3Mo + 20N + 20C - 0.5Mn - 0.25Ni \quad \ldots (2.2.4)$$

From the MARC rule, it can be deduced that co-alloying with manganese and nitrogen might offset the negative effect of alloying with manganese alone. Therefore, increasing nitrogen solubility with manganese additions may have a beneficial effect on pitting corrosion resistance on account of nitrogen's stronger effect on the MARC rule than that of manganese.

Lenel and Knott [78] conducted experiments on Fe-Cr-Mn-N steels consisting of 10 to 12% chromium, 5 to 10% manganese, 0.05% carbon and nitrogen ranging from 0.16 to 0.32%. After solution annealing and air cooling, they found that alloys containing 10% manganese consisted of unstable austenite at room temperature with M_s temperatures below -196°C. Those alloys that contained 8% manganese showed a mixture of residual austenite and martensite with an M_s temperature close to room temperature, and alloys with 5% manganese were martensitic with an M_s temperature of about 150°C. They also found that co-alloying with manganese and nitrogen had a beneficial effect on pitting corrosion resistance.

Due to the negative effect of manganese on the MARC rule and its effect on the M_s temperature in equation (2.2.1), manganese additions to the experimental alloys designed as part of this study were kept to a minimum, but high enough to take advantage of its effect on nitrogen solubility. Also taken into account in the selection of manganese levels was the effect of cooling rate on the modified Schaeffler diagram for laser welding. A maximum manganese level of 3.5% was selected.

Nickel has a negative effect on the localised corrosion resistance of stainless steels according to the MARC rule [79], but has a beneficial effect on corrosion resistance in reducing acids [73]. In contrast to manganese, nickel has a positive interaction parameter with nitrogen, reducing nitrogen solubility in steels and stainless steels [72]. Nickel may, however, indirectly enhance nitrogen solubility by serving as a strong austenite-former. It is well established that austenite has a higher nitrogen solubility than ferrite due to differences in crystal structure and lattice parameters. In fact, a significant difference between the typical nitrogen contents of high-nitrogen austenitic and ferritic stainless steels exists. An austenitic stainless steel is regarded as a "high-nitrogen stainless steel" when its nitrogen content exceeds 0.4 wt%, whereas the upper limit for ferritic and martensitic stainless steels is about 0.08 wt% [42,72,80]. For this reason, the nitrogen solubilities of different alloy systems were investigated by means of incremental nickel and manganese additions to AISI 410L stainless steel during the current investigation. This is described in more detail in Chapter 4.

From the Balmforth diagram of Figure 2.2.5, it is apparent that a fully martensitic microstructure can be attained in welds in 12% chromium steels at nickel levels exceeding about 5%. This agrees with the results of Van Rooyen [81] who reported a fully martensitic microstructure after laser cladding in modified AISI 410L with 5% nickel and additions of cobalt and molybdenum. Based on this finding, and to accommodate additional nitrogen in the experimental alloys, a maximum nickel concentration of 5.5% was selected in this investigation to prevent the retention of excessive amounts of residual austenite.

Nitrogen, apart from its role as an austenite-former, also enhances the physical and mechanical properties of steels and stainless steels. Lenel and Knott [78] showed that replacing carbon in martensitic stainless steels with nitrogen could lead to an increase in hardness. Alloys containing nitrogen as principle interstitial alloying element exhibit higher toughness than alloys containing an equal amount of carbon [72,82]. An increase in the interstitial nitrogen content of stainless steel increases the tensile strength, elastic modulus, hardness and wear resistance [83,84]. Nitrogen also improves the pitting and crevice corrosion resistance of martensitic stainless steels [73,80,85,86], as evident from the MARC rule in equation (2.2.4).

Most of the research in the area of high-nitrogen stainless steels was performed to investigate partial or complete nickel replacement. Due to the high cost and price volatility of nickel, and the human and animal propensities for nickel allergies, possible replacements for nickel in stainless steels have been proposed and investigated with respect to their influence on austenite formation, austenite stabilisation and corrosion resistance. It was shown that a combination of manganese and nitrogen is the most attractive replacement for nickel [72,73,80]. A considerable amount of research has been dedicated to the successful replacement of nickel in high-nitrogen, low-nickel or even nickel-free stainless steels. The bulk of this work was carried out

in the austenitic family of stainless steels [87-94] and to a lesser extent, the duplex grades of stainless steel [95-98].

Less research has been performed in the field of high-nitrogen ferritic and martensitic stainless steels due to their low solubility for nitrogen. As early as 1961, Babakov [76] produced a dual phase structure of martensite and residual austenite after alloying martensitic stainless steel with nitrogen. More recently, Ma *et al.* [99] demonstrated that nitrogen is a suitable replacement for nickel in martensitic stainless steel, successfully increasing the hardness of the martensite without a significant decrease in toughness, and fully suppressing δ-ferrite formation. They also found that tempering above 550°C impaired the corrosion resistance and drastically reduced toughness due to the precipitation of coarse hexagonal Cr_2N nitrides. This agrees with the work of Ojima *et al.* [100] who reported a loss in corrosion resistance after tempering high-nitrogen martensitic stainless steel above 500°C. Toro *et al.* [101] reported a reduction in erosion-corrosion resistance in high-nitrogen martensitic stainless steel at increasing temper temperatures in the range of 200°C to 600°C. This is due to CrN precipitation between 400°C and 600°C and Cr_2N nitride precipitation between 550°C and 600°C.

According to Du Toit and Van Niekerk [44], partial replacement of carbon with nitrogen in high-nitrogen martensitic stainless steels negates the need for tempering during the cladding of continuous caster rolls due to the higher toughness of the nitrogen-alloyed low carbon martensitic stainless steel. Due to lower carbon content, inter-bead corrosion due to sensitisation is also suppressed. For these reasons and in the absence of any impact stresses in the intended applications, tempering was not carried out during this investigation.

2.3 ALLOYING WITH NITROGEN

2.3.1 Introduction

The low solubility of nitrogen in iron at atmospheric pressure is an important concern when nitrogen alloying is considered. There is also a large difference between the austenite and ferrite solubility levels for nitrogen in pure iron, as shown in Table 2.3.1 [102]. Producing a high-nitrogen stainless steel therefore requires tight control over the amount of nitrogen dissolved in the steel during processing.

Table 2.3.1. Solubility of nitrogen in γ- and α-iron at various temperatures [102].

	Temperature (°C)	Solubility (wt %)
N in γ-iron	650	2.80
	590	2.35
N in α-iron	590	0.10
	20	<0.0001

During steelmaking, the solubility of nitrogen in stainless steel is dependent on three important variables: temperature, pressure and the composition of the alloy [88]. The nitrogen source and alloying method need further consideration as these factors determine the amount of available nitrogen and the homogeneity of the

final product. Essentially, a nitrogen source with a higher nitrogen potential than that of the alloy is required. In the presence of a gaseous nitrogen atmosphere, the nitrogen potential of the gaseous phase must be at least equal to that of the source to prevent nitrogen desorption, as shown in equation (2.3.1) [103].

$$\mu_N^{Gas} \geq \mu_N^{Source} \geq \mu_N^{Alloy} \quad \ldots (2.3.1)$$

where: μ_N^{Gas} is the nitrogen potential of the gaseous atmosphere,
μ_N^{Source} is the nitrogen potential of the nitrogen source, and
μ_N^{Alloy} is the nitrogen potential of the alloy.

When an iron alloy in the liquid state is enriched with nitrogen from a suitable source, segregation of nitrogen takes place during solidification. Nitrogen has a higher solubility in the liquid phase than in the solid and is therefore rejected to the liquid on solidification, as expressed by the equilibrium partition coefficient, *K*, in equation (2.3.2) [104].

$$K = \frac{S_S}{S_L} \quad \ldots (2.3.2)$$

where: S_S is the solubility of nitrogen in the solid, and
S_L is the solubility of nitrogen in the liquid

For most simple alloying systems under atmospheric pressure, this ratio is less than one, resulting in a higher percentage nitrogen in the liquid phase. If the solubility in the liquid is exceeded on further enrichment, the value of *K* approaches 1, nitrogen desorption occurs and porosity results through diatomic nitrogen (N_2) gas evolution.

Segregation is more pronounced in alloys that solidify as primary δ-ferrite rather than primary γ-austenite owing to the lower solubility of nitrogen in ferrite, as shown in Table 2.3.1. Furthermore, and contrasting with the effect of carbon (which is also a strong austenite former), increasing the nitrogen content in the liquid phase does not significantly alter the solidification mode from primary ferritic (F) to primary austenitic (A), or even a mixture of the two, FA and AF [105]. To prevent pore formation at fixed nitrogen additions, the remaining alloying elements in the steel therefore need to be adjusted to increase the nitrogen solubility in the primary ferrite phase or to alter the solidification mode to primary austenite.

As previously stated, the beneficial effects of nitrogen on corrosion resistance, strength and hardness, in the absence of secondary hardening mechanisms, are only realised when nitrogen is in solid solution as an interstitial alloying element. A number of processing techniques are used in the production of high-nitrogen stainless steels to ensure high dissolved nitrogen contents. Such processes include pressurised induction furnace melting, pressurised plasma (arc) furnace melting, pressurised electroslag remelting (PESR), hot isostatic remelting at pressures up to 200 MPa and nitrogen as the pressurising gas, electric arc furnace melting, gas purging, argon-oxygen decarburisation (AOD), arc-slag melting and powder metallurgy [42,72,106,107].

A nitrogen content (in solid solution) exceeding the equilibrium solubility can also be achieved through a combination of applied pressure and powder metallurgy. In the powder metallurgy route, increased nitrogen contents in stainless steel can be achieved by either melting a nitrided stainless steel powder under pressure (HIP), or by enriching molten and pressurised stainless steel with a high-nitrogen powder such as CrN. The nitrogen level of metallic powders may be raised through pressurised gas atomisation, nitriding in a fluidised bed reactor or rotating furnace, HIP nitriding, reactive mechanical alloying or powder injection moulding [42,108].

High pressure processing techniques are most commonly used in the production of nitrogen-alloyed austenitic stainless steels, as nitrogen is both a strong austenite-former and austenite-stabiliser (i.e. it depresses the M_s temperature). High-nitrogen martensitic and duplex stainless steels can be produced successfully at atmospheric pressure using conventional electroslag remelting, as they typically contain lower nitrogen contents than nitrogen-alloyed austenitic stainless steels [72]. High-nitrogen martensitic stainless steels can also be obtained by powder metallurgical processing at atmospheric pressure [109].

The drawbacks of these processes include the high cost and requirement for specialised equipment. This study, therefore, focused on developing an *in-situ* alloying process during laser cladding that will ensure a relatively high nitrogen content at atmospheric pressure in type AISI 410L clad layers and. In addition, it strives to minimise operating costs and to ensure rapid production rates. High nitrogen partial pressures in the shielding and carrier gasses and nitrided metallurgical powders were investigated as viable nitrogen sources.

The principles governing the equilibrium nitrogen dissolution in iron-based alloys play an important role in determining the success of the alloying methods under investigation. Large differences between the nitrogen contents of steels produced under equilibrium and non-equilibrium conditions exist, however, and these conditions therefore warrant further consideration.

2.3.2 Equilibrium dissolution of nitrogen: Effect of temperature

The equilibrium solubility of nitrogen in pure iron and steel, and hence the interstitial nitrogen content, is strongly dependent on temperature. Furthermore, as shown in Table 2.3.1, there is a difference between the nitrogen solubility limits in liquid iron (L), austenite (γ) and ferrite (α or δ). This is evident from Equations (2.3.3) to (2.3.5) that describe the equilibrium constants for nitrogen in pure iron or low alloy steel at a diatomic nitrogen gas pressure of 1 atm for the different phases. These equations are graphically represented in Figure 2.3.1 [110].

$$\log K_{\alpha,\delta} = -\frac{1570}{T} + 2.98 \quad \ldots (2.3.3)$$

$$\log K_{\gamma} = \frac{450}{T} + 2.05 \quad \ldots (2.3.4)$$

$$\log K_{\mathrm{L}} = -\frac{188}{T} + 2.76 \quad \ldots (2.3.5)$$

where: $K_{\alpha,\delta}$, K_{γ} and K_{L} are the equilibrium constants for nitrogen in ferrite (α or δ), austenite (γ) and liquid iron (L), respectively, and
T is the temperature in Kelvin (K).

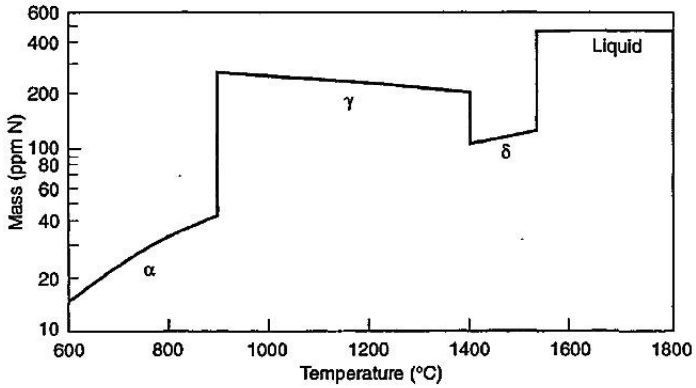

Figure 2.3.1. Equilibrium nitrogen solubility in ferrite (α or δ), austenite (δ) and liquid iron (L) as a function of temperature [110].

The equilibrium nitrogen solubility decreases slightly in liquid iron with a decrease in temperature. In highly alloyed steels and stainless steels, however, the nitrogen solubility in the liquid phase increases marginally as temperature decreases. On solidification the nitrogen solubility limit falls sharply. There is a decrease in the nitrogen solubility in ferrite (α or δ) with decreasing temperature and a linear increase in solubility in austenite (γ). The solubility decreases again on transformation from austenite to α-ferrite as the temperature falls. From Figure 2.3.1, it is evident that the nitrogen solubility is much higher in austenite than in ferrite. This can be attributed to the larger lattice parameter of the face centred cubic (FCC) unit cell of the austenite phase, and the correspondingly larger interstitial openings in the matrix.

2.3.3 Equilibrium dissolution of nitrogen: Effect of pressure

The equilibrium nitrogen content of liquid iron is strongly dependent on the partial pressure of the diatomic nitrogen gas in the atmosphere in direct contact with the surface of the molten metal. The diatomic gas dissociates and is absorbed into the liquid iron in accordance with equation (2.3.6) [110].

$$\tfrac{1}{2}N_2\,(g) = N_{eq}\,(wt\%) \qquad \ldots (2.3.6)$$

The isothermal equilibrium constant, K_{eq}, for this reaction is shown in equation (2.3.7) and rewritten in equation (2.3.8) to yield the equilibrium nitrogen solubility [110].

$$K_{eq} = \frac{N_{eq}\,(wt\%)}{\sqrt{p_{N_2}}} \qquad \ldots (2.3.7)$$

$$N_{eq}\,(wt\%) = K_{eq}\sqrt{p_{N_2}} \qquad \ldots (2.3.8)$$

where: where N_{eq} (wt%) refers to the equilibrium solubility of nitrogen in the liquid iron in weight percentage, and
p_{N_2} is the partial pressure of diatomic nitrogen (N_2) gas in the atmosphere.

This implies that, at constant temperature, the equilibrium nitrogen solubility of liquid iron is directly proportional to the square root of the equilibrium partial pressure of diatomic nitrogen gas in the atmosphere in contact with the liquid metal. This relationship is known as Sievert's Law.

Figure 2.3.2 shows the nitrogen solubility as a function of diatomic nitrogen partial pressure for a 13Cr1Mo stainless steel in the austenite region at three different temperatures. There is a linear relationship between the equilibrium nitrogen solubility and the square root of the partial pressure of N_2 gas, as predicted by Sievert's Law.

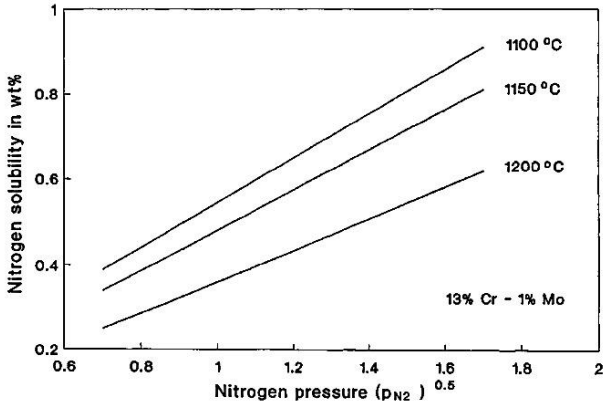

Figure 2.3.2. Equilibrium nitrogen solubility in austenite as a function of diatomic nitrogen partial pressure at three temperatures [111].

When the nitrogen solubility limit is exceeded on cooling, dissolved nitrogen atoms may recombine to form N_2 and degassing occurs in the form of gas bubbles. Nitrogen gas evolution or pore formation is described by equation (2.3.9) [105].

$$P_g < P_a + P_m + P_c \quad \ldots (2.3.9)$$

where: P_g is the gas pressure within a pore,
P_a is atmospheric pressure,
P_m is the hydrostatic pressure of the melt, and
P_c is the capillary pressure, as defined by equation (2.3.10).

$$P_c = \frac{2\sigma}{r} \quad \ldots (2.3.10)$$

where: σ is the surface tension of the pore, and
r is the average pore radius.

Equation (2.3.9) states that pore formation will only occur if the internal pressure within a gas pore exceeds the combined pressures from the atmosphere, the melt and the capillary pressure related to the pore radius. High atmospheric pressure therefore tends to increase the equilibrium nitrogen solubility by suppressing pore formation and degassing.

2.3.4 Equilibrium dissolution of nitrogen: Effect of alloy composition

The equilibrium solubility of nitrogen in iron alloys is strongly influenced by the presence of alloying elements. Figure 2.3.3 shows how an increase in chromium content from 0% to 18.4% increases the nitrogen solubility in binary Fe-Cr alloys as a function of temperature. Comparison with Figure 2.3.1 clearly illustrates how the nitrogen solubility in iron changes with chromium content. A significant increase in the nitrogen solubility in the liquid, ferrite and austenite regions is evident. This increase in nitrogen solubility is due to the negative interaction parameter of chromium with nitrogen in solution. At high levels of chromium there is a slight decrease in nitrogen solubility with increasing temperature in the liquid phase.

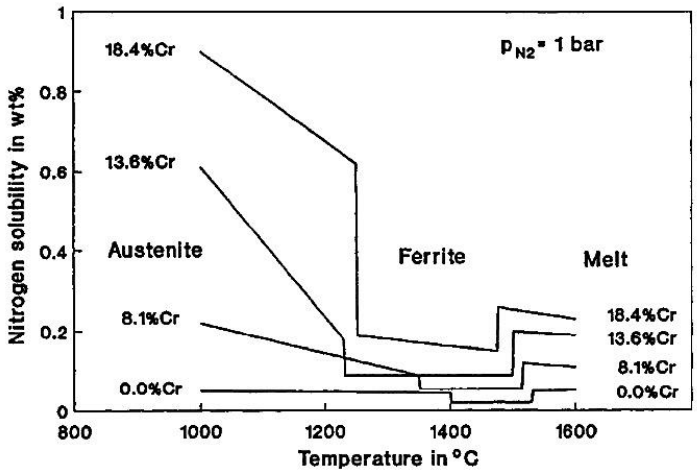

Figure 2.3.3. Equilibrium nitrogen solubility in iron as a function of chromium content and temperature with diatomic nitrogen gas at 1 bar partial pressure [111].

Table 2.3.2 lists the interaction parameters, $e_N^{X_i}$, of various elements, X_i, with nitrogen in iron-based alloys at 1600°C. Satir-Kolorz and Feichtinger [112] compiled this list on the basis of published literature and their own experimental data. A negative interaction parameter indicates that an alloying element increases the nitrogen solubility, whereas a positive parameter implies reduced solubility.

In Table 2.3.2, the elements with the highest negative interaction parameters with nitrogen, i.e. titanium, zirconium, vanadium and niobium, are strong nitride-formers and are therefore not suited to increasing nitrogen solubility when nitride formation is undesirable. These elements are also strong ferrite-formers and therefore not suitable for martensitic stainless steels. As the focus of the current investigation is on the formation of fully martensitic microstructures in martensitic stainless steel, strong ferrite-forming elements were not considered in the design of the experimental alloys.

As stated in Section 2.2.4 and shown in Table 2.3.2, manganese increases the equilibrium solubility of nitrogen in iron-based alloys and plays an important role in the substitution of nickel in high-nitrogen stainless steels.

The positive interaction parameter of carbon with nitrogen emphasises the importance of low carbon contents in raising the nitrogen solubility, and explains the use of low carbon type AISI 410L in this

investigation. It is interesting to note that nitrogen has a positive interaction parameter with itself. This implies that at high nitrogen levels in liquid iron-based alloys, nitrogen lowers its own equilibrium solubility. This suggests that Sievert's Law may not accurately predict nitrogen solubility at high concentrations [112].

Table 2.3.2. Interaction parameters of various alloying elements with nitrogen in iron-based alloys at 1600°C [112].

Element	$e_N^{X_i}$
Titanium	-0.930
Zirconium	-0.630
Vanadium	-0.098
Niobium	-0.050
Chromium	-0.048
Tantalum	-0.033
Manganese	-0.024
Molybdenum	-0.013
Tungsten	-0.002
Cobalt	0.010
Nickel	0.011
Copper	0.006
Arsenic	0.010
Tin	0.008
Antimony	0.010
Aluminium	0.040
Silicon	0.043
Phosphorus	0.048
Boron	0.083
Carbon	0.118
Nitrogen	0.130

Figure 2.3.4 is a graphic representation of the interaction parameters shown in Table 2.3.2, normalised to the effect of chromium. Chromium promotes the equilibrium solubility of nitrogen in iron-based alloys at 1600°C and has a lower nitride-forming tendency than titanium, zirconium, vanadium and niobium. Due to its ferrite-forming tendency, additional chromium was not added to the AISI 410L alloy used in the current investigation.

Figures 2.3.5(a) and (b) show the influence of increasing manganese and nickel contents in iron-based alloys on the equilibrium nitrogen solubility at 1600°C [112]. Manganese contents ranged from 0% to 28% and nickel concentrations from 0% to 25%. Due to its negative interaction parameter with nitrogen, an increase in manganese content resulted in a significant increase in nitrogen solubility, whereas nickel additions resulted in a decrease in nitrogen solubility.

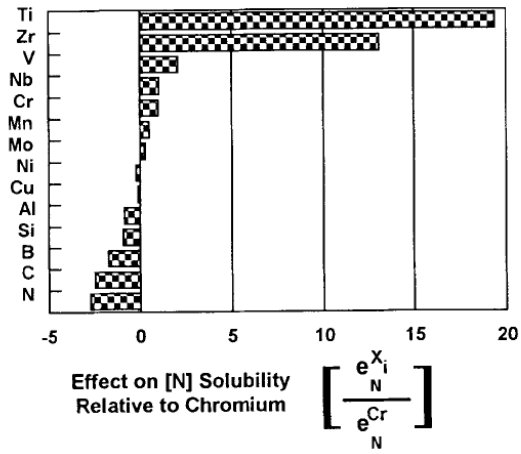

Figure 2.3.4. Interaction parameters of various alloying elements with nitrogen in iron-based alloys at 1600°C [113].

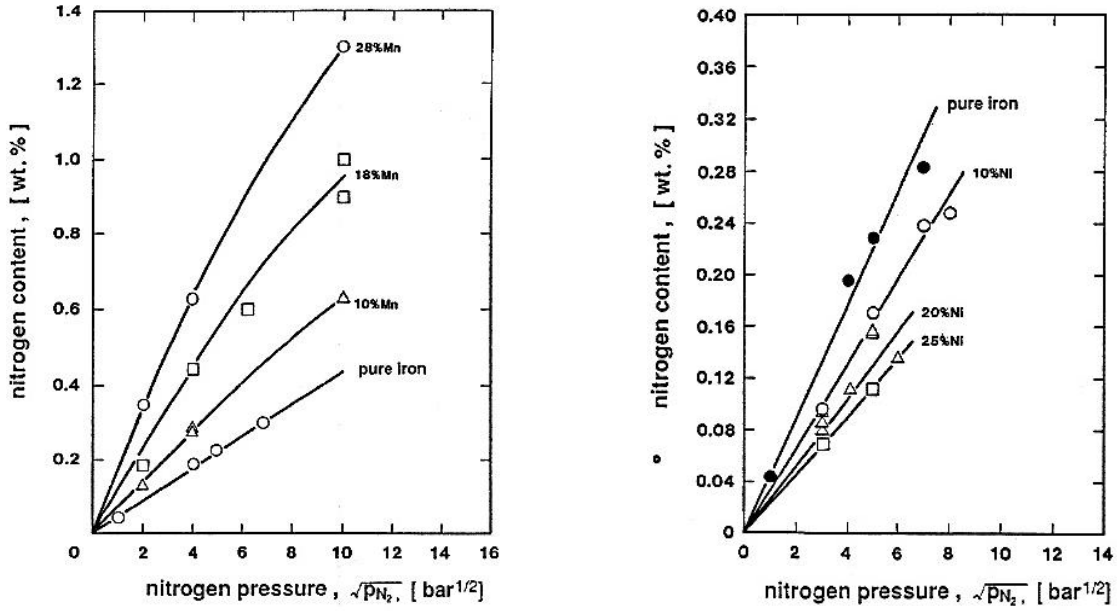

(a) (b)

Figure 2.3.5. The effect of: (a) manganese; and (b) nickel additions, on the nitrogen solubility of iron-based alloys at 1600°C as a function of diatomic nitrogen partial pressure [112].

As shown in equations (2.3.11) and (2.3.12) Wada and Pehlke [114] used Sievert's Law to compile an equation to predict the equilibrium nitrogen solubility of multicomponent iron-based alloys containing chromium, nickel, manganese and molybdenum as principal alloying elements.

$$K_{eq} = a_N\sqrt{p_{N_2}} = f_N(\%N_{eq})\sqrt{p_{N_2}} \quad \ldots (2.3.11)$$

$$\log(\text{wt\% } N_{eq}) = \left(-\frac{274}{T} - 1.22\right) - \left(\frac{4780}{T} - 1.51\right)\left(\log(f_{N,\,1873K})\right) - \left(\frac{1760}{T} - 0.91\right)\left(\log(f_{N,\,1873K})\right)^2 \quad \ldots (2.3.12)$$

where: a_N is the Henrian activity of nitrogen in the liquid multicomponent alloy,
f_N is the activity coefficient of nitrogen in the liquid alloy, and
$f_{N,\,1873K}$ is the activity coefficient of nitrogen in the liquid alloy at 1873 K.

Equation (2.3.12) makes use of the activity coefficient of nitrogen in iron alloys at 1600°C (1873 K) to predict the equilibrium nitrogen solubility as a function of temperature and alloying element content. It holds as long as the requirement $0 \geq \log(f_{N,\,1873K}) \geq -1.4$ is satisfied. The effect of alloying element content on the activity coefficient at 1600°C (1873 K) is given by equation (2.3.13), which also incorporates the effects of C, Si, P, S, Al, Ti, V, W and O [114].

$$\begin{aligned}\log(f_{N,}) = \{&- 164[\%Cr] + 8.33[Ni] - 33.2[\%Mo] - 134[\%Mn] + 1.68[\%Cr]^2 - 1.83[\%Ni]^2 - \\ &2.78[\%Mo]^2 + 8.82[\%Mn]^2 + (1.6\,[\%Ni] + 1.2[\%Mo] + 2.16[\%Mn])[\%Cr] + \\ &(0.26[\%Mo] + 0.09[\%Mn])[\%Ni]\}/T + \{0.0415[\%Cr] + 0.0019[\%Ni] + 0.0064[\%Mo] \\ &+ (0.035[\%Mn] - 0.0006[\%Cr]^2 + 0.001[\%Ni]^2 + 0.0013[\%Mo]^2 - 0.0056[\%Mn]^2 + \\ &(- 0.0009[\%Ni] - 0.0005[\%Mo] - 0.0005[\%Mn])[\%Cr] + (0.0003[\%Mo] + \\ &0.0007[\%Mn])[\%Ni]\} + 0.13[\%C] + 0.06[\%Si] + 0.046[\%P] + 0.007[\%S] + \\ &0.01[\%Al] - 0.9[\%Ti] - 0.1[\%V] - 0.003[\%W] - 0.12[\%O] \qquad \ldots (2.3.13)\end{aligned}$$

where: [%M] is the weight percentage of each alloying element.

The preceding discussion suggests that the nitrogen solubility limit in stainless steels can be increased by increasing the nitrogen partial pressure in the gas atmosphere in contact with the liquid alloy, by increasing the total pressure or by changing the composition of the alloy. The next section considers the applicability of Sievert's Law and the Wada and Pehlke equations during laser processing.

2.3.5 Nitrogen dissolution during laser processing

The formation of a plasma phase over the surface of the weld pool is an inherent feature of most welding processes, including arc, laser and electron beam welding. This plasma phase has a high electron density and contains excited neutral atoms, molecules and ionised gas. The presence of these species in the plasma alters the dissociation behaviour of a diatomic gas such as nitrogen (N_2) from that of a purely diatomic gas-metal system. Sievert's Law and any solubility calculations based on equilibrium thermodynamic considerations are therefore not expected to be valid in the presence of plasma. In fact, the presence of neutral atoms in the plasma leads to increased dissolution of the gaseous species [115].

Numerous authors, including Kuwana *et al.* [116], Palmer *et al.* [117], and Du Toit and Pistorius [118,119], investigated nitrogen dissolution in iron, steel and stainless steel during arc welding and arc melting. These authors reported higher nitrogen dissolution than the solubility values predicted from Sievert's Law for varying nitrogen partial pressures and attributed this effect to high partial pressures of monatomic nitrogen (N) in the plasma.

During laser welding, plasma is created when the metal under laser irradiation evaporates from the surface of the workpiece. The metal vapour forms a plume with low ionisation potential close to the surface and provides the seeding electrons for the creation of gaseous plasma from the shielding gas. At a minimum laser intensity, or threshold intensity, I_i (MW/cm), the laser light is absorbed by the plume and provides sufficient

heating and acceleration of seeding electrons (by a mechanism known as Bremsstrahlung (IB)) for the increase in electron energy to exceed that lost to elastic kinetic interactions between electrons and neutral atoms. At this point, an avalanche effect is initiated which exponentially increases the electron density in the metallic vapour and the gas is ionised. The threshold intensity is strongly dependent on the inverse square of the wavelength of the laser light (λ^{-2}). In simpler terms, laser light with a longer wavelength has a lower ionisation potential [120].

Sato *et al.* [121] conducted comparative experiments with autogenous Nd:YAG laser and arc welds (GTAW and GMAW) on purified iron, Fe-20Cr-10Ni austenitic stainless steel and SUS329J1 duplex stainless steel at increasing diatomic nitrogen partial pressures in Ar-N_2 shielding gas mixtures. These authors used a laser power of 3.5 kW, a welding speed of 0.02 m/s and gas mixtures with nitrogen partial pressures ranging from 0.0 to 1.0 atmosphere N_2. GTAW was conducted on purified iron at a welding current of 250 A, with an arc length of 10 mm and a travel speed of 3.3 mm/s. GTAW and GMAW trials were conducted on the Fe-20Cr-10Ni stainless steel at 250 A, an arc length of 5 mm and a travel speed of 2.5 mm/s. The same parameters were used for GTAW of SUS329J1 stainless steel. Figure 2.3.6 shows the weld metal nitrogen contents of the three materials as a function of the nitrogen partial pressure, p_{N_2}. The equilibrium nitrogen solubility of each material, calculated by means of the Wada and Pehlke equations (2.3.12) and (2.3.13) at measured weld pool temperatures of 1900 K, 1800 K and 1880 K is shown in Figures 2.3.6(a), (b) and (c), respectively. Also indicated on these figures is the calculated equilibrium nitrogen solubility at the boiling temperature of each respective material. The temperature of the laser weld pool is assumed to be between the arc weld pool temperature and the boiling point of the material.

There is usually a rapid increase in the nitrogen content of gas tungsten arc welds at low N_2 partial pressures, followed by a plateau stage at higher partial pressures of N_2 when nitrogen absorption from the arc plasma is balanced by nitrogen desorption from the weld pool [116]. Gas tungsten arc welded specimens also consistently have nitrogen contents exceeding the calculated equilibrium solubility due to the presence of monatomic nitrogen in the arc plasma. Gas metal arc welded specimens generally exhibit less nitrogen pick-up than gas tungsten arc welded specimens and have weld metal nitrogen contents lower than the calculated equilibrium nitrogen solubility at the weld pool temperature.

The nitrogen contents of Nd:YAG laser welded specimens increase slightly with N_2 partial pressure, but are considerably lower than those of the gas tungsten arc welded specimens in Figures 2.3.6(a), (b) and (c). The laser welded nitrogen contents are lower than the calculated equilibrium contents in Figures 2.3.6(a) and (b) and only exceeds the calculated equilibrium content in Figure 2.3.6(c) at the temperature of the arc weld pool at low N_2 partial pressures. This is due to the high initial nitrogen content of SUS329J1 duplex stainless steel prior to welding. Unlike the behaviour observed during arc welding, the nitrogen contents of Nd:YAG welded specimens do not level off at increasing partial pressures. The nitrogen levels do not reach the calculated equilibrium nitrogen contents in most cases and prominent nitrogen degassing therefore does not occur during Nd:YAG welding in Ar-N_2 shielding gas mixtures. The authors proposed three reasons for the

lower nitrogen contents of the laser welded specimens. Less time is available for nitrogen absorption during laser welding than during arc welding due to the shorter thermal cycle. Not enough time is therefore allowed for the nitrogen contents to reach the calculated equilibrium values. The second reason is the presence of high metal vapour pressure above the weld pool of the laser welded specimens. This effect is prominent during both keyhole and conduction mode welding, but is more pronounced during keyhole welding. The increase in metal-vapour partial pressure (p_{Fe}) results in the formation of a barrier to nitrogen absorption by reducing the partial pressure of N_2 in the shielding atmosphere. Equations (2.3.14) and (2.3.15) describe the formation of iron vapour and are graphically represented in Figure 2.3.7 [121]. In this figure, the equilibrium nitrogen solubility of liquid iron in the absence of iron vapour (calculated from the equations of Wada and Pehlke), N (calc.), is extrapolated from the measured nitrogen content, N (correct), at ambient pressure.

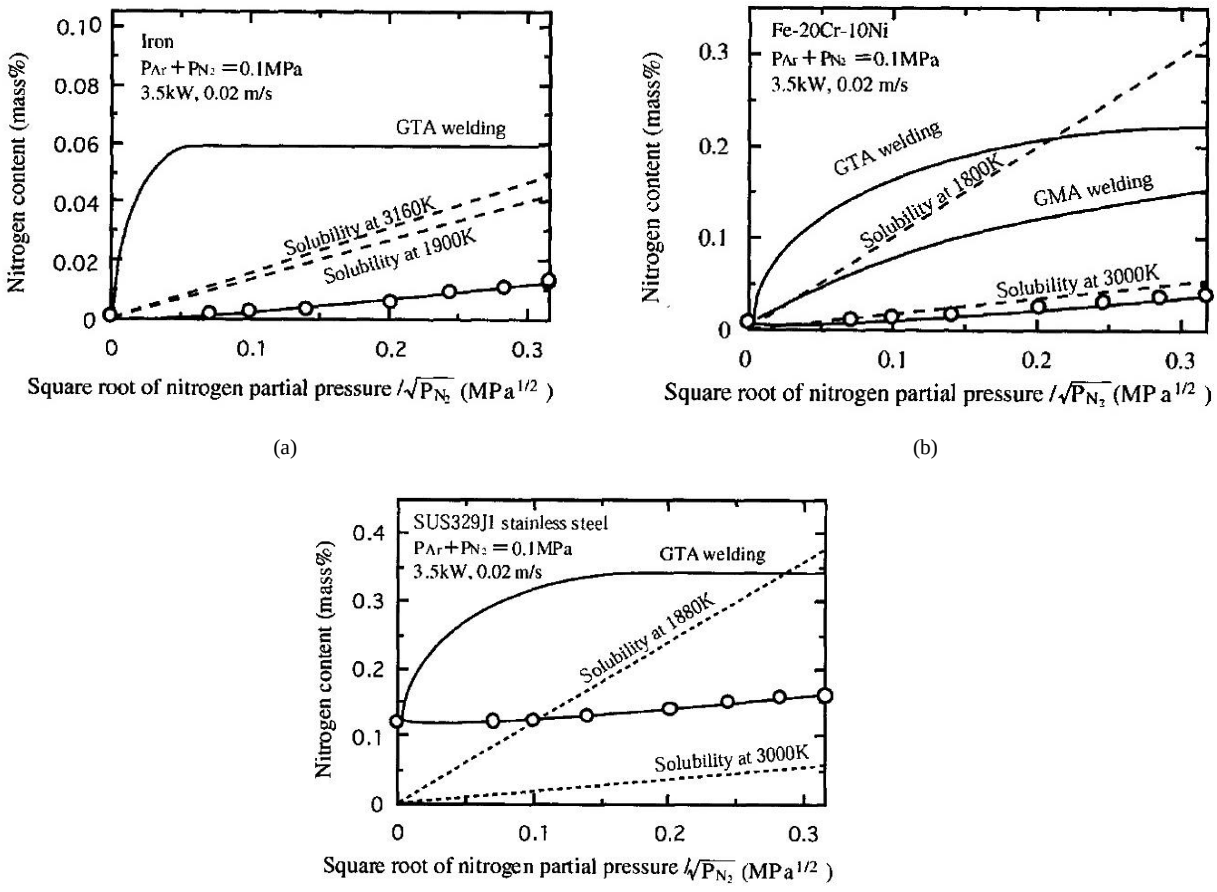

Figure 2.3.6. The nitrogen content of Nd:YAG laser and arc welds as a function of the square root of the nitrogen partial pressure in Ar-N_2 gas mixtures for: (a) purified iron; (b) Fe-20Cr-10Ni austenitic stainless steel; and (c) SUS329J1 duplex stainless steel, compared to the calculated equilibrium nitrogen solubility at the measured weld pool temperature and the boiling temperature [121].

$$\mathrm{Fe}\ (\ell) = \mathrm{Fe}\ (g) \qquad \ldots (2.3.14)$$

$$\log p_{Fe}\ (\mathrm{mm.Hg}) = -19710\ T^{-1} - 1.2 \log T + 13.27 \qquad \ldots (2.3.15)$$

where: p_{Fe} is the partial pressure of gaseous iron in the atmosphere, and
T is temperature (K).

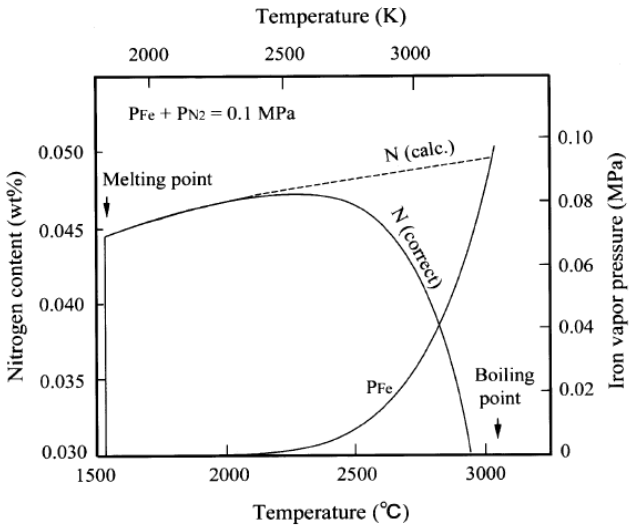

Figure 2.3.7. The influence of increasing iron vapour pressure on the nitrogen solubility in pure iron, N (correct), as a function of temperature at a constant ambient pressure of 1 atmosphere (0.1 MPa), compared to the calculated equilibrium nitrogen solubility, N (calc.) [121].

The measured nitrogen content of liquid iron, shown in Figure 2.3.7, decreases from a maximum value of 0.047% with an increase in p_{Fe}, and approaches zero at the boiling point of iron where p_{Fe} reaches a maximum. During laser welding, the metal vapour forms a much more dense cover over the surface of the weld pool than during arc welding. Nitrogen absorption is therefore expected to be different for the two processes.

Sato *et al.* [121] postulated a third reason for the lower nitrogen levels of Nd:YAG laser welded specimens, namely that due to the shorter wavelength of the Nd:YAG laser, insufficient laser absorption by the metal-vapour plume occurs, resulting in a low plasma temperature and a low density of monatomic nitrogen (in accordance with the temperature dependence of N_2 dissociation). To test this hypothesis, Dong *et al.* [122] performed autogenous gas tungsten arc and laser welding on the same materials as those used by Sato *et al.*, replacing the Nd:YAG laser (with a wavelength of 1.06 μm) with a CO_2 laser (with a wavelength of 10.6 μm). Laser welding was performed at a laser power of 5.0 kW and a travel speed of 0.02 m/s. The gas tungsten arc welding parameters were selected to ensure similar weld bead dimensions to those of the laser welds. This eliminated the effect of weld bead area ratio on nitrogen absorption, as the surface area of the bead influences the absorption kinetics. The welding current was set at 150 A, the arc length at 1 mm and the travel speed at 3.33 mm/s. Their results are shown in Figures 2.3.8(a), (b) and (c) for purified iron, Fe-20Cr-10Ni austenitic stainless steel and SUS329J1 duplex stainless steel, respectively. For comparative purposes, the authors included the results from the Nd:YAG study by Sato *et al.* [121]. Also shown are the calculated equilibrium nitrogen solubilities for each material at the arc weld pool temperature and boiling point for increasing nitrogen partial pressure.

In Figures 2.3.8(a), (b) and (c), the nitrogen contents of the CO_2 laser welded specimens fall between those of gas tungsten arc welded and Nd:YAG laser welded specimens. At low nitrogen partial pressures, the

nitrogen contents of CO_2 welded specimens consistently exceed the calculated equilibrium nitrogen solubilities at both the weld pool and boiling temperatures for all three materials tested. This suggests that monatomic nitrogen (N) is present in the plasma above the weld pool, enhancing nitrogen dissolution in the liquid metal during CO_2 laser welding.

The difference in nitrogen content between the laser welds and the arc welded specimens can be attributed to the reasons proposed by Sato *et al*. [121], i.e. less absorption time during the shorter thermal cycle and high metal vapour pressure, p_{Fe}, which retards nitrogen absorption from the plasma. The levelling off of the nitrogen content below the calculated equilibrium nitrogen solubility at high diatomic nitrogen partial pressures is attributed to the higher weld pool temperatures of the CO_2 laser welds. The nitrogen solubility limit in highly alloyed steels decreases with an increase in temperature, as is evident from the calculated equilibrium values in Figures 2.3.8(b) and (c). This is not the case for pure iron, as shown in Figure 2.3.8(a). This suggests that nitrogen desorption from the weld pool will occur at much lower nitrogen contents during CO_2 laser welding of stainless steel [122].

Dong *et al.* [122] attributed the difference in the measured nitrogen contents of CO_2 and Nd:YAG laser welded specimens to the difference in wavelength between the two lasers. A CO_2 laser has a typical threshold laser intensity range (below which plasma cannot form) of $1.0x10^6$ to $3.0x10^6$ W/cm^2. For a Nd:YAG laser, the threshold laser intensity is $1.0x10^8$ W/cm^2, making it less likely for strong plasma to develop during Nd:YAG laser welding. The temperatures above CO_2 laser weld pools were shown to exceed the typical temperatures of arc plasmas, being sufficiently high for diatomic nitrogen dissociation into monatomic nitrogen. Temperatures above Nd:YAG laser weld pools were observed to be below those required for successful N_2 dissociation and the probability of forming a dense monatomic nitrogen-containing plasma is therefore considerably lower.

Dong *et al*. [123] subsequently confirmed, through monochromatic photography, that there is little difference between the plasmas formed during CO_2 welding and gas tungsten arc welding, but that metallic vapour is more concentrated over CO_2 laser weld pools than arc welds. These authors also showed that similar nitrogen contents to those measured during Nd:YAG laser welding could be achieved during CO_2 laser welding when plasma formation was suppressed in a reduced ambient pressure nitrogen atmosphere.

Zhao *et al.* [124] investigated the influence of heat input during CO_2 welding on the nitrogen solubility of 1Cr22Mn16N austenitic stainless steel at increasing nitrogen partial pressures in Ar-N_2 shielding gas mixtures. It is evident from Figure 2.3.9 that an increase in heat input in a 100% argon atmosphere leads to lower nitrogen contents in the weld metal. This is due to increased nitrogen desorption from the weld pool. At higher heat input levels the weld cooling time is longer, allowing more time for desorption to occur. When nitrogen is added to the shielding gas, the weld metal nitrogen content increases with an increase in heat input. This is ascribed to an increase in the surface area of the liquid pool available for nitrogen adsorption and a longer weld thermal cycle, which increases the time available for adsorption.

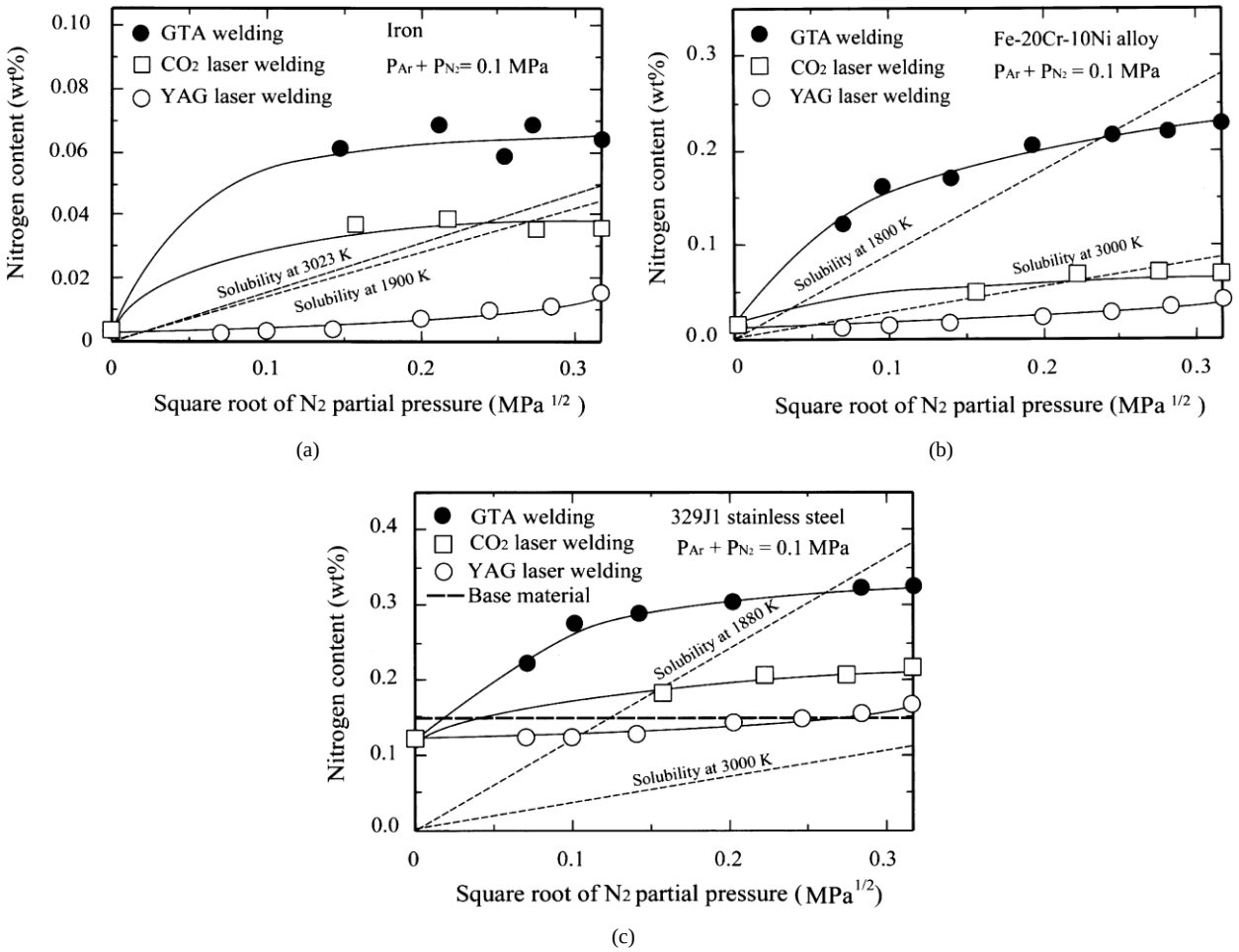

Figure 2.3.8. The influence of nitrogen partial pressure in Ar-N_2 gas mixtures on the nitrogen contents of Nd:YAG laser, CO_2 laser and gas tungsten arc welds in: (a) purified iron; (b) Fe-20Cr-10Ni austenitic stainless steel; and (c) SUS329J1 duplex stainless steel, compared to the calculated equilibrium nitrogen solubilities at the measured arc weld pool temperature and the boiling temperature [122].

Based on these results, the authors demonstrated that a critical boundary exists in the form of a balance between the amount of nitrogen in the shielding gas and the heat input above which porosity does not occur. This is illustrated in Figure 2.3.10 for 1Cr22Mn16N austenitic stainless steel. Porosity can be avoided at higher diatomic nitrogen partial pressures, p_{N2}, and at high heat inputs where there is enhanced nitrogen solubility. At higher heat inputs, the slower cooling rates allow the escape of nitrogen bubbles from the melt pool before solidification [124].

2.3.6 Si_3N_4 powder as alternative source for nitrogen

Due to the low nitrogen solubility from the atmosphere during Nd:YAG laser welding, alternative nitrogen sources were considered for the current project. One such alternative nitrogen source is the addition of nitrided powders to the powder feed. Powders similar in chemical composition to the nitrided granulated additives used during pressurised electroslag remelting were considered. These granulated particles are typically mixtures of FeCrN, consisting of 8 to 10 wt% atomic nitrogen (N), CrN (4 to 10 wt% N) or Si_3N_4 (25 to 30 wt% N) [86]. Si_3N_4 was selected for this investigation on account of its high contribution of atomic

nitrogen on dissociation. Furthermore, silicon is an effective deoxidiser and improves the high-temperature oxidation and scaling resistance of stainless steels [72].

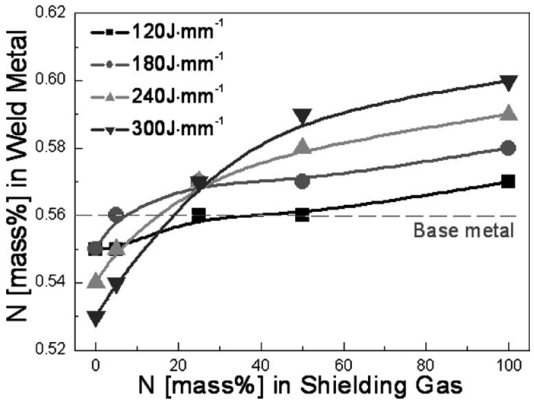

Figure 2.3.9. Nitrogen solubility of austenitic stainless steel as a function of the nitrogen content in the shielding gas and the heat input [124].

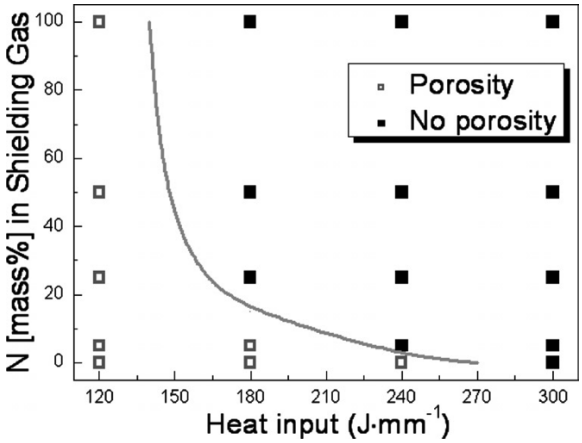

Figure 2.3.10. Critical boundary between the amount of nitrogen in the shielding gas and heat input where porosity-free welds can be made during CO_2 laser welding of 1Cr22Mn16N austenitic stainless steel [124].

Huang *et al.* [125-131] and other authors [132-134] performed extensive research on the laser surface alloying (LSA) and laser surface cladding (LSC) of carbon steel with stainless steel and Si_3N_4 mixtures. The alloy systems investigated were of the forms Fe-Cr-Si_3N_4, Fe-Cr-Mo-Si_3N_4, Fe-Cr-Ni-Si_3N_4 and Fe-Cr-Mn-Si_3N_4, including AISI 430 ferritic and S42000 martensitic stainless steel powders mixed with Si_3N_4. All of these authors used CO_2 lasers ranging in power from 0.4 kW to 4.5 kW, and either argon or nitrogen as shielding gas. The authors made no reference with regards to observed porosity.

An important consideration during laser cladding and alloying with metallurgical powders such as Si_3N_4 is the extent of dissociation during processing. Si_3N_4 decomposes in the temperature range 1800°C to 1900°C [125]. Various authors observed that at the temperatures of laser irradiation, Si_3N_4 dissociates completely in the surface layers during laser processing [125,130,133] in accordance with equation (2.3.16) [130].

$$Si_3N_4 \rightarrow 3Si + 4N \quad \ldots (2.3.16)$$

Table 2.3.3 shows the alloy systems investigated by Huang *et al.* [125,127-131] and the corresponding weld nitrogen contents achieved in each respective system through the addition of Si_3N_4. An increase in nitrogen content from 0.008 wt% to 0.35 wt% was achieved in the Fe-30Cr-1.5Si_3N_4 system and a maximum nitrogen content of 0.83 wt% was achieved in the Fe-25Cr-25Mn-2Si_3N_4 system. The difference between the nitrogen content in this system and that in the Fe-25Cr-25Ni-2Si_3N_4 system (0.38 wt%) can be attributed to the high manganese content in the Fe-25Cr-25Mn-2Si_3N_4 system, which increases the nitrogen solubility, and the high nickel content in the Fe-25Cr-25Ni-2Si_3N_4 system, which decreases the nitrogen solubility (as shown in Table 2.3.2).

Table 2.3.3. The alloy systems examined by Huang *et al.* [125,127-129,131] and the corresponding nitrogen contents obtained after laser surface treatments.

Alloy System	N (wt%)	Reference
Fe-30Cr-1.5Si_3N_4	0.35	[125,128]
Fe-30Cr-2Si_3N_4	0.52	[129]
Fe-30Cr-2Si_3N_4	0.63	[129]
Fe-30Cr-5Mo-2Si_3N_4	0.58	[129]
Fe-25Cr-25Mn-2Si_3N_4	0.83	[131]
Fe-25Cr-25Ni-2Si_3N_4	0.38	[131]
Fe-25Cr-15Ni-2Si_3N_4	0.40	[127]
Fe-25Cr-15Ni-8Mo-2Si_3N_4	0.48	[127]

An increase in the deposit nitrogen content improved the pitting corrosion resistance in de-aerated 3.5% NaCl solutions in all the alloy systems shown in Table 2.3.3 [126-129,131,132]. Furthermore, lower oxygen levels were reported due to an increase in deposit silicon content [125,128-131,133]. As shown in equation (2.3.17), silicon reacts with oxygen to form SiO_2, which is rejected to the slag that forms on the laser treated surfaces [130].

$$Si + 2O \rightarrow SiO_2 \quad \ldots (2.3.17)$$

Figure 2.3.11(a) shows the increase in hardness observed by Sha and Tsai [134] during hardfacing of carbon steel with mixed powders of S42000 martensitic stainless steel and Si_3N_4, and Figure 2.3.11(b) shows the consequent decrease in wear rate, as tested by means of a pin-on-disk continuous sliding test under loads of 4 kg and 5 kg. The increase in hardness and the reduction in wear rate are due to the interstitial solid solution hardening caused by nitrogen and, to a lesser extent, the substitutional solid solution strengthening caused by silicon not bonded to oxygen as SiO_2. These authors found a steady increase in silicon content with an increase in Si_3N_4 powder addition, and although they reported a general increasing trend in the nitrogen content, found significant scattering in the individual nitrogen analyses.

More recently, Brytan *et al.* [135] demonstrated that the laser surface alloying of various sintered stainless steels, including sintered AISI 410L ferritic stainless steel with nitrogen, is possible using preplaced Si_3N_4

powder as nitrogen source. A 2.3 kW high power diode laser (HPDL) with argon shielding gas was used in this study. The authors observed an increase in the amount of martensite in the microstructure of the AISI 410L stainless steel after laser irradiation and an increase in hardness up to a maximum value of 450 HV (hardness on the Vickers scale).

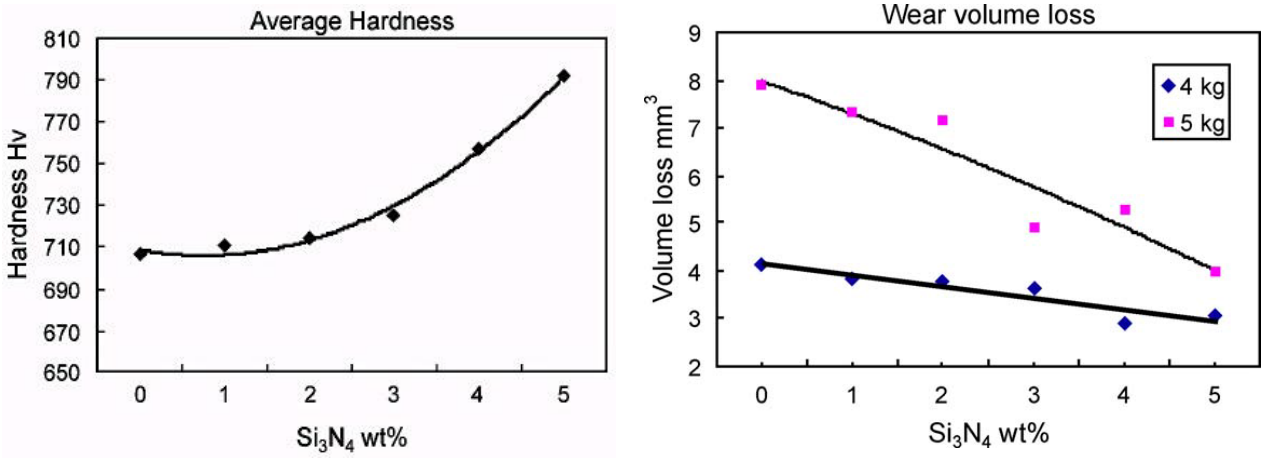

(a) (b)

Figure 2.3.11. Influence of increasing Si_3N_4 content on the: (a) hardness; and (b) wear rate of S42000 martensitic stainless steel after laser cladding [134].

Paczkowska [136] successfully alloyed surface layers of nodular cast iron with nitrogen using preplaced Si_3N_4-containing paste as nitrogen source. A continuous wave CO_2 laser was used in this study. Paczkowska found that the hardness of the surface layers was at least three times higher than the original hardness of the cast iron prior to laser treatment. The study showed that laser surface alloying of cast iron with nitrogen was possible with Si_3N_4.

2.4 SUMMARY

According to the published literature, achieving high nitrogen contents, or even equilibrium nitrogen contents, in ferrous alloys from dissolution of nitrogen from the atmosphere is not possible during welding and cladding using Nd:YAG lasers. The short thermal cycle does not allow enough time for nitrogen pick-up from the diatomic nitrogen-containing atmosphere. Sievert's Law therefore cannot be used to predict the nitrogen contents of laser clad layers. Unlike during arc welding or CO_2 laser welding, there is insufficient laser absorption by the gaseous metal plume above the weld pool during Nd:YAG laser welding, resulting in the formation of a low temperature plasma, or even completely suppressing plasma formation. Under these conditions, insufficient monatomic nitrogen forms in the atmosphere to enhance solubility.

Nd:YAG laser welding or cladding in a nitrogen-containing atmosphere is therefore not suitable for alloying stainless steel with nitrogen. Alloying with nitrided metallurgical powders and high-nitrogen ceramic powders such as Si_3N_4 could provide an alternative alloying method capable of delivering high-nitrogen contents to martensitic stainless steel clad layers.

Martensitic stainless steels are generally considered to be high in nitrogen when the nitrogen content exceeds about 0.08 wt%. Huang *et al.* [125-131] confirmed that high nitrogen contents can be attained in austenitic and ferritic stainless steels by means of Si_3N_4 powder additions and it therefore seems plausible that high nitrogen contents could also be achieved in martensitic stainless steels using this method. Manganese additions can be used to increase the nitrogen solubility limit of the martensitic stainless steel deposit. Despite its positive interaction parameter with nitrogen, nickel may also indirectly increase the nitrogen solubility of martensitic stainless steels by enlarging the high temperature austenite phase field. Since martensite can only form from rapidly cooled high temperature austenite, an increase in the nitrogen content of the high temperature austenite phase should result in the formation of high nitrogen martensite at room temperature. The objectives of this investigation are considered in more detail in Chapter 3.

2.5 REFERENCES

[1] Vollertsen, F., Partes, K., Meijer, J. *State of the art of laser hardening and cladding*. Proceedings of the 3rd International WLT-Conference on Lasers in Manufacturing, held in Munich, Germany, on 13-16 June 2005. pp. 281-305.

[2] Dini, J.W. *Laser surface modification offers promise for various coating processes and substrates.* Metal Finishing, vol. 95, no. 10. 1997. pp. 10-14.

[3] Toyserkani, E., Khajepour, A., Corbin, S.F. *Laser cladding*. CRC Press, Boca Raton, FL. 2005.

[4] Riabkina-Fishman, M., Zahavi, J. *Laser alloying and cladding for improving surface properties.* Applied Surface Science, vol. 106. 1996. pp. 263-267.

[5] Arnold, J., Volz, R. *Laser powder technology for cladding and welding*. Journal of Thermal Spray Technology, vol. 8, no. 2. 1999. pp. 243-248.

[6] Vilar, R. *Laser cladding*. Journal of Laser Applications, vol. 11, no. 2. 1999. pp. 64-79.

[7] Vilar, R. *Laser cladding.* Proceedings of the International Society for Optical Engineering, vol. 5147. 2003. pp. 385-392.

[8] Dubourg, L., Archambeault, J. *Technological and scientific landscape of laser cladding process in 2007.* Surface and Coatings Technology, vol. 202, no. 24. 2008. pp. 5863-5869.

[9] Vuoristo, P., Vihinen, J. *High-performance laser coatings for manufacturing and maintenance of industrial components and equipment.* Kunnossapito, vol. 5. 2002. pp. 1-8.

[10] Sexton, L., Lavin, S., Byrne, G., Kennedy, A. *Laser cladding of aerospace materials.* Journal of Materials Processing Technology, vol. 122. 2002, pp. 63-68.

[11] Song, J., Deng, Q., Chen, C., Hu, D., Li, Y. *Rebuilding of metal components with laser cladding forming*. Applied Surface Science, vol. 252. 2006. pp. 7934-7940.

[12] Costa, L., Vilar, R. *Laser powder deposition*. Rapid Prototyping Journal, vol. 15, no. 4. 2009. pp. 264-279.

[13] Torims, T. *The application of laser cladding to mechanical component repair, renovation and regeneration.* DAAAM International, Vienna. 2013. pp. 587-608.

[14] Anderson, T. *Laser resurfacing for industry and mining - A practical overview.* Proceedings of the 49th Annual Conference of the Welding Technology Institute of Australia (WTIA), held in Adelaide, Australia, on 8-10 October 2001.

[15] ASM International. *ASM Handbook Volume 14B - Metalworking: Sheet Forming*. ASM International, Materials Park, OH. 2009. pp. 113-114.

[16] Olsen, F.O. *Hybrid laser-arc welding.* Woodhead Publishing, Oxford. 2009. pp. 58.

[17] American Welding Society. *Welding Handbook Volume 3 - Welding Processes, Part 2.* American Welding Society, Miami, FL. 2007. pp. 540-541.

[18] Weisheit, A., Backes, G., Stromeyer, R., Gasser, A., Wissenbach, K., Poprawe, R. *Powder injection: The key to reconditioning and generating components using laser cladding.* Proceedings of the International Congress on Advanced Materials, their Processes and Applications, held in Munich, Germany, on 1-4 October 2001.

[19] Kaierle, S., Barroi, A., Noelke, C., Hermsdorf, J., Overmeyer, L., Haferkamp, H. *Review on laser deposition welding: From micro to macro.* Physics Procedia, vol. 39. 2012. pp. 336-345.

[20] Kathuria, Y.P. *Laser-cladding process: A study using stationary and scanning CO_2 laser beams.* Surface and Coatings Technology, vol. 97, no. 1-3. 1997. pp. 442-447.

[21] Huang, F.X., Jiang, Z.H., Liu, X.M., Lian, J.S., Chen, L. *Effects of process parameters on microstructure and hardness of layers by laser cladding.* ISIJ International, vol. 51, no. 3. 2011. pp. 441-447.

[22] Qian, M., Lim, L.C., Chen, Z.D., Chen, W.I. *Parametric studies of laser cladding process.* Journal of Materials Processing Technology, vol. 63, no. 1-3. 1997. pp. 590-593.

[23] Pelletier, J.M., Sahour, M.C., Pilloz, M., Vannes, A.B. *Influence of processing conditions on geometrical features of laser claddings obtained by powder injection.* Journal of Materials Science, vol. 28, no. 19. 1993. pp. 5184-5188.

[24] Sexton, C.L., Byrne, G., Watkins, K.G. *Alloy development by laser cladding: An overview.* Journal of Laser Applications, vol. 13, no. 2. 2001. pp. 2-11.

[25] De Oliveira, U., Ocelík, V., De Hosson, J.Th.M. *Analysis of coaxial laser cladding processing conditions.* Surface and Coatings Technology, vol. 197, no. 2-3. 2005. pp. 127-136.

[26] Sun, S., Durandet, Y., Brandt, M. *Parametric investigation of pulsed Nd:YAG laser cladding of Stellite 6 on stainless steel.* Surface and Coatings Technology, vol. 194, no. 2-3. 2005. pp. 225-231.

[27] Chryssolouris, G., Zannis, S., Tsirbas, K., Lalas, C. *An experimental investigation of laser cladding.* CIRP Annals - Manufacturing Technology, vol. 51, no. 1. 2002. pp. 145-148.

[28] Li, Y., Yang, H., Lin, X., Huang, W., Li, J., Zhou, Y. *The influences of processing parameters on forming characterizations during laser rapid forming.* Materials Science and Engineering A, vol. 360, no. 1-2. 2003. pp. 18-25.

[29] Steen, W.M., and Courtney C.G.H. *Hardfacing of Nimonic 75 using 2 kW continuous-wave CO_2 laser.* Metals Technology, vol. 7, no. 6. 1980. pp. 232-237.

[30] Wu, X., Zhu, B., Zeng, X., Hu, X., Cui, K. *Critical state of laser cladding with powder auto-feeding.* Surface and Coatings Technology, vol. 79, no. 1-3. 1996. pp. 200-204.

[31] Dahmen, M., Janzen, V., Lindner, S., Wagener, R. *Laser beam welding of ultra-high strength chromium steel with martensitic microstructure.* Physics Procedia, vol. 56. 2014. pp. 525-534.

[32] Dowson, P., Bauer, D., Laney, S. *Selection of materials and materials related processes for centrifugal compressors and steam turbines in the oil and petrochemical industry.* Proceedings of the 37th Turbomachinery Symposium, held in Houston, TX, on 8-11 September 2008. pp. 189-209.

[33] Avner, S.H. *Introduction to Physical Metallurgy*. McGraw-Hill, Singapore. 1974. pp 349-367.

[34] Garcia de Andrés, C., Alvaréz, L.F., López, V. *Effects of carbide-forming elements on the response to thermal treatment of the X45Cr13 martensitic stainless steel*. Journal of Materials Science, vol. 33. 1998. pp 4095-4100.

[35] Kotecki, D.J. *Alloy recovery in 12% chromium continuous caster roll welding*. Welding Journal, vol. 73, no. 1. 1994. pp. 16-23.

[36] Bhaduri, A.K., Gill, T.P.S., Albert, S.K., Shanmugam, K., Iyer, D.R. *Repair welding of cracked steam turbine blades using austenitic and martensitic stainless-steel consumables.* Nuclear Engineering and Design, vol. 206, no. 2-3. 2001, pp. 249-259.

[37] Klueh, R.L., Harries, D.R. *High-chromium ferritic and martensitic steels for nuclear applications.* ASTM International, West Conshohocken, PA. 2001. pp. 10-11.

[38] Kathuria, Y.P. *Some aspects of laser surface cladding in the turbine industry.* Surface and Coatings Technology, vol. 132, no. 2-3. 2000. pp. 262-269.

[39] Bendeich, P., Alam, N., Brandt, M., Carr, D., Short, K., Blevins, R., Curfs, C., Kirstein, O., Atkinson, G., Holden, T., Rogge, R. *Residual stress measurements in laser clad repaired low pressure turbine blades for the power industry.* Materials Science and Engineering A, vol. 437, no. 1. 2006, pp. 70-74.

[40] Asevedo, C.R.F., Sinátora, A. *Erosion-fatigue of steam turbine blades.* Engineering Failure Analysis, vol. 16, no. 7. 2009. pp. 2290-2303.

[41] Klotz, U.E., Solenthaler, C., Ernst, P., Uggowitzer, P.J., Speidel, M.O. *Alloy compositions and mechanical properties of 9-12% chromium steels with martensitic-austenitic microstructure.* Materials Science and Engineering A, vol. 272, no. 2. 1999. pp. 292-299.

[42] Hänninen, H., Romu, J., Ilola, R., Tervo, J., Laitinen, A. *Effects of processing and manufacturing of high nitrogen-containing stainless steels on their mechanical, corrosion and wear properties.* Journal of Materials Processing Technology, vol. 117, no. 3. 2001. pp. 424-430.

[43] Loosen, B. *Surfacing continuous casting rollers*. Svetsaren, vol. 50, no. 2. 1995. pp. 29-31.

[44] Du Toit, M., Van Niekerk, J. *Improving the life of continuous casting rolls through submerged arc cladding with nitrogen-alloyed martensitic stainless steel*. Welding in the World, vol. 54, no. 11-12. 2010. pp. 342-349.

[45] Shepeleva, L., Medres, B., Kaplan, W.D., Bamberger, M., Wiesheit, A. *Laser cladding of turbine blades*. Surface and Coatings Technology, vol. 125, no. 1-3. 2000. pp. 45-48.

[46] Sanz, A. *New coatings for continuous casting rolls.* Surface and Coatings Technology, vol. 177-178. 2004. pp. 1-11.

[47] Burger, H. *Laser engineering: Enabling SA industry to improve its global competitiveness*. ScienceScope, vol. 6, no. 4. 2013. pp. 15.

[48] Rombouts, M., Meneve, J., Robberecht, D., Geerinckx, E., Gedopt, J. *Laser cladding: A versatile proactive and reactive technology.* Asset Management and Maintenance Journal, vol 24, no. 1. 2011. pp. 7-10

[49] Zhao, J.-C., Notis, M.R. *Continuous cooling transformation kinetics versus isothermal transformation kinetics of steels: A phenomenological rationalization of experimental observations.* Materials Science and Engineering R, vol. 15, no. 4-5. 1995. pp. 135-207.

[50] Tsai, M.C., Chiou, C.S., Du, J.S., Yang, J.R. *Phase transformation in AISI 410 stainless steel.* Materials Science and Engineering A, vol. 322, no. 1-2. 2002. pp. 1-10.

[51] Hemmati, I., Ocelík, V., De Hosson, J.Th.M. *The effect of cladding speed on phase constitution and properties of AISI 431 stainless steel laser deposited coatings.* Surface and Coatings Technology, vol. 205, no. 21-22. 2011. pp. 5235-5239.

[52] Yang, H.-S., Bhadeshia, H.K.D.H. *Austenite grain size and the martensite-start temperature.* Scripta Materialia, vol. 60, no. 2. 2009. pp. 493-495.

[53] Abbaschian, R., Abbaschian, L., Reed-Hill, R.E. *Physical metallurgy principles*. Cengage Learning, Stamford. 2010, pp. 182, 542.

[54] Vamsi Krishna, B., Bandyopadhyay, A. *Surface modification of AISI 410 stainless steel using laser engineered net shaping (LENS^{TM}).* Materials and Design, vol. 30, no. 5. 2009. pp. 1490-1496.

[55] Hemmati, I., Ocelík, V., De Hosson, J.Th.M. *Microstructural characterization of AISI 431 martensitic stainless steel laser-deposited coatings.* Journal of Materials Science, vol. 46, no. 10. 2011. pp. 3405-3414.

[56] Van Rooyen, C., Burger, H.P., Du Toit, M. *Laser metal deposition microstructure of modified low-C martensitic stainless steel.* African Fusion. November 2012. pp. 16-27.

[57] David, S.A., Vitek, J.M., Hebble, T.L. *Effect of rapid solidification on stainless steel weld metal microstructures and its implications on the Schaeffler diagram.* Welding Journal, vol. 66, no. 10. 1987. pp. 289-300.

[58] Van Rooyen, C., Burger, H.P., Kazadi, B.P. *Microstructure of laser cladded martensitic stainless steel.* IIW document IX-H-636-06. International Institute of Welding, Paris. 2006.

[59] American Welding Society. *Welding Handbook Volume 4 - Materials and applications, Part 1.* American Welding Society, Miami, FL. 2011. pp. 285.

[60] Capdevila, C., Caballero, F.G., Garcia de Andrés, C. *Determination of Ms temperature in steels. A Bayesian neural network model.* ISIJ International, vol. 42, no. 8. 2002. pp. 894-902.

[61] Ishida, K. *Calculation of the effect of alloying elements on the M_s temperature in steels.* Journal of Alloys and Compounds, vol. 220, no. 1-2. 1995. pp. 126-131.

[62] Vermeulen, W.G., Morris, P.F., De Weijer, A.P., Van der Zwaag, S. *Prediction of martensite start temperature using artificial neural networks.* Iron and Steelmaking, vol. 23, no. 5. 1996. pp. 433-437.

[63] Wu, W., Hwu, L.Y., Lin, D.Y., Lee, J.L. *The relationship between alloying elements and retained austenite in martensitic stainless steel welds.* Scripta Materialia, vol. 42, no. 11. 2000. pp. 1071-1076.

[64] Capdevila, C., Caballero, F.G., Garcia de Andrés, C. *Analysis of effect of alloying elements on martensite start temperature of steels*. Materials Science and Technology, vol. 19, no. 5. 2003. pp. 581-586.

[65] Sourmail, T., Garcia-Mateo, C. *Critical assessment of models for predicting the M_s temperature of steels.* Computational Material Science, vol. 34, no. 4. 2005. pp. 323-334.

[66] Gorni, A.A. *Steel forming and heat treatment handbook.* www.gorni.eng.br. Accessed 04-04-2014. 2008. pp. 34-47.

[67] Capdevila, C., Caballero, F.G., Garcia de Andrés, C. *Prediction of martensite start temperature by neural network analysis.* Journal De Physique IV, vol. 112. 2003. pp. 217-221.

[68] Charles, J. Mithieux, J.-D., Santacreu, P.-O., Peguet, L. *The ferritic stainless steel family: The appropriate answer to nickel volatility?* Revue De Métallurgie, vol. 106, no. 3. 2009. pp. 124-139.

[69] Schade, C., Schaberl, J., Lawley, A. *Stainless steel AISI grades for PM applications.* International Journal of Powder Metallurgy, vol. 44, no. 3. 2008. pp. 57-67.

[70] Lippold, J.C., Kotecki, D.J. *Welding metallurgy and weldability of stainless steels.* Wiley, Hoboken, NJ. 2005, pp. 19-51.

[71] Balmforth, M.C., Lippold, J.C. *A new ferritic-martensitic stainless steel constitution diagram.* Welding Journal, vol. 79, no. 12. 2000. pp. 330-345.

[72] Lai, J.K.L., Shek, C.H., Lo, K.H. *Stainless steels: An introduction and their recent developments.* Bentham Science Publishers, Sharja. 2012. pp. 72-89.

[73] Pistorius, P.C., Du Toit, M. *Low-nickel austenitic stainless steels: Metallurgical constraints.* Proceedings of the 12th International Ferroalloy Congress (INFACON XII), held in Helsinki, Finland, on 6-9 June 2010. pp. 911-917.

[74] Hull, F.C. *Delta ferrite and martensite formation in stainless steels.* Welding Journal, vol. 52, no. 5. 1973. pp. 193-203.

[75] Kemp, M. Van Bennekom, A., Robinson, F.P.A. *Evaluation of the corrosion and mechanical properties of a range of experimental Cr-Mn stainless steels.* Materials Science and Engineering A, vol. 199, no. 2. 1995. pp. 183-194.

[76] Babakov, A.A. *Substitution of manganese and nitrogen for nickel in stainless steels.* Metal Science and Heat Treatment of Metals, vol. 3, no. 11. 1961. pp. 490-494.

[77] Jackson, E.M.L.E.M., Paton, R. *Influence of manganese on the properties of a vanadium-bearing ferritic stainless steel.* ISIJ International, vol. 35, no. 5. 1995. pp. 557-563.

[78] Lenel, U.R., Knott, B.R. *Structure and properties of corrosion and wear resistant Cr-Mn-N steels.* Metallurgical Transactions A, vol. 18, no. 6. 1987. pp. 847-855.

[79] Speidel, H.J.C., Speidel, M.O. *Nickel and chromium-based high nitrogen alloys.* Materials and Manufacturing Processes, vol. 19, no. 1. 2004. pp. 95-109.

[80] Talha, M, Behera, C.K., Sinha, O.P. *A review on nickel-free nitrogen containing austenitic stainless steels for biomedical applications.* Materials Science and Engineering C, vol. 33, no. 7. 2013. pp. 3563-3575.

[81] Van Rooyen, C. *Microstructural development during laser cladding of low-C martensitic stainless steel.* Welding in the World, vol. 52, no. 3-4. 2008. pp. 22-29.

[82] Kovach, C.W. *High-performance stainless steels.* Nickel Development Institute, Pittsburgh, PA. www.nickelinstitute.org. Accessed 09-05-2013.

[83] Rawers, J.C., Dunning, J.S., Asai, G., Reed, R.P. *Characterization of stainless steels melted under high nitrogen pressure.* Metallurgical Transactions A, vol. 23, no. 7. 1992. pp. 2061-2068.

[84] Simmons, J.W. *Overview: High-nitrogen alloying of stainless steels.* Materials Science and Engineering A, vol. 207, no. 2. 1996. pp. 159-169.

[85] Leda, H. *Nitrogen in martensitic stainless steels.* Journal of Materials Processing Technology, vol. 53, no. 1-2. 1995. pp. 263-272.

[86] Speidel, M.O. *Nitrogen containing austenitic stainless steels.* Materialwissenschaft und Werkstofftechnik, vol. 37, no.10. 2006. pp. 875-880.

[87] Uggowitzer, P.J., Madgowski, R., Speidel, M.O. *High nitrogen steels. Nickel free high nitrogen austenitic steels*. ISIJ International, vol. 36, no. 7. 1996. pp. 901-908.

[88] Gavriljuk, V.G. *Nitrogen in iron and steel.* ISIJ International, vol. 36, no. 7. 1996. pp. 738-745.

[89] Di Schino, A., Kenny, J.M., Mecozzi, M.G., Barteri, M. *Development of high nitrogen, low lickel, 18%Cr austenitic stainless steels.* Journal of Materials Science, vol. 35, no. 19. 2000. pp. 4803-4808.

[90] Di Schino, A., Barteri, M., Kenny, J.M. *Grain size dependence of mechanical, corrosion and tribological properties of high nitrogen stainless steels.* Journal of Materials Science, vol. 38, no. 15. 2003. pp. 3257-3262.

[91] Pozuelo, M., Wittig, J.E., Jiménez, J.A., Frommeyer, G. *Enhanced mechanical properties of a novel high-nitrogen Cr-Mn-Ni-Si austenitic stainless steel via TWIP/TRIP effects*. Metallurgical and Materials Transactions A, vol. 40A, no. 8. 2009. pp. 1826-1834.

[92] Elsener, B., Addari, D., Coray, S., Rossi, A. *Nickel-free manganese bearing stainless steel in alkaline media - Electrochemisty and surface chemistry*. Electrochimica Acta, vol. 56, no. 12. 2011. pp. 4489-4497.

[93] Berezovskaya, V.V., Savrai, R.A., Merkushkin, E.A., Makarov, A.V. *Structure and mechanical and corrosion properties of new high-nitrogen Cr-Mn steels containing molybdenum.* Russian Metallurgy (Metally), vol. 2012, no. 5. 2012. pp. 31-39.

[94] Behjati, P., Kermanpur, A., Najafizadeh, A., Samaei Baghbadorani, H., Karjalainen, L.P., Jung, J.-G., Lee, Y.-K. *Design of a new Ni-free austenitic stainless steel with unique ultrahigh strength-high ductility synergy.* Materials and Design, vol. 63. 2014. pp. 500-507.

[95] Berns, H., Kleff, J., Krauss, G., Foley, R.P. *Microstructure and tensile behavior of nitrogen-alloyed dual-phase stainless steels*. Metallurgical and Materials Transactions A, vol. 27, no. 7. 1996. pp. 1845-1859.

[96] Wang, J., Uggowitzer, P.J., Magdowski, R., Speidel, M.O. *Nickel-free duplex stainless steels.* Scripta Materialia, vol. 40, no. 1. 1998. pp. 123-129.

[97] Calliari, I., Brunelli, K., Zanellato, M., Ramous, E., Bertelli, R. *Microstructural modification during isothermal ageing of a low nickel duplex stainless steel.* Journal of Materials Science, vol. 44, no. 14. 2009. pp. 3764-3769.

[98] Lee, T.-H., Ha, H.-Y., Hwang, B., Kim, S.-J. *Isothermal decomposition of ferrite in a high-nitrogen, nickel-free duplex stainless steel.* Metallurgical and Materials Transactions A, vol. 43, no. 3. 2012. pp. 822-832.

[99] Ma, X.P., Wang, L.J., Qin, B., Liu, C.M., Subramanian, S.V. *Effect of N on microstructure and mechanical properties of 16Cr5Ni1Mo martensitic stainless steel.* Materials and Design, vol. 34. 2012. pp. 74-81.

[100] Ojima, M., Ohnuma, M., Suzuki, J., Ueta, S., Narita, S., Shimizu, T., Tomota, Y. *Origin of the enhanced hardness of a tempered high-nitrogen martensitic steel.* Scripta Materialia, vol. 59, no. 3. 2008. pp. 313-316.

[101] Toro, A., Misiolek, W.Z., Tschiptschin, A.P. *Correlations between microstructure and surface properties in a high nitrogen martensitic stainless steel.* Acta Materialia, vol. 51. 2003. pp. 3363-3374.

[102] Bhadeshia, H.K.D.H., Honeycombe, R. *Steels - Microstructure and properties.* Butterworth Heinemann, Oxford. 2006. pp. 10.

[103] Foct, J. *Future developments and applications of nitrogen-bearing steels and stainless steels*. Sādhanā, vol. 28, no. 3-4. 2003. pp. 731-737.

[104] ASM International. *ASM Handbook Volume 15 - Casting*. ASM International, Materials Park, OH. 2008. pp. 64-67.

[105] Yang, S.-H., Lee, Z.-H. *A method for predicting nitrogen gas pores in nitrogen alloying stainless steels.* Materials Science and Engineering A, vol. 417, no. 1-2. 2006. pp. 307-314.

[106] Mitchell, A., Frederiksson, H. *The electroslag remelting of high-nitrogen steels.* Journal of Materials Science, vol. 39, no. 24. 2004. pp. 7275-7283.

[107] Lo, K.H., Shek, C.H., Lai, J.K.L. *Recent developments in stainless steels.* Materials Science and Engineering R, vol. 65, no. 4-6. 2009. pp. 39-104.

[108] Berns, H. *Manufacture and application of high nitrogen steels.* ISIJ International, vol. 36, no. 7. 1996. pp. 909-914.

[109] Toro, A., Alonso-Falleiros, N., Rodriquez, D., Ambrozio Filho, F. Liberati, J.F., Tschiptschin, A.P. *P/M processing routes for high nitrogen martensitic stainless steels*. Transactions of the Indian Institute of Metals, vol. 55, no. 5. 2002. pp. 481-487.

[110] Turkdogan, E.T. *Fundamentals of steelmaking*. The Institute of Materials, Minerals and Mining, London. 1996. pp. 95-98.

[111] Sudarshan, T.S., Jeandin, M. *Case hardening stainless steels with nitrogen.* Proceedings of the 8th International Conference on Surface Modification Technologies, held in Nice, France, on 26-28 September 1994. pp. 902.

[112] Satir-Kolorz, A.H., Feichtinger, H.K. *On the solubility of nitrogen in liquid iron and steel alloys using elevated pressure.* Zeitschrift für Metallkunde, vol. 82, no. 9. 1991. pp. 689-697.

[113] Hawk, J.A., Simmons, J.W., Raviers, J.C. *Effect of nitrogen alloying on the microstructure and abrasive wear of stainless steels.* Journal of Materials Engineering and Performance, vol. 3, no. 2. 1994. pp. 259-272.

[114] Wada, H., Pehlke, R.D. *Solubility of nitrogen in liquid Fe-Cr-Ni alloys containing manganese and molybdenum*. Metallurgical Transactions B, vol. 8, no. 4. 1977. pp. 675-682.

[115] Bandopadhyay, A., Banerjee, A., Debroy, T. *Nitrogen activity determination in plasmas.* Metallurgical Transactions B, vol. 23, no. 2. 1992. pp. 207-214.

[116] Kuwana, T., Kokawa, H., Saotome, M. *Quantitative prediction of nitrogen absorption by steel during Gas Tungsten Arc Welding*. In Mathematical Modelling of Weld Phenomena, vol. 3 (ed. H. Cerjak), Maney Publishing, London. 1997. pp. 64-81

[117] Palmer, T.A., Mundra, K., Debroy, T. *Nitrogen dissolution in the weld metal - Current status and research opportunities.* In Mathematical Modelling of Weld Phenomena, vol. 3 (ed. H. Cerjak), Maney Publishing, London. 1997. pp. 3-40.

[118] Du Toit, M., Pistorius, P.C. *Nitrogen control during the autogenous arc welding of stainless steel.* Welding in the World, vol. 47, no. 9/10. 2003. pp. 30-43.

[119] Du Toit, M., Pistorius, P.C. *Shielding gas oxygen additions as a means of curbing nitrogen degassing during the autogenous arc welding of nitrogen-alloyed stainless steel.* Welding in the World, vol. 53, no. 1/2. 2009. pp. 38-47.

[120] Poueyo-Verwaerde, A., Fabbro, R., Deshors, G., De Frutos, A.M., Orza, J.M. *Experimental study of laser-induced plasma in welding conditions with continuous CO_2 laser.* Journal of Applied Physics, vol. 74, no. 9. 1993. pp. 5773-5780.

[121] Sato, Y., Dong, W., Kokawa, H., Kuwana, T. *Nitrogen absorption by iron and stainless steels during YAG laser welding*. ISIJ International, vol. 40. 2000. pp. S20-S24.

[122] Dong, W., Kokawa, H., Sato, Y.S., Tsukamoto, S. *Nitrogen absorption by iron and stainless steels during CO_2 laser welding.* Metallurgical and Materials Transactions B, vol. 34, no. 1. 2003. pp. 75-82.

[123] Dong, W., Kokawa, H., Sato, Y.S., Tsukamoto, S., Ogawa, M. *Mechanism governing nitrogen absorption by steel weld metal during laser welding*. Metallurgical and Materials Transactions B, vol. 35, no. 2. 2004. pp. 331-338.

[124] Zhao, L., Tian, Z., Peng, Y. *Porosity and nitrogen content of weld metal in laser welding of high nitrogen austenitic stainless steel.* ISIJ International, vol. 47, no. 12. 2007. pp. 1772-1775.

[125] Huang, C.-C., Tsai, W.-T., Lee, J.-T. *Laser surface alloying of carbon steel with Fe-Cr-Si_3N_4 powders.* Scripta Metallurgica et Materialia, vol. 30, no. 11. 1994. pp. 1461-1466.

[126] Huang, C.-C., Tsai, W.-T., Lee, J.-T. *Electrochemical and surface studies on the passivity of nitrogen and molybdenum containing laser cladded alloys in 3.5 wt% NaCl solution*. Corrosion Science, vol. 37, no.5. 1995. pp. 769-780.

[127] Huang, C.-C., Tsai, W.-T., Lee, J.-T. *Effects of N and Mo on the electrochemical behavior of laser-alloyed stainless steels in a 3.5 wt.% NaCl solution.* Materials Chemistry and Physics, vol. 42, no. 4. 1995. pp. 280-284.

[128] Huang, C.-C., Tsai, W.-T., Lee, J.-T. *Microstructure and electrochemical behavior of laser treated Fe-Cr and Fe-Cr-Si-N surface alloyed layers on carbon steel.* Materials Science and Engineering A, vol. 190, no. 1-2. 1995. pp. 199-205.

[129] Huang, C.-C., Tsai, W.-T., Lee, J.-T. *Microstructure and electrochemical behavior of laser cladded Fe-Cr-Mo-Si-N surface alloys on carbon steel.* Materials Science and Engineering A, vol. 196, no. 1-2. 1995. pp. 243-248.

[130] Huang, C.-C., Tsai, W.-T., Lee, J.-T. *The effect of silicon nitride on the laser surface alloying with Fe-Cr-Si_3N_4 powders.* Scripta Metallurgica et Materialia, vol. 32, no. 9. 1995. pp. 1465-1470.

[131] Huang, C.-C., Tsai, W.-T., Lee, J.-T. *Surface modification of carbon steel with laser treated nitrogen-containing stainless steel layers.* Surface and Coatings Technology, vol. 79, no. 1-3. 1996. pp. 67-70.

[132] Tsai, W.-T., Shieh, C.-H., Lee, J.-T. *Surface modification of ferritic stainless steel by laser alloying.* Thin Solid Films, vol. 247, no. 1. 1994. pp. 79-84.

[133] Lin, S.-A., Lee, J.-T., Tsai, W.-T. *Microstructural aspects and oxidation behavior of laser surface cladded silicon-containing stainless steels.* Scripta Materialia, vol. 38, no. 4. 1998. pp. 559-563.

[134] Sha, C.-K., Tsai, H.-L. *Hardfacing characteristics of S42000 stainless steel powder with added silicon nitride using a CO_2 laser.* Materials Characterization, vol. 52, no. 4-5. 2004. pp. 341-238.

[135] Brytan, Z., Dobrzański, L.A., Pakieła, W. *Sintered stainless steel surface alloyed with Si_3N_4 powder.* Archives of Materials Science and Engineering, vol. 50, no. 1. 2011. pp. 43-55.

[136] Paczkowska, M. *The evaluation of nodular iron surface layer modification by laser alloying with nitrogen and titanium.* Archives of Mechanical Technology and Automation, vol. 33, no. 3. 2013. pp. 33-43.

CHAPTER 3

OBJECTIVES OF THE INVESTIGATION

The literature review in Chapter 2 revealed that nitrogen absorption from a gaseous diatomic nitrogen atmosphere during Nd-YAG laser welding or cladding of stainless steel is unlikely to increase the nitrogen content of the clad layer significantly. The dissolution of Si_3N_4 powder was identified as a possible alternative for increasing the nitrogen concentration of the clad layer. During the course of this project, various alloying techniques were investigated to accommodate higher levels of nitrogen from the dissolution of nitrogen-containing Si_3N_4 powder in modified AISI 410L stainless steel. In addition, parametric investigations were performed to determine if a critical window of cladding parameters exists where porosity and high levels of dilution may be avoided when Si_3N_4 powder is co-fed with AISI 410L powder.

The following objectives were defined in the current investigation:

- To determine the maximum nitrogen content achievable by means of dissolution from diatomic nitrogen-containing shielding and carrier gas atmospheres during laser cladding of modified AISI 410L ferritic/martensitic stainless steels.
- To determine the maximum nitrogen content achievable by means of the addition of varying amounts of Si_3N_4 powder to AISI 410L stainless steel powder during laser cladding.
- To determine and compare the maximum nitrogen contents achievable in various alloy systems based on AISI 410L powder with set additions of Si_3N_4. Varying amounts of manganese and/or nickel powder was added to AISI 410L powder to obtain the alloying systems 410L-Mn-Si-N, 410L-Ni-Si-N and 410L-Ni-Mn-Si-N. In the 410L-Mn-Si-N system manganese powder was added to increase the nitrogen solubility on account of its negative interaction parameter with nitrogen. In the 410L-Ni-Si-N system, the aim was to increase the nitrogen solubility at elevated temperature by enlarging the austenite phase field at high temperatures. Austenite has a higher solubility for nitrogen than ferrite. The aim of the 410L-Ni-Mn-Si-N system was to enhance the nitrogen solubility of the austenite phase field at high temperatures through combined additions of nickel and manganese.
- To determine and compare hardness values obtained as a result of various alloying methods and deposit chemistries.
- To ultimately achieve a laser cladded surface layer with a fully martensitic microstructure, increased nitrogen content and optimised hardness.
- To achieve a minimum nitrogen content of 0.08 wt% in a modified AISI 410L stainless steel.
- To investigate parametric variance with regards to dilution and porosity levels in the 410L-Si-N alloy system and to compare these values with parametric results from the literature.

CHAPTER 4

EXPERIMENTAL PROCEDURE

4.1 INTRODUCTION

During the course of this investigation, a medium-carbon steel substrate with a thickness of 10 mm was surfaced with martensitic stainless steel using a laser powder cladding process and commercially available AISI 410L stainless steel powder. The choice of medium-carbon steel was made on practical grounds considering the intended application of the findings. A 4.4 kW continuous wave Nd:YAG laser with a pneumatic powder feed system and a beam delivery efficiency of approximately 84% was used. The actual laser power delivered to the workpiece was measured with a thermopile sensor which converts the amount of heat absorbed from the laser beam into an electrical signal which is in turn converted to a power level. The relationship between the set laser power and the measured laser power is shown in Figure 4.1.1. To ensure sufficiently low surface roughness to minimise post-clad machining, a bead overlap of 50% was used [1].

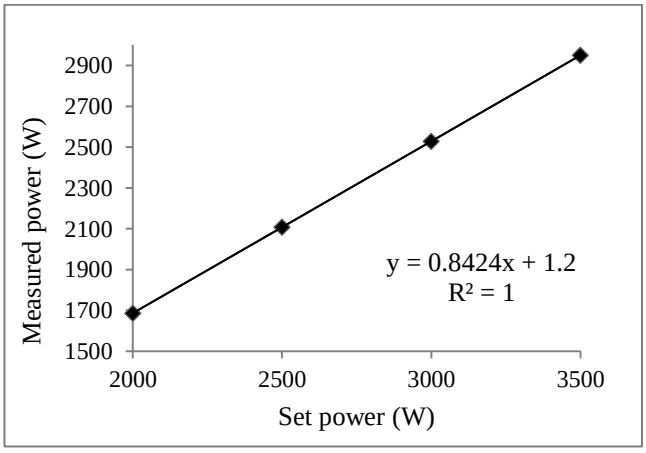

Figure 4.1.1. Measured laser power relative to the set laser power, indicating a beam delivery efficiency of approximately 84%.

To optimise the microstructure and properties of the clad layers, various additions of silicon nitride (Si_3N_4), manganese and nickel powder were made to the AISI 410L stainless steel powder feed, either singly or in combination. All powders used throughout the investigation (AISI 410L, Si_3N_4, Mn and Ni) were crushed and screened to ensure a particle size of between 45 μm and 105 μm, and co-axially fed into the laser beam. The deposit microstructures were evaluated by sectioning representative samples from the clad layers, mounting in resin, polishing to a mirror finish, and etching with Vilella's reagent (1 g picric acid, 5 ml hydrochloric acid and 100 ml ethanol). Hardness measurements throughout the study were obtained using a calibrated Vickers hardness tester with an applied load of 5 kg. Hardness measurements were carried out in the centre of the cross-sectioned cladded layers, and surfaces were prepared to a 3 micron finish during polishing. At least three indentations were made per sample and 95% confidence intervals are reported as error bars on individual hardness curves throughout this study.

4.2 ANALYSES OF METALLURGICAL POWDERS

Table 4.2.1 shows the chemical composition of the commercial AISI 410L powder used during the course of this investigation. The composition of the powder falls well within specified limits for this grade. The manganese and nickel alloying additions used were confirmed to be high purity, single phase metallic powders.

In order to analyse the purity of the Si_3N_4 powder used in this investigation, a representative sample of the crushed and screened 45 µm to 106 µm size fraction was milled and subjected to X-ray diffraction (XRD) analysis. The relative amounts of the phases in the powder (in weight percentage) were estimated by means of the Rietveld method using PANalytical High Score Plus™ software. As shown in Figure 4.2.1, only two phases were identified in the silicon nitride powder, namely nierite (88.2 weight %) and silicon nitride (11.8 weight %). Both these compounds are of the stoichiometric form Si_3N_4 and have hexagonal structures, but are of different spacial groups with different spacial numbers [2]. No analyses were conducted on the remaining metallurgical powders in this study, or on the medium-carbon steel substrate material.

Table 4.2.1. Nominal chemical composition of the AISI 410L powder used in this investigation (weight percentage).

Fe	C	Cr	Mn	Si	P	S
Balance	0.03	12.1	0.61	0.56	< 0.005	< 0.005

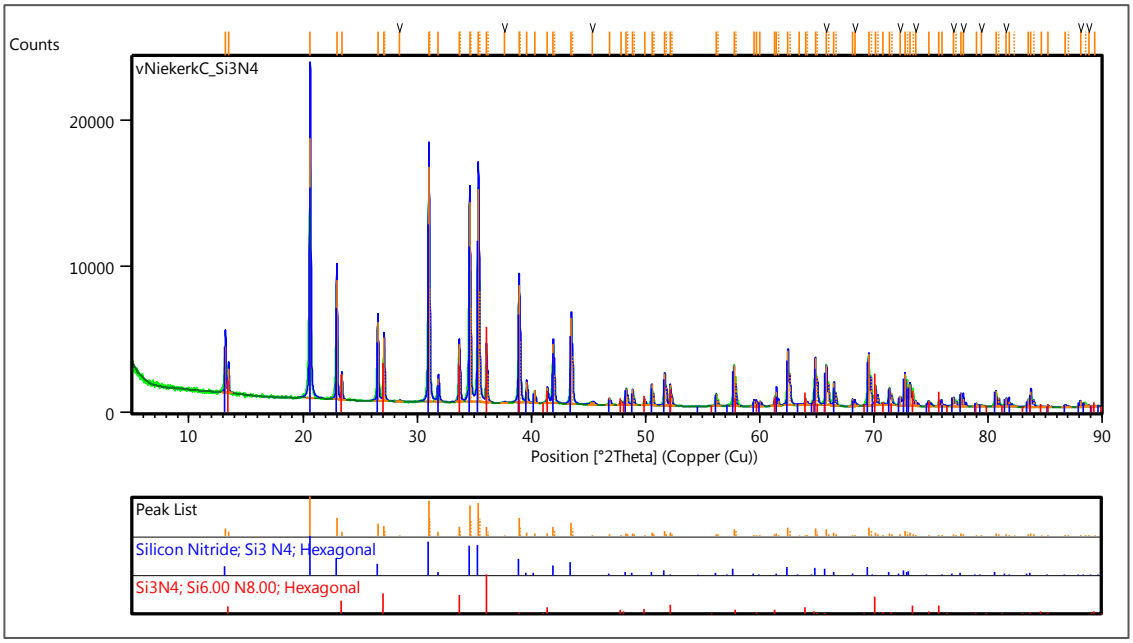

Figure 4.2.1. XRD analysis of the silicon nitride powder used in this investigation, revealing the presence of two different forms of Si_3N_4.

Figure 4.2.3 shows a representative optical photomicrograph of the silicon nitride powder used in this investigation after crushing and screening. The powder was cold mounted in resin, ground and polished. The particles were shown to be amorphous, irregular in shape and with a certain level of porosity as a

consequence of the amorphous structure. Although the porosity is not abundantly clear in the particles shown, it stands to reason that air entrapment could occur with greater ease within the particles during any processing. This could have an effect on the amount of porosity observed in the clad layers when Si_3N_4 is added to the powder feed.

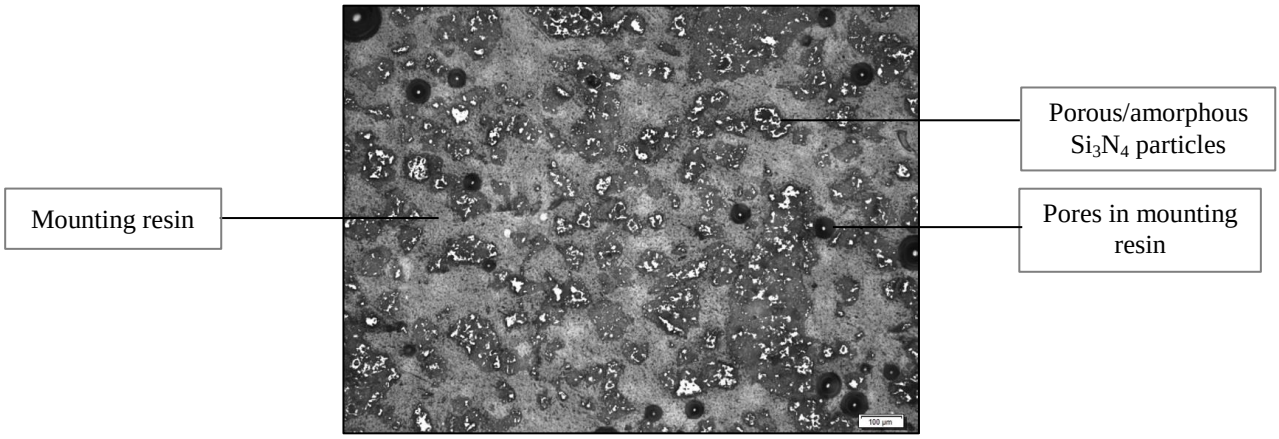

Figure 4.2.3. Optical photomicrograph of the Si_3N_4 powder used in this investigation.

Particle size distributions and morphology analyses were not determined for any metallurgical powders used.

4.3 LASER CLADDING OF AISI 410L STAINLESS STEEL IN DIATOMIC NITROGEN GAS ATMOSPHERES

During the first set of cladding experiments, the maximum nitrogen content that can be achieved through dissolution of nitrogen from nitrogen-containing shielding and carrier gas atmospheres during laser cladding was investigated for AISI 410L stainless steel.

Laser cladding was performed using a Nd-YAG laser and the laser parameters shown in Table 4.3.1. Two single-layer clad deposits were produced. The first sample was produced with pure welding grade argon as shielding and carrier gas, whereas the second specimen was surfaced using pure nitrogen as shielding and carrier gas.

Table 4.3.1. Laser parameters used during laser cladding of AISI 410L in Ar and N_2 atmospheres.

Set laser power (kW)	2.5
Measured laser power (kW)	2.1
Cladding speed (m/min)	1.2
Overlap (%)	50
Powder feed rate (g/min)	30
Focal point distance, f_p (mm)	12
Laser spot size (mm)	4
Shielding gas flow rate (L/min)	15
Carrier gas flow rate (L/min)	3

Following the cladding operation, hardness measurements were performed along the centre of the deposited layers, and the nitrogen contents of the samples were determined using inert gas fusion analysis.

4.4 LASER CLADDING OF AISI 410L-Si-N ALLOYS

4.4.1 Design of the experimental AISI 410L-Si-N clad alloys

In the next set of experiments, the influence of Si_3N_4 additions to AISI 410L powder on the microstructure and properties of the clad layers was evaluated. The alloy design methodology used in this experiment is shown schematically in Figure 4.4.1.

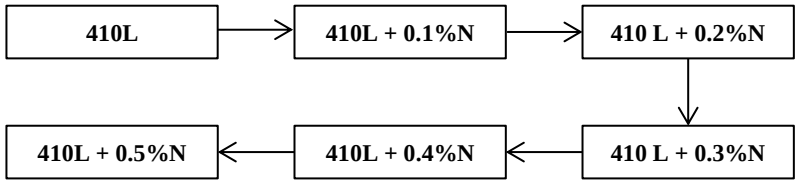

Figure 4.4.1. The design methodology for the alloy system AISI 410L-Si-N prepared by laser cladding and co-feeding of AISI 410L and Si_3N_4 powders (theoretical nitrogen content in wt%).

Six clad samples were produced with varying amounts of Si_3N_4 mixed with AISI 410L powder (Table 4.2.1). The first clad sample was produced as a reference specimen using unmodified AISI 410L powder. In the remainder of the samples, increasing amounts of Si_3N_4 powder were incrementally added to the powder feed. The amount of Si_3N_4 powder in the feed was adjusted to deliver theoretical maximum nitrogen contents of between 0.1 wt% and 0.5 wt% in increments of 0.1 wt% nitrogen. An example of such a calculation is shown in Appendix A1. Calculation of these maximum theoretical nitrogen contents was based on the assumption that Si_3N_4 completely dissociates during cladding and that dilution with the substrate is negligible. In reality the deposit nitrogen contents will be somewhat lower than the calculated maximum values.

Single-layer and multi-layer clad deposits were produced using the parameters in Table 4.4.1. Single-layer deposits were produced at a total powder feed rate of 30 g/min and a measured laser power of 2.9 kW, whereas three-layer deposits were produced at a powder feed rate of 15 g/min and a laser power of 2.5 kW. The residual oxygen content in the clad layers under argon shielding was approximately 13 parts per million.

4.4.2 Laser parameter optimisation in the AISI 410L-Si-N system

4.4.2.1 Parameter range selection

After the initial experiments studying nitrogen alloying by means of Si_3N_4 powder additions, the laser cladding parameters were optimised. Parameter optimisation entailed systematically varying the laser power, cladding speed and powder feed rate to find an optimum combination of parameters with regards to observed dilution levels and clad geometry in single-track layers, and volume percentage porosity in multi-track layers. All other laser parameters, such as focal point distance, laser spot size, and shielding and carrier gas flow rates, were kept constant. Nitrogen was used as shielding and carrier gas. A simplified factorial

experimental design, based on the methodology proposed by Montgomery [3], was used in the design of the experimental matrix.

Table 4.4.1. Laser parameters used to produce clad deposits of AISI 410L alloyed with Si_3N_4.

Parameter	Single-layer deposits	Three-layer deposits
Set laser power (kW)	3.5	3.0
Cladding speed (m/min)	1.2	1.2
Overlap (%)	50	50
Powder feed rate (g/min)	30	15
Focal point distance, f_p (mm)	12	12
Laser spot size (mm)	4	4
Shielding gas flow rate (L/min)	15	15
Carrier gas flow rate (L/min)	3	3
Shielding and carrier gas used	Ar	Ar
Number of layers	1	3

As shown in Figure 4.4.2, combinations of four laser power settings and three cladding speed settings were investigated (enclosed by the box in this figure). The set laser power was varied from 2 kW to 3.5 kW (corresponding to measured power levels of 1.69 kW to 2.95 kW) in 0.5 kW increments and the cladding speed was varied from 1.0 m/min to 1.4 m/min in 0.2 m/min increments. Optimisation experiments were carried out using all possible combinations of these parameters within the experimental matrix. In the context of this investigation a "+" sign in Figure 4.4.2 denotes a high value and a "-" sign denotes a low value. The minimum and maximum settings were selected on the basis of earlier optimisation work carried out at the NLC. Combinations of low laser power and low cladding speed were shown to result in intermittent clad deposits, whereas high power and cladding speed settings resulted in excessive heating and dilution. The experimental matrix shown in Figure 4.4.2 was repeated for powder feed rates of 25 g/min and 30 g/min. A constant ratio of AISI 410L to Si_3N_4 powder was maintained in the powder feed (resulting in a theoretical nitrogen content of 0.4 wt%).

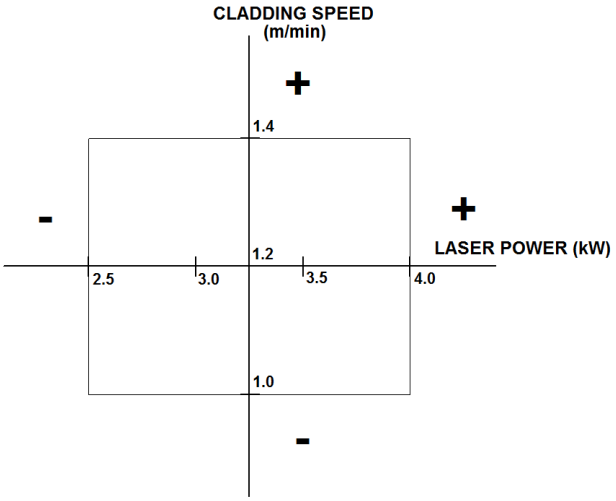

Figure 4.4.2. Design methodology for single and multi-track laser parameter optimisation.

The number of laser parameter combinations tested during the course of this investigation can be determined from equation (4.4.1):

$$N = \sum_{n=2}^{n_i} P \times S \qquad \ldots(4.4.1)$$

where: *N* is the number of entries in the experimental matrix,
n is the number of feed rates evaluated,
P is the number of power settings, and
S is the number of different cladding speed settings.

For values of n=2, P=4 and S=3, the total number of parameter combinations in the matrix are 24, as shown below:

$$N = \sum_{n=2}^{n_i} 4 \times 3 = (4 \times 3) + (4 \times 3) = 12 + 12 = 24$$

A more detailed layout of the experimental matrix used is given in Appendix A2 of this study. Table 4.4.2 summarises all laser parameters examined during this stage of the investigation. The residual oxygen level under nitrogen shielding was less than 20 parts per million.

Table 4.4.2. Parameters used in the laser parameter optimisation matrix for both single- and multi-track experiments.

Set laser power (kW)	2.0 - 3.5
Measured laser power (kW)	1.69 - 2.95
Cladding speed (m/min)	1.0 - 1.4
Powder feed rate (g/min)	25 - 30
Overlap (%)	50
Focal point distance, f_p (mm)	12
Laser spot size (mm)	4
Shielding gas flow rate (L/min)	15
Carrier gas flow rate (L/min)	3
Shielding and carrier gas used	N_2
Measured O_2 levels (ppm)	< 20

4.4.2.2 Single-track parameter optimisation

Single-track deposits were produced using the experimental parameter matrix described in section 4.4.2.1 and the clad geometry was analysed in terms of clad height, width and depth of penetration (as shown schematically in Figure 2.1.6). Dilution levels were calculated by means of equation (4.4.2) [4]. Repeatability was ensured by randomly repeating three different parameter combinations three times, as illustrated in Appendix A3.

$$\text{Dilution} = \frac{b}{h+b} \qquad \ldots (4.4.2)$$

Representative samples were sectioned from each track, mounted in resin and polished to a mirror finish. The prepared samples were etched with a 3% Nital solution (consisting of 3 ml nitric acid and 97 ml ethanol) to ensure high contrast between the etched medium-carbon steel substrate and the unetched stainless steel surface layer.

4.4.2.3 Multi-track parameter optimisation

The influence of the laser parameters on the observable volume percentage porosity in multi-track deposits was investigated using the experimental matrix described in Table 4.4.2. This parameter matrix was used to deposit nine tracks per sample with a 50% overlap between tracks. The specimens were sectioned in the transverse direction at six random locations, as shown schematically in Figure 4.4.3.

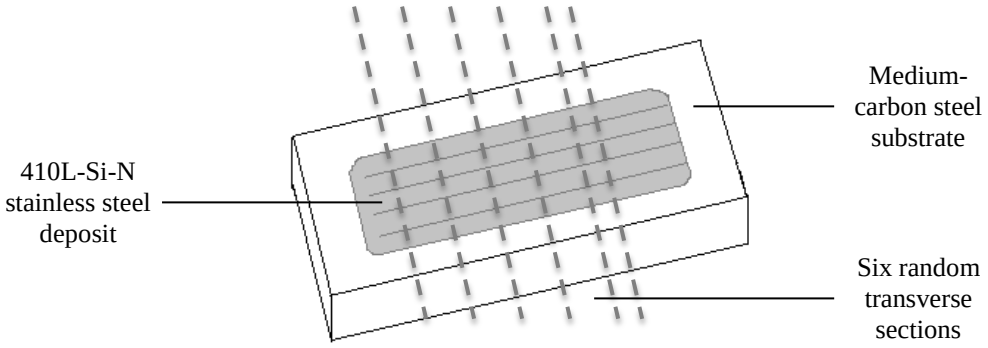

Figure 4.4.3. Schematic representation of six random transverse sections through the laser deposited surfaces.

The samples were mounted in cross-section and polished to a mirror finish. To ensure that porosity would be clearly visible in the clad deposits, the samples were not etched. Photomicrographs were taken in random locations at magnifications of either 100X or 200X, depending on the layer's thickness. The magnification was selected to be as high as possible to prevent substrate material from being included in the images.

The public domain image processing software package, ImageJ™, was subsequently used to determine the volume percentage porosity in the prepared samples. Figure 4.4.4(a) shows a typical photomicrograph of a polished section loaded into the software. The image was transformed into a binary file, as shown in Figure 4.4.4(b), followed by pixel analysis to determine the area occupied by black pixels (representing porosity). For the example shown in Figure 4.4.4, 19.5% porosity was measured. Area percentage porosity was assumed to be equal to volume percentage porosity [5]. Depending on statistical variance, this process was repeated for multiple photographs across each sample's prepared surface areas (6 cross sectional areas per sample) through a range of 25-50 photographs per sample, and an average percentage porosity, standard deviation, and 95% confidence interval were determined.

The observable volume percentage porosity for cladded layers was determined in this way for the purposes of multi-track parameter optimisation alone. This procedure was not repeated for any experimental alloys produced as described in sections 4.4.1 and 4.7.1 and no other attempt was made to quantify the observed porosity for the alloys produced during this study.

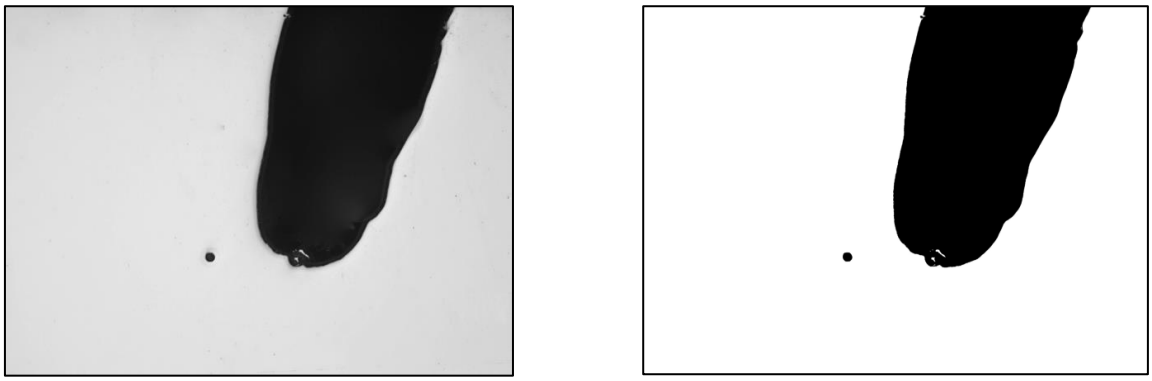

(a) (b)

Figure 4.4.4. Example of the determination of volume percentage porosity using image processing software: (a) micrograph loaded into the software; and (b) binary image of the photograph to be analysed.

4.5 DESIGN OF THEORETICAL AISI 410L-Mn, AISI 410L-Ni and AISI 410L-Mn-Ni CLAD ALLOYS

As described in more detail in Chapter 5, neither the use of nitrogen as shielding and carrier gas, nor the addition of Si_3N_4 powder to AISI 410L to form AISI 410L-Si-N alloys resulted in sufficient nitrogen pick-up in the surface layers during laser cladding. Alternative alloy systems, based on AISI 410L (Table 4.2.1), were therefore considered in an attempt to increase the deposit nitrogen content. Three different theoretical alloy systems were investigated. In the first alloy system, between 1% and 3% (by weight) manganese powder was added to AISI 410L powder to produce three experimental AISI 410L-Mn alloys. This alloy system was designed to take advantage of the beneficial influence of manganese on nitrogen solubility. In the second set of alloys, up to 5.5% nickel was added to the stainless steel powder to make up four theoretical AISI 410L-Ni alloys, with the aim of increasing the amount of high temperature austenite formed in the deposit. In the last set of alloys, up to 3% manganese was added to alloys containing 2% nickel, resulting in four AISI 410L-Mn-Ni theoretical alloys.

Dilution levels during cladding were not taken into consideration in any of the following calculations. Determination of the theoretical compositions of alloys was established on a comparative basis between the different alloys and actual chemical compositions would differ from the theorised compositions depending on the level of dilution experienced during laser cladding. During execution of the experimental procedure, laser parameters were selected to ensure full melting of metallurgical powders at minimum dilution levels. The approach to alloy design was purely theoretical and ignores the effect of dilution. This effect would therefore contribute to variations in actual nitrogen solubility levels in these alloys from that predicted. Results to this regard are given in Section 5.5 of this study.

The theoretical alloys were designed on the basis of the predicted phase composition of the final room temperature microstructure prior to the addition of nitrogen. This method entailed strict control over the amounts of δ-ferrite, martensite and retained austenite in the room temperature microstructures. The

modified Schaeffler diagram for laser welding, developed by David *et al.* [6], was used to determine the influence of manganese and nickel additions to AISI 410L on the predicted phase composition, while the M_s temperatures of the alloys were calculated by means of the equation developed by Capdevila *et al.* [7] (equation (4.5.1)). This approach was used to ensure fully martensitic microstructures, even at high nitrogen levels.

$$M_s\ (K) = 767.7 - 305[C] - 30.6[Mn] - 14.5[Si] - 8.9[(Cr] - 16.6[(Ni] + 2.4[Mo] + 5.3[V] + 8.58[Co] + 40.4[Al] + 7.4\ [W] - 11.3[Cu] + 510.4[Nb] \quad \ldots (4.5.1)$$

Equations (4.5.2) and (4.5.3) show the nickel-equivalent and chromium-equivalent equations in accordance with the modified Schaeffler diagram shown in Figure 4.5.1.

$$\text{Ni-equivalent} = [Ni] + 30[C] + 0.5[Mn] \quad \ldots (4.5.2)$$

$$\text{Cr-equivalent} = [Cr] + [Mo] + 1.5[Si] + 0.5[Nb] \quad \ldots (4.5.3)$$

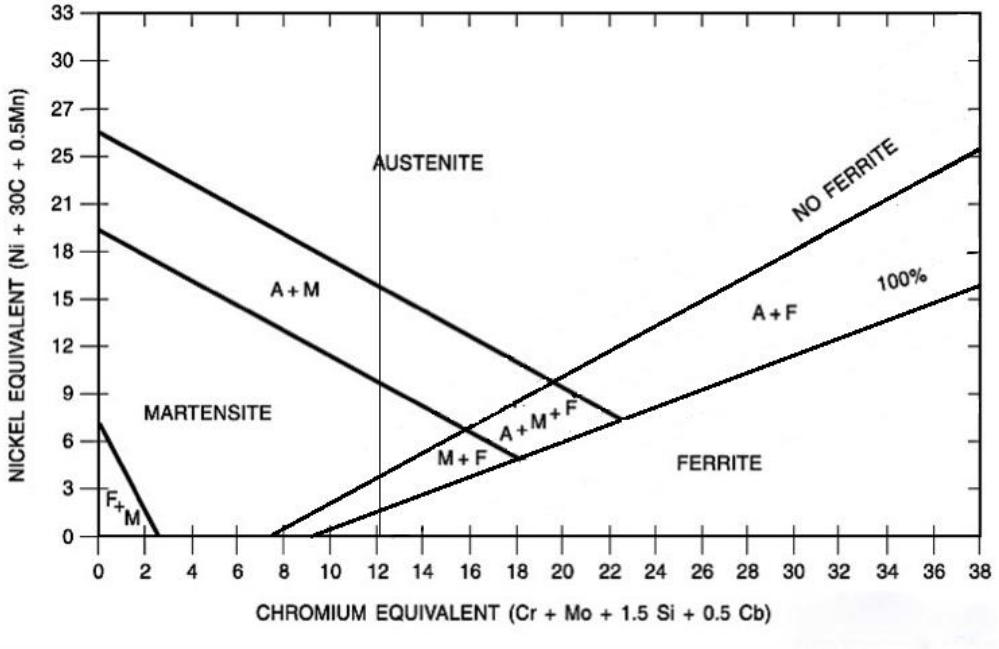

Figure 4.5.1. Modified Schaeffler diagram for laser welding processes. Adapted from the AWS Welding Handbook [8] from David *et al.* [6].

The Cr-equivalent of the AISI 410L powder used in this investigation (with composition as given by Table 4.2.1) is indicated by the vertical line at 12.1 in Figure 4.5.1. According to equations (4.5.2) and (4.5.3), manganese and nickel additions affect the Ni-equivalent of the clad deposit. Although large additions of Mn and/or Ni to AISI 410L powder dilute the ferrite-forming elements (Cr, Mo, Si and Nb) in the deposit to some extent, the Cr-equivalents of the theoretical alloys should not be reduced significantly. It is evident from Figure 4.5.1 that, at a Cr-equivalent of 12.1, fully martensitic microstructures are predicted for Ni-equivalents of between about 4 and 10. Since nitrogen is a strong austenite-former, the optimum nickel equivalents achieved through additions of manganese and/or nickel to AISI 410L should be close to the

lower bounds of this range, either just above or just below the minimum value of 4, to accommodate nitrogen.

The design methodology followed for the addition of manganese and nickel to AISI 410L is shown schematically in Figure 4.5.2. In the first set of theoretical alloys, (a) in Figure 4.5.2, manganese powder was added to AISI 410L in increments of 1 wt% up to a theoretical maximum of 3 wt% (assuming negligible dilution with the substrate). In the second set of alloys, (c) in Figure 4.5.2, up to 5.5 wt% nickel was added to AISI 410L powder. In the third set of alloys, (b) in Figure 4.5.2, combinations of manganese and nickel were added to AISI 410L powder by keeping the nickel content fixed at 2 wt% and increasing the manganese content up to a maximum theoretical content of 3 wt%.

The Cr- and Ni- equivalents of AISI 410L and the different theoretical alloys (without considering the effect of nitrogen) are given in Table 4.5.1. This table also contains the calculated M_s and assumed M_f temperatures of each alloy. The M_f temperature was assumed to be on average about 150°C below the M_s temperature [9]. The Cr-equivalents and Ni-equivalents of each alloy system are shown on the modified Schaeffler diagram in Figure 4.5.3.

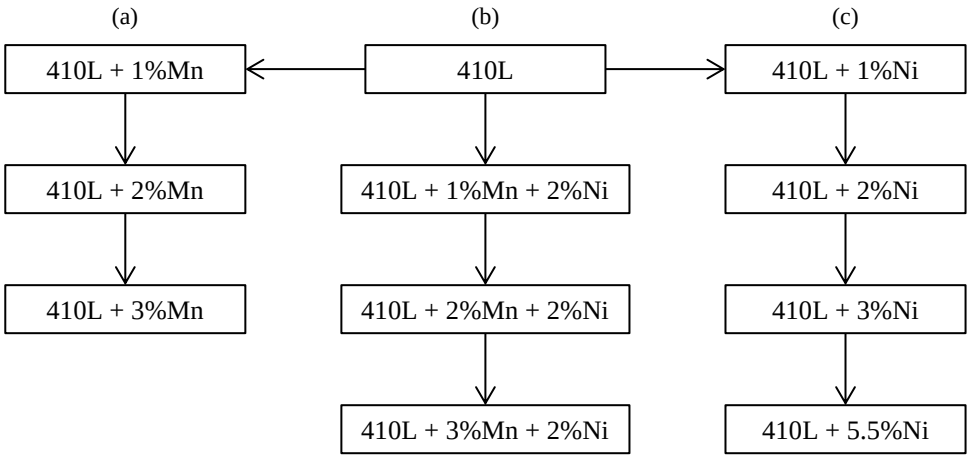

Figure 4.5.2. Alloy design methodology for the theoretical alloy systems: (a) AISI 410L-Mn; (b) AISI 410L-Ni-Mn; and (c) AISI 410L-Ni.

To guarantee adequate hardness in the surface layers, it is important to avoid excessive retained austenite in the room temperature clad microstructures. In the alloys under investigation, retained austenite is expected when the Ni-equivalent exceeds a value of about 10 (according to Figure 4.5.1), or when the calculated M_f temperatures are below room temperature. Although Table 4.5.1 suggests that none of the theoretical alloys have M_f temperatures below room temperature, the effect of nitrogen was not considered in these calculations. Since nitrogen alloying from Si_4N_3 powder is expected to increase the Ni-equivalent and reduce the M_s and M_f temperatures, the risk of retained austenite increases with nitrogen addition and care should be taken to ensure fully martensitic structures. The alloy consisting of AISI 410L powder alloyed with 5.5% nickel has the highest Ni-equivalent of the alloys investigated, and although a fully martensitic microstructure is predicted (Figure 4.5.3), this alloy can accommodate the least amount of nitrogen before

retained austenite is expected. AISI 410L alloyed with 3% Mn has the lowest Ni-equivalent of the theoretical alloys and can therefore accommodate the highest amount of nitrogen. It should be noted that by increasing the Ni-equivalent, nitrogen alloying also reduces the risk of δ-ferrite formation.

Table 4.5.1. The Cr- and Ni-equivalents for AISI 410L and the theoretical alloy systems AISI 410L-Mn, AISI 410L-Ni, and AISI 410L-Ni-Mn, and the M_s and M_f temperatures calculated according to the equation by Capdevila *et al.* [7].

Alloy system	Cr-equivalent	Ni-equivalent	M_s (K)	M_s (°C)	M_f (°C)
AISI 410L	12.9	1.2	624	351	201
410L-Mn					
410L + 1% Mn	12.9	1.7	593	320	170
410L + 2% Mn	12.9	2.2	563	290	140
410L + 3% Mn	12.9	2.7	532	259	109
410L-Ni					
410L + 1% Ni	12.9	2.2	607	334	184
410L + 2% Ni	12.9	3.2	591	318	168
410L + 3% Ni	12.9	4.2	574	301	151
410L + 5.5% Ni	12.9	6.7	533	260	110
410L-Ni-Mn					
410L + 2% Ni + 1% Mn	12.9	3.7	560	287	137
410L + 2% Ni + 2% Mn	12.9	4.2	530	257	107
410L + 2% Ni + 3% Mn	12.9	4.7	499	226	76

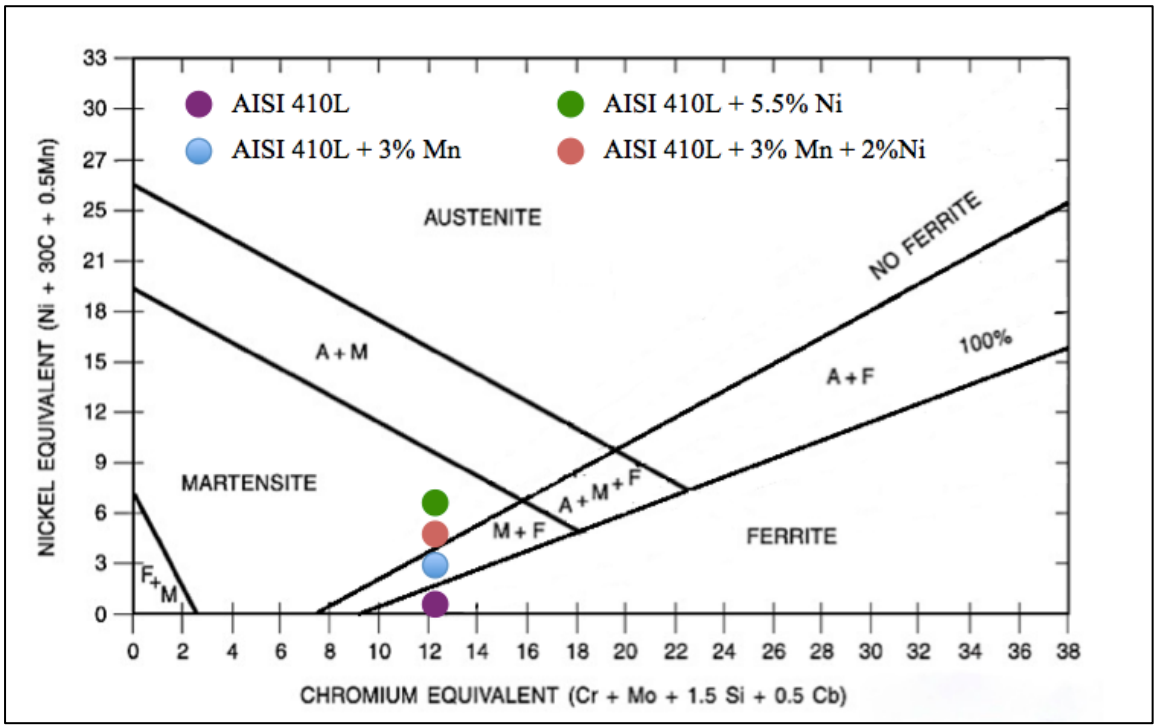

Figure 4.5.3. Modified Schaeffler diagram for laser welding processes. Adapted from the AWS Welding Handbook [8] according to David *et al.* [6], with the position of the most highly alloyed alloy in each theoretical alloy system shown.

Figures 4.5.4 (a), (b) and (c) represent the calculated M_s temperatures for the AISI 410L-Mn, AISI 410L-Ni and AISI 410L-Ni-Mn alloy systems, respectively, as a function of Ni-equivalent. These figures suggest that the M_s temperatures decrease as the theoretical Mn and/or Ni contents increase (as expected from equation (4.5.1)). The lowest M_s temperatures are obtained in the most highly alloyed steels in each alloy system, i.e. the AISI 410L-5.5%Ni, AISI 410L-3%Mn and AISI 410L-3%Mn-2%Ni alloys. These alloys can therefore accommodate less nitrogen.

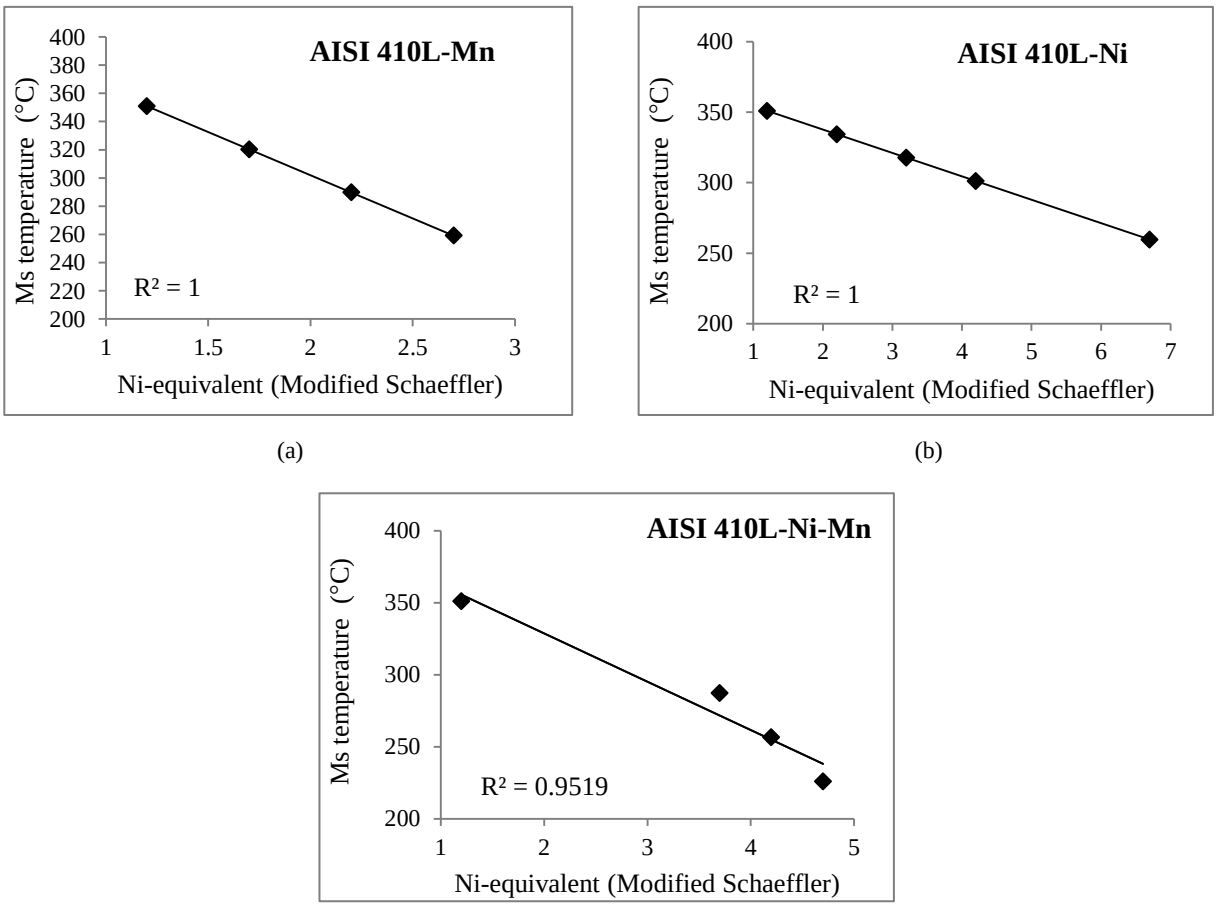

Figure 4.5.4. M_s temperatures of the theoretical alloys for the: (a) AISI 410L-Mn; (b) AISI 410L-Ni; and (c) AISI 410L-Ni-Mn alloy systems, calculated according to the equation by Capdevila *et al.* [7].

In order to accommodate the effect of nitrogen on the Ni-equivalent and on the M_s and M_f temperatures, a maximum nitrogen content of 0.2 wt% was selected to serve as a safe-design criterion. As shown in Table 4.5.2, the Mn and Ni levels of the experimental alloys were selected to ensure that the calculated M_s and M_f temperatures are generally above room temperature at this nitrogen content (based on the assumption that the influence of C and N on the M_s temperature is similar or equal [10]).

4.6 THERMODYNAMIC PREDICTION OF ALLOYING ELEMENT INTERACTIONS

The influence of manganese and nickel additions on the solubility of nitrogen in AISI 410L stainless steel was estimated using Thermocalc™ thermodynamic prediction software (with database TCFE7). Although the information obtained from Thermocalc™ is only valid under equilibrium conditions, it provides valuable

information on the interaction between alloying elements and was merely used as a tool to estimate the changes in nitrogen solubility in different alloy systems as a consequence of the changes in alloy composition. During laser cladding non-thermodynamic conditions prevail and therefore any predictions made by Thermocalc™ should be regarded as purely indicative.

Table 4.5.2. Calculated M_f temperatures for the theoretical alloys with an optimistic 0.2 wt% N as the safe-design criterion.

Alloy system	**Calculated M_f temperature (°C) at 0.2 wt% N**
AISI 410L	140
410L-Mn	
410L + 1% Mn	109
410L + 2% Mn	79
410L + 3% Mn	48
410L-Ni	
410L + 1% Ni	123
410L + 2% Ni	107
410L + 3% Ni	90
410L + 5.5% Ni	49
410L-Ni-Mn	
410L + 2% Ni + 1% Mn	76
410L + 2% Ni + 2% Mn	46
410L + 2% Ni + 3% Mn	15

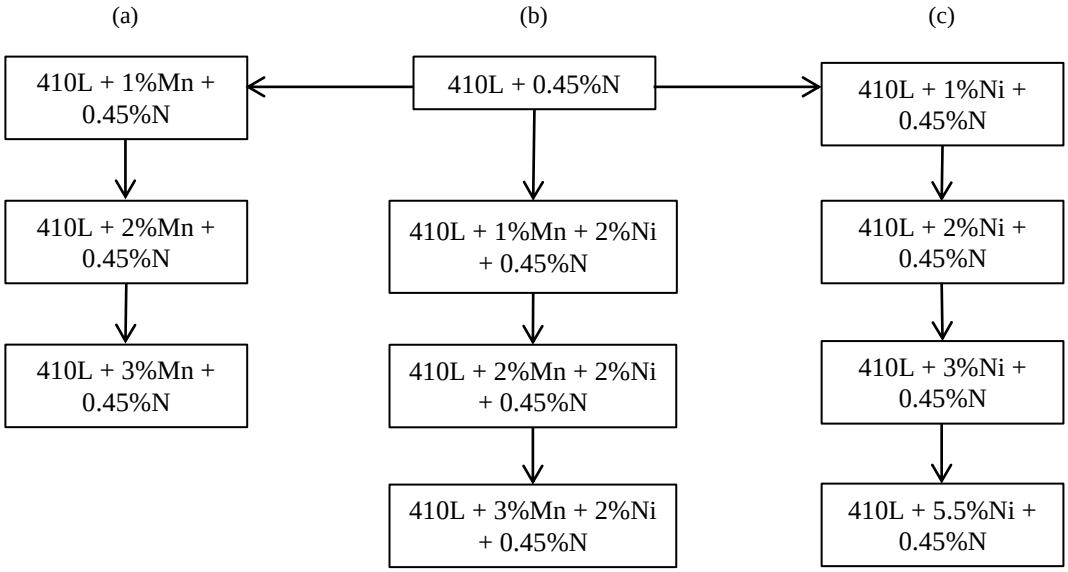

Figure 4.6.1. Alloy design methodology for the: (a) AISI 410L-Mn-Si-N; (b) AISI 410L-Ni-Mn-Si-N; and (c) AISI 410L-Ni-Si-N alloy systems, modelled using Thermocalc™.

The three theoretical alloy systems described in the previous section were modelled in accordance with the alloy design methodology illustrated in Figure 4.6.1. These theoretical alloy systems were designed for a specified Si_3N_4 addition, yielding a maximum calculated nitrogen content of 0.45% on dissociation. Thermocalc™ rejects excess nitrogen not dissolved in ferrite or high-temperature austenite and not chemically bonded in a nitride phase to the gaseous phase. As in the previous section, manganese was added to the nominal chemical composition given in Table 4.2.1at contents ranging from 1 wt% to 3 wt% in the theoretical AISI 410L-Mn-Si-N system (system (a) in Figure 4.6.1), while in the AISI 410L-Ni-Si-N system (system (c) in Figure 4.6.1), nickel was added from 1 wt% to 5.5 wt%. In the AISI 410L-Mn-Ni-Si-N system (system (b) in Figure 4.6.1), manganese was added from 1 wt% to 3 wt% at fixed nickel and nitrogen contents.

4.7 LASER CLADDING OF AISI 410L-Mn-Si-N, AISI 410L-Ni-Si-N AND AISI 410L-Ni-Mn-Si-N ALLOYS

4.7.1 Design of theoretical AISI 410L-Mn-Si-N, AISI 410L-Ni-Si-N and AISI 410L-Mn-Ni-Si-N clad alloys

Once the theoretical design of the clad alloys systems had been completed, laser clad layers were deposited using the desired powder mixtures. Two sets of experiments were conducted. In the first set of experiments, the methodology described in Figure 4.5.2 was followed by adding manganese and/or nickel to the AISI 410L stainless steel powder. Si_3N_4 powder was not added. In the second set of experiments, the methodology described in Figure 4.6.1 was followed with the addition of Si_3N_4, manganese and nickel to the powder feed. Unfortunately the pneumatic powder feeder used during cladding could not deliver the exact manganese and nickel powder feed rates required to produce the desired theoretical alloys. For this reason the manganese and nickel contents had to be adjusted slightly in accordance with the feed rate capabilities of the powder feeders during cladding.

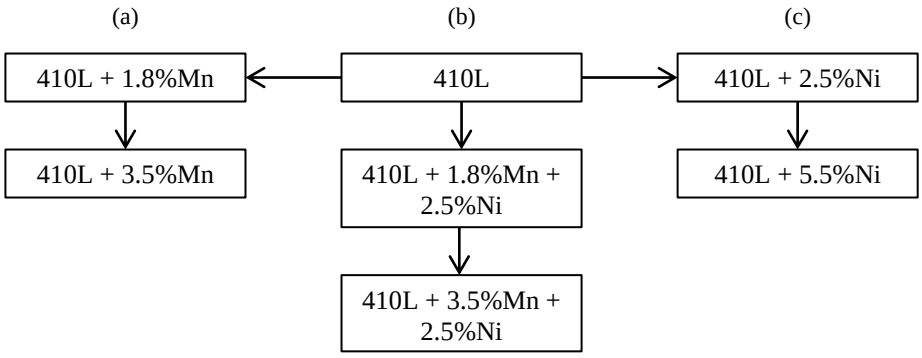

Figure 4.7.1. Alloy design methodology for the: (a) AISI 410L-Mn; (b) AISI 410L-Ni-Mn; and (c) AISI 410L-Ni alloy systems, prepared using laser powder cladding at two different powder feed rates.

Figure 4.7.1 shows the alloy design methodology used in preparing the first set of experimental alloys, deposited without the addition of any Si_3N_4 powder during cladding. The powder feed used to prepare these

samples consisted of AISI 410L powder, co-fed with manganese powder ((a) in Figure 4.7.1), nickel powder ((c) in Figure 4.7.1), or combinations of manganese and nickel (system (b) in Figure 4.7.1).

The alloy design matrix shown in Figure 4.7.1 was then repeated with a Si_3N_4 addition to the powder feed at a feed rate selected to yield a consistent calculated nitrogen content of 0.45% on dissociation, as illustrated in Figure 4.7.2.

4.7.2 Parameter selection

For the cladding experiments described above, the laser cladding parameters listed in Table 4.7.1 were used.

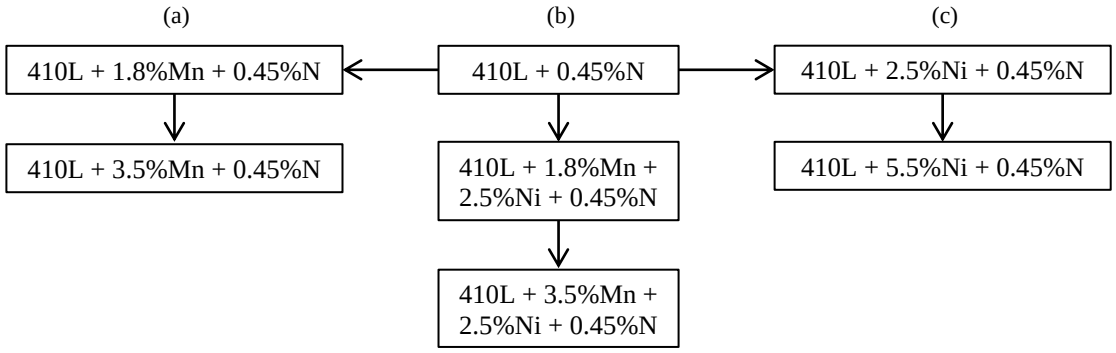

Figure 4.7.2. Alloy design methodology for the: (a) AISI 410L-Mn-Si-N; (b) AISI 410L-Ni-Mn-Si-N; and (c) AISI 410L-Ni-Si-N alloy systems, prepared using laser powder cladding at two different powder feed rates.

Table 4.7.1. Laser parameters used to produce single- and double-layer deposits.

Parameter	2-layer deposit	Single layer deposit
Set laser power (kW)	3.0	3.5
Cladding speed (m/min)	1.2	1.2
Powder feed rate (g/min)	15	30
Overlap (%)	50	50
Focal point distance, f_p (mm)	12	12
Laser spot size (mm)	4	4
Shielding gas flow rate (L/min)	15	15
Carrier gas flow rate (L/min)	2.5	2.5
Shielding and carrier gas	N_2	N_2
Measured O_2 levels (ppm)	12	12
Number of layers	2	1

Nitrogen was used as carrier and shielding gas at flow rates of 2.5 L/min (for each powder) and 15 L/min, respectively. The residual oxygen level was 12 parts per million. To investigate the effect of successive layering of deposits on the hardness and nitrogen contents, the cladding matrices shown in Figures 4.7.1 and 4.7.2 were each repeated at two different feed rates. A total powder feed rate of 15 g/min was used to produce two-layer deposits, and a total powder feed rate of 30 g/min was used to produce single-layer

deposits. The measured laser power for samples produced at a total powder feed rate of 15 g/min was 2.52 kW and for samples produced at a total powder feed rate of 30 g/min was 2.94 kW.

4.8 SUMMARY

The experimental procedure described in this chapter aims to determine the maximum nitrogen content attainable through *in-situ* alloying of AISI 410L stainless steel with nitrogen during laser cladding. To achieve this aim, nitrogen alloying by means of nitrogen-rich shielding and carrier gas, as well as nitrogen absorption from Si_4N_3 additions to the powder feed was investigated for standard AISI 410L and for AISI 410L powder modified with manganese and/or nickel additions. The results obtained from these experiments are discussed in more detail in the next chapter.

4.9 REFERENCES

[1] Vilar, R. *Laser cladding*. Journal of Laser Applications, vol. 11, no. 2. 1999. pp. 64-79.

[2] Lee, M.R., Russell, S.S., Arden, J.W., Pillinger, C.T. *Nierite (Si_3N_4), a new mineral from ordinary and enstatite chondrites*. Meteoritics and Planetary Science, vol. 30, no. 4. 1995. pp. 387-398.

[3] Montgomery, D.C. *Design and analysis of experiments*. John Wiley & Sons Inc., Hoboken, NJ. 2001.

[4] Toyserkani, E., Khajepour, A., Corbin, S.F. *Laser cladding*. CRC Press, Boca Raton, FL. 2005.

[5] Underwood, E.E. *Quantitative stereology*. Addison-Wesley Publishing Company Inc., Boston, MA. 1970. pp. 20.

[6] David, S.A., Vitek, J.M., Hebble, T.L. *Effect of rapid solidification on stainless steel weld metal microstructures and its implications on the Schaeffler diagram.* Welding Journal, vol. 66, no. 10. 1987. pp. 289-300.

[7] Capdevila, C., Caballero, F.G., Garcia de Andrés, C. *Prediction of martensite start temperature by neural network analysis.* Journal De Physique IV, vol. 112. 2003. pp. 217-221.

[8] American Welding Society. *Welding Handbook, Volume 4 - Materials and Applications, Part 1*. American Welding Society, Miami, FL. 2011. pp. 285.

[9] Bhadeshia, H.K.D.H., Honeycombe, R. *Steels - Microstructure and properties.* Butterworth Heinemann, Oxford. 2006. pp. 10.

[10] Porter, D.A., Easterling, K.E. *Phase transformations in metals and alloys.* Chapman & Hall, London. 1992.

CHAPTER 5

RESULTS AND DISCUSSION

This chapter presents the results obtained during this investigation and assesses the feasibility of the *in-situ* nitrogen alloying methods examined. To facilitate the discussion, the results are described in the chronological order in which the experiments were performed.

5.1 LASER CLADDING OF AISI 410L STAINLESS STEEL IN DIATOMIC NITROGEN GAS ATMOSPHERES

As described in Chapter 2, published literature suggests that achieving high nitrogen contents, or even equilibrium nitrogen solubility levels, by means of nitrogen absorption from nitrogen-rich shielding or carrier gas atmospheres is unlikely during Nd:YAG laser cladding. The short thermal cycle does not allow enough time for nitrogen pick-up from the diatomic nitrogen atmosphere, and plasma formation is suppressed as a result of insufficient laser absorption by the gaseous metal plume above the weld pool. Under these conditions, enough monatomic nitrogen does not form in the atmosphere to enhance solubility. This section aimed to test these conclusions and to confirm that nitrogen absorption from the atmosphere is unsatisfactory during Nd-YAG laser cladding. To this end, single-layer deposits of AISI 410L stainless steel were made on carbon steel substrate using the cladding parameters described in section 4.3, with either argon or nitrogen as shielding and carrier gas.

Figure 5.1.1 shows the results of hardness measurements after cladding as a function of the maximum nitrogen content (wt %) attained after cladding in a fully diatomic nitrogen (N_2) gas atmosphere. The hardness indentations were made on the top surfaces of the layers at the clad centreline in all cases. It is evident that the deposit hardness increased slightly with a change in cladding atmosphere from pure argon to pure nitrogen, suggesting that some interstitial solid solution strengthening had occurred as a result of nitrogen absorption from the shielding and carrier gas atmospheres. The observed increase in hardness is, however, marginal. Inert gas fusion analysis of the deposit nitrogen contents confirmed a slight increase in nitrogen content from 0.03 wt% (deposited in an argon atmosphere) to 0.04 wt% (in a nitrogen atmosphere). The final deposit nitrogen content is well below the minimum requirement of 0.08 wt% (as stated in Chapter 3).

These results confirm that nitrogen absorption from a diatomic nitrogen atmosphere during Nd-YAG laser cladding is limited and suggests that alternative methods of *in-situ* nitrogen alloying should be investigated. As discussed in section 2.3.6, Si_3N_4 powder added to the stainless steel powder feed may serve as a viable source of nitrogen during laser cladding. The next section discusses the results obtained from *in-situ* alloying of stainless steel clad deposits with nitrogen by co-feeding AISI 410L stainless steel powder and Si_3N_4 powder during Nd-YAG laser cladding.

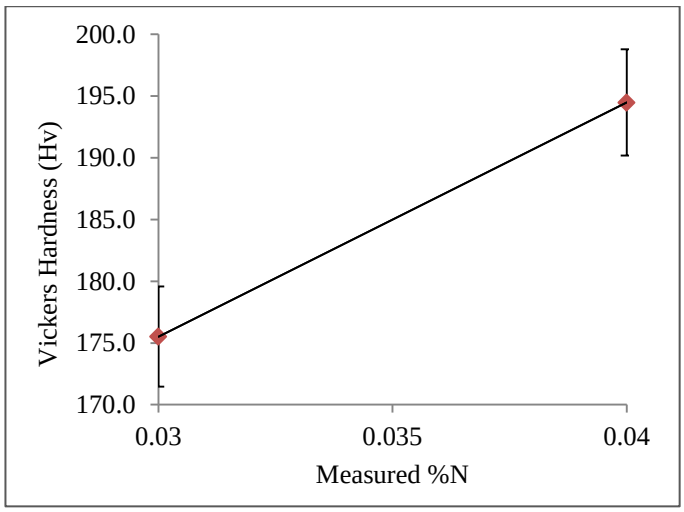

Figure 5.1.1. Influence of maximum attainable nitrogen content in cladded layers after Nd-YAG laser cladding of AISI410L powder in a fully diatomic nitrogen (N_2) atmosphere on the Vickers hardness of the layers (with 95% confidence interval).

5.2 THE INFLUENCE OF Si_3N_4 POWDER ADDITIONS TO AISI 410L ON THE DEPOSIT MICROSTRUCTURE AND HARDNESS AFTER LASER CLADDING

As shown in Figure 4.4.1 in the previous chapter, the influence of Si_3N_4 additions on the deposit microstructure and hardness was examined by adding sufficient Si_3N_4 to the AISI 410L powder feed to yield maximum calculated nitrogen contents in the clad deposit ranging from 0 wt% to 0.5 wt% (in 0.1 wt% increments). Figures 5.2.1(a) to (d) contain optical photomicrographs of the clad layers obtained. The deposit microstructures are largely ferritic, but an increase in martensite content with an increase in theoretical nitrogen content is evident. A fully martensitic microstructure could, however, not be obtained with the addition of Si_3N_4 to AISI 410L powder in the range investigated.

A marked increase in porosity is also evident as the theoretical nitrogen content increases to 0.5 wt%. This indicates that the nitrogen solubility limit was increasingly exceeded with increased Si_3N_4 additions to the powder feed. The incidence of porosity and the absence of fully martensitic microstructures suggest that *in-situ* alloying of AISI 410L stainless steel with nitrogen will only be viable if the nitrogen solubility limit in the deposit can be increased.

Figure 5.2.2 shows the results of hardness tests conducted on samples alloyed with increasing amounts of nitrogen during cladding. The hardness indentations were made on the top surface of each layer at the clad centreline. The hardness measurements indicate that there is a general increase in hardness with an increase in the theoretical percentage nitrogen in the deposit. The layers deposited at a total powder feed rate of 15 g/min exhibit higher hardness than layers deposited at a feed rate of 30 g/min, with maximum hardness levels of 307 HV and 378 HV achieved at the different feed rates. This can be attributed to the lower levels of nitrogen in the single-layer deposits performed at the higher powder feed rates (as shown in Figure 5.2.3) and to higher levels of dilution with the carbon steel substrate.

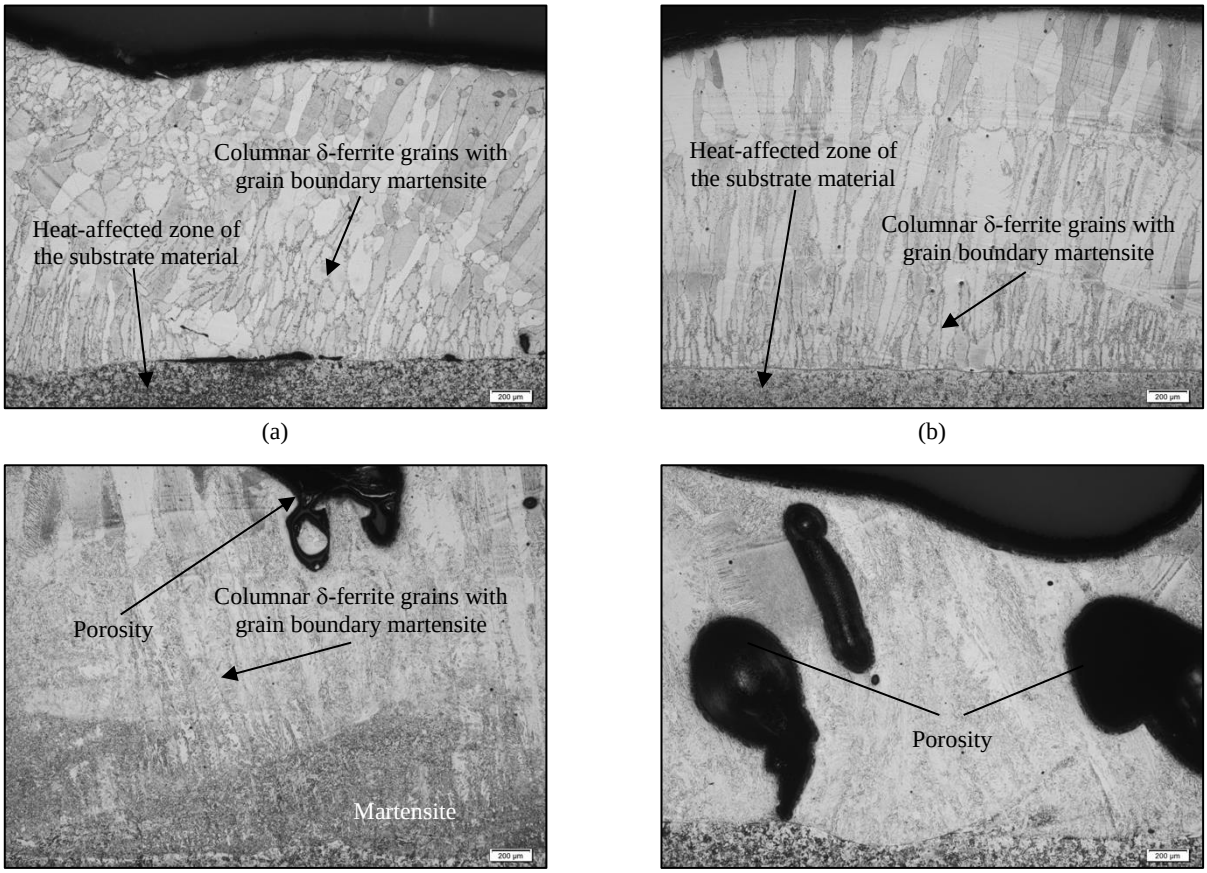

Figure 5.2.1. Optical photomicrographs of: **(**a) the unmodified AISI 410L clad deposit, performed at a feed rate of 30 g/min; (b) the AISI 410L clad deposit with a theoretical N content of 0.1 wt%, performed at a feed rate of 15 g/min; (c) the AISI 410L clad deposit with a theoretical N content of 0.3 wt%, performed at a feed rate of 15 g/min; and (d) the AISI 410L clad deposit with a theoretical N content of 0.5 wt%, performed at a feed rate of 30 g/min.

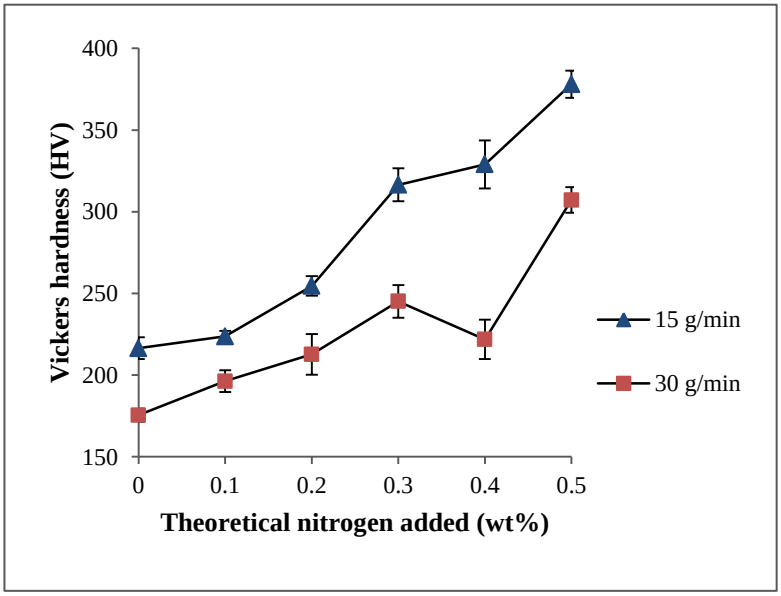

Figure 5.2.2. Hardness of deposited AISI 410L layers as a function of increasing theoretical nitrogen content (or increasing Si_3N_4 powder addition) for 15 g/min and 30 g/min total feed rates (with 95% confidence interval).

Figure 5.2.3 shows the weight percentage nitrogen dissolved in the deposits during cladding, expressed as the average percentage nitrogen measured experimentally using inert gas fusion analysis techniques. Although a general increase in the amount of nitrogen dissolved during cladding is evident with an increase in Si_3N_4 content in the powder feed, the trend shown in Figure 5.2.3 does not correlate well with that shown in Figure 5.2.2. This can be ascribed to the observed increase in porosity, which detracts from the analytical accuracy. A drop in dissolved nitrogen (Figure 5.2.3) and a consequent drop in hardness (Figure 5.2.2) is observed at a theoretical nitrogen content of 0.4 wt% for cladded layers deposited at a total powder feed rate of 30 g/min. The exact mechanism for this is unclear although strong fluctuations in the relevant observed amount of porosity could be indicative of fluctuating nitrogen desorption from the melt during solidification. The amount of martensite also appears to fluctuate in the microstructures of Figure 5.2.1 with added amounts of Si_3N_4, highlighting the lack of precise correlation in the trends of Figures 5.2.2 and 5.2.3. The maximum nitrogen content measured in the clad deposit was 0.063 wt%, which is well below the required concentration of 0.08 wt%.

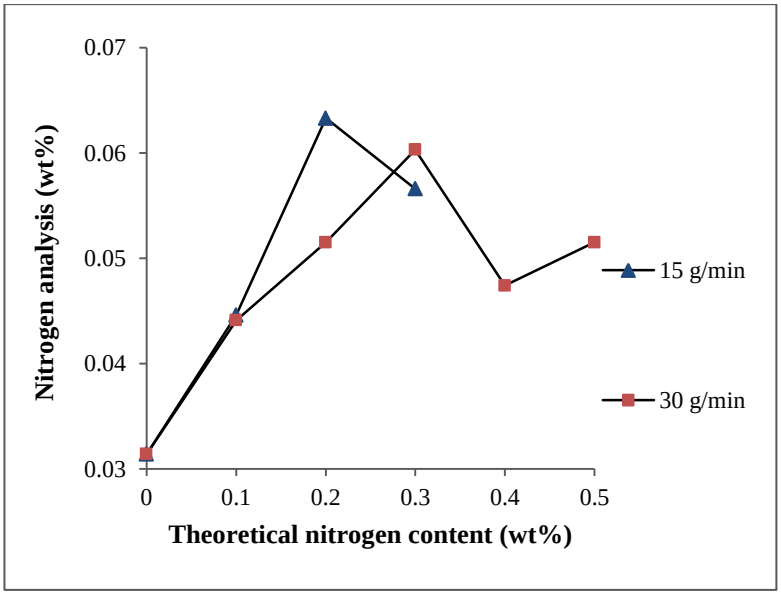

Figure 5.2.3. The amount of nitrogen dissolved in the deposit layers as a function of the theoretical amount of nitrogen added in the form of Si_3N_4 powder.

These results show that additions of Si_3N_4 to AISI 410L powder cannot ensure fully martensitic microstructures after laser cladding without causing unwanted nitrogen-induced porosity at higher Si_3N_4 levels. Successful *in-situ* alloying with nitrogen during laser cladding would therefore require the nitrogen solubility limit in AISI 410L stainless steel to be increased.

5.3 THERMODYNAMIC PREDICTION OF ALLOYING ELEMENT INTERACTIONS

As described in section 2.3.4, manganese is known to increase the nitrogen solubility limit in stainless steels on account of its negative interaction parameter with nitrogen. Although nickel tends to decrease the nitrogen solubility in stainless steel, it is a strong austenite-former and is expected to reduce the δ-ferrite content of the deposit and enlarge the austenite phase field at elevated temperatures. Since martensite forms from

austenite, an austenitic structure at elevated temperature is a prerequisite for the formation of a fully martensitic structure on cooling. The presence of austenite at elevated temperatures on cooling is also likely to increase the nitrogen solubility, as austenite has a higher solubility limit for nitrogen than ferrite or martensite. Thermodynamic predictions describing the effect of nickel and manganese additions on the microstructure and nitrogen solubility of nitrogen-alloyed AISI 410L stainless steel are considered in this section.

Figure 5.3.1 shows the influence of increasing nickel content on the amount of high temperature austenite, as predicted by Thermocalc™ for the AISI 410L-Ni-Si-N system at a maximum theoretical nitrogen content of 0.45%. At temperatures of 1200°C and 1060°C, a nitrogen-alloyed AISI 410L stainless steel is fully austenitic over the entire range of nickel contents evaluated. At 800°C, the amount of austenite increases from 28% at 0 wt% nickel to an almost fully austenitic structure at 1 wt% nickel due to the strong austenite-forming ability of nickel in stainless steel. A fully austenitic structure at higher temperatures facilitates the formation of a fully martensitic structure on cooling after cladding, provided the cooling rate is fast enough and the M_s and M_f temperatures are above room temperature.

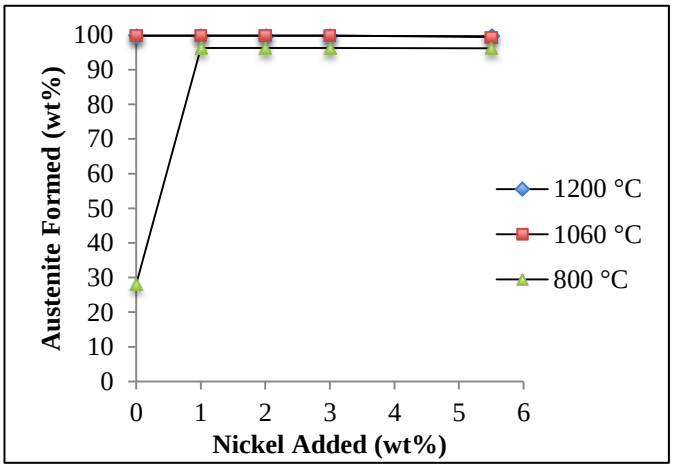

Figure 5.3.1. The predicted amount of high temperature austenite as a function of nickel content, calculated using at 800°C, 1060°C and 1200°C in the AISI 410L-Ni-Si-N system (for a theoretical nitrogen content of 0.45%).

The calculated nitrogen solubility in AISI 410L alloyed with nickel is shown in Figure 5.3.2. At 800°C, an increase in nickel content from 0 wt% to 1 wt% results in a slight increase in nitrogen solubility, which corresponds to the change in microstructure from largely ferritic at 0 wt% nickel to almost fully austenitic at 1 wt% (as shown in Figure 5.3.1). Austenite has a significantly higher solubility for nitrogen than ferrite or martensite, and a higher volume fraction of austenite at a given temperature therefore tends to increase the nitrogen solubility limit at that temperature as evident at 800ºC. At 1200°C and 1060°C, the alloy is fully austenitic, and an increase in nickel content leads to a decrease in nitrogen solubility. This is due to the positive interaction parameter of nickel with nitrogen which affects the nitrogen solubility directly. Therefore, with a higher percentage nickel, the positive interaction parameter between nickel and nitrogen consistently lowers the nitrogen solubility as observed in figure 5.3.2.

Figure 5.3.3 shows the effect of increasing manganese content on the amount of nitrogen dissolved in the austenite and ferrite phases for the AISI 410L-Mn-Si-N system. Due to the negative interaction parameter between manganese and nitrogen, the addition of manganese increases the nitrogen solubility limit over the entire temperature range evaluated. A similar trend is evident in Figure 5.3.4, which shows the effect of increasing manganese content on the amount of nitrogen dissolved in AISI 410L-Mn-Ni-Si-N alloys at a fixed nickel content of 2 wt%. At 2 wt% nickel, the microstructure is fully austenitic at all three temperatures and the observed increase in nitrogen solubility can be attributed to the influence (negative interaction parameter with nitrogen) of manganese.

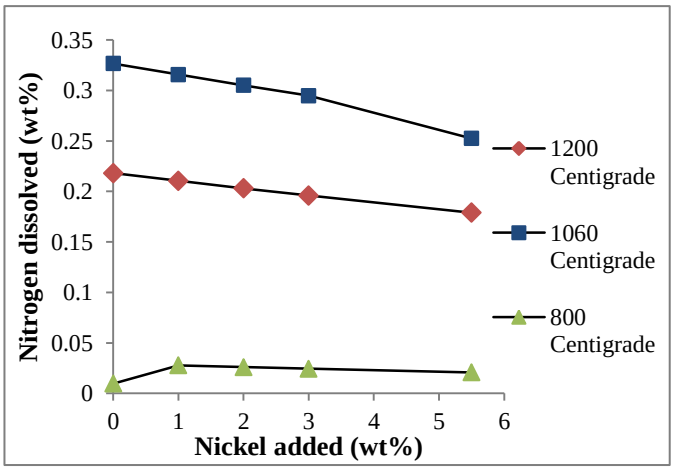

Figure 5.3.2. Nitrogen dissolved in the ferrite and austenite phases as a function of nickel content, calculated using Thermocalc™ at 800°C, 1060°C and 1200°C for the AISI 410L-Ni-Si-N system (for a theoretical nitrogen content of 0.45%).

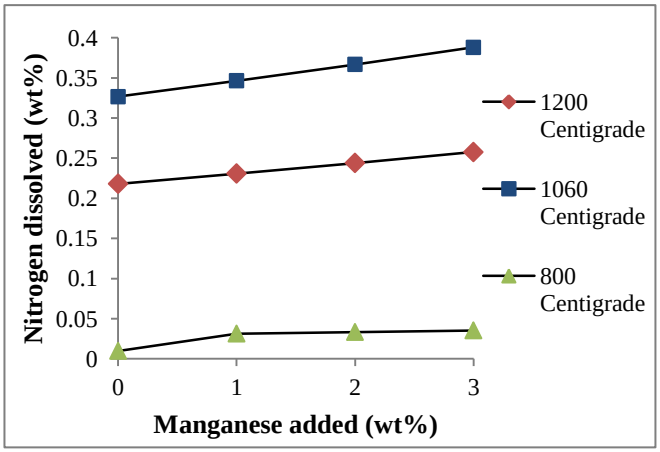

Figure 5.3.3. Nitrogen dissolved in the ferrite and austenite phases as a function of manganese content, calculated using Thermocalc™ at 800°C, 1060°C and 1200°C for the AISI 410L-Mn-Si-N system.

The increase in nitrogen solubility at 800°C in Figure 5.3.3 on addition of 1 wt% manganese coincides with an increase in the temperature range over which high temperature austenite is stable. This agrees with the findings of Kemp *et al.* [1] who reported that at low interstitial contents, manganese acts as a weak austenite-

former, regardless of its concentration. An increase in manganese content also increases the austenite stability range by enhancing nitrogen solubility (nitrogen is a strong austenite-former in stainless steels).

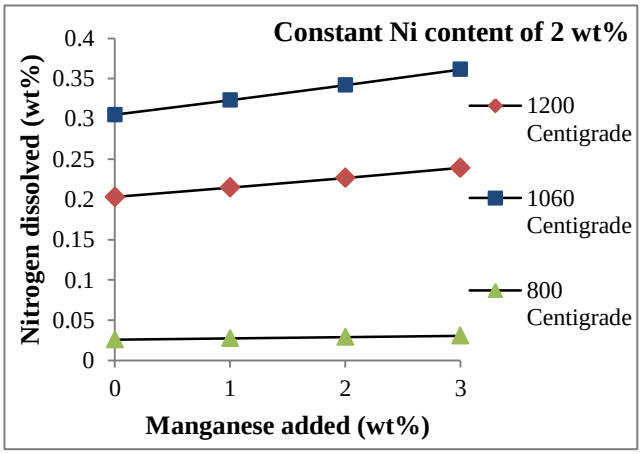

Figure 5.3.4. Nitrogen dissolved in the ferrite and austenite phases as a function of manganese content (at a fixed nickel content of 2 wt%), calculated using Thermocalc™ at 800°C, 1060°C and 1200°C for the AISI 410L-Mn-Ni-Si-N system.

In the AISI 410L-Ni-Si-N system, the equilibrium nitrogen solubility at 1060°C for a nickel content of 3 wt% is approximately 0.3 wt%. At the same temperature, the calculated nitrogen solubility is 0.39 wt% in a 3 wt% manganese alloy (in the AISI 410L-Mn-Si-N system) and 0.36 wt% in an alloy containing 3 wt% manganese and 2 wt% nickel (in the AISI 410L-Ni-Mn-Si-N system). This suggests that the addition of manganese is the most effective means of increasing the nitrogen solubility of AISI 410L. This agrees well with the curves shown in Figure 5.3.5, which represent the predicted high temperature nitrogen solubility limits for four alloys in the AISI 410L-Si-N, AISI 410L-Mn-Si-N, AISI 410L-Ni-Si-Ni, and AISI 410L-Ni-Mn-Si-N alloy systems as a function of temperature.

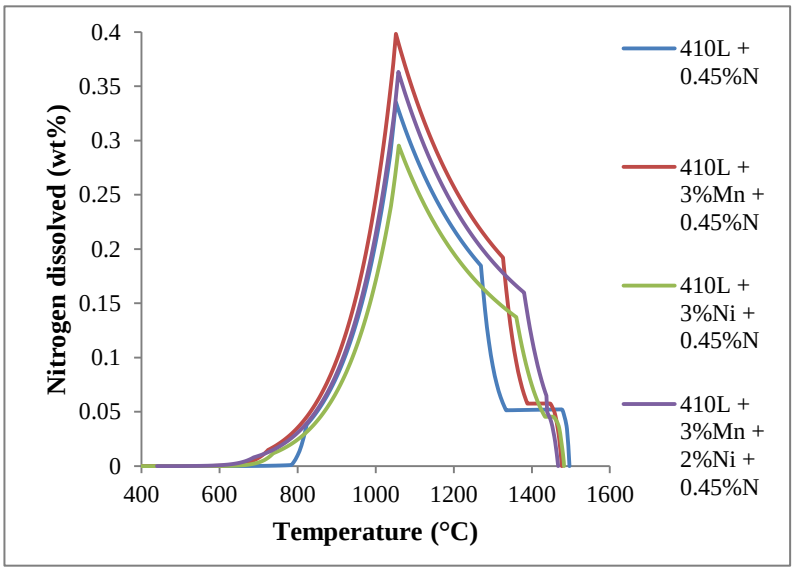

Figure 5.3.5. Nitrogen solubility in the AISI 410L-Si-N, AISI 410L-Mn-Si-N, AISI 410L-Ni-Si-N and AISI 410L-Ni-Mn-Si-N alloy systems as a function of temperature, calculated using Thermocalc™.

From Figure 5.3.5, it is evident that, at peak solubility (around 1050°C), alloys with no added manganese and high nickel contents (such as AISI 410L-3Ni-0.45N) exhibit very low nitrogen solubility. The addition of nickel increases the stability of austenite at high temperatures to some extent, but alloying with nickel also reduces the nitrogen solubility limit due to the positive interaction parameter of nickel with nitrogen. Alloys with high manganese contents and no added nickel (such as AISI 410L-3Mn-0.45N in Figure 5.3.5) demonstrate the highest nitrogen solubility limits.

5.4 THE INFLUENCE OF MANGANESE, NICKEL AND Si_3N_4 ADDITIONS ON THE MICROSTRUCTURE, HARDNESS AND NITROGEN CONTENT OF AISI 410L CLAD DEPOSITS

The thermodynamic predictions described in section 5.3 suggest that the most effective method of increasing the nitrogen solubility limit in AISI 410L is through alloying with manganese. In order to test the influence of manganese and nickel additions on the microstructure, hardness and nitrogen content of experimental AISI 410L clad deposits (with and without Si_3N_4 additions to the powder feed), the experimental procedure described in section 4.7 was followed.

Figure 5.4.1 shows the surface appearance of the most highly alloyed AISI 410L-Mn, AISI 410L-Ni and AISI 410L-Mn-Ni single-layer clad samples deposited in accordance with the experimental procedure shown schematically in Figure 4.7.1. No Si_3N_4 powder was added to any of these samples. The layers are uniform in appearance and no porosity is visible on any of the deposit surfaces.

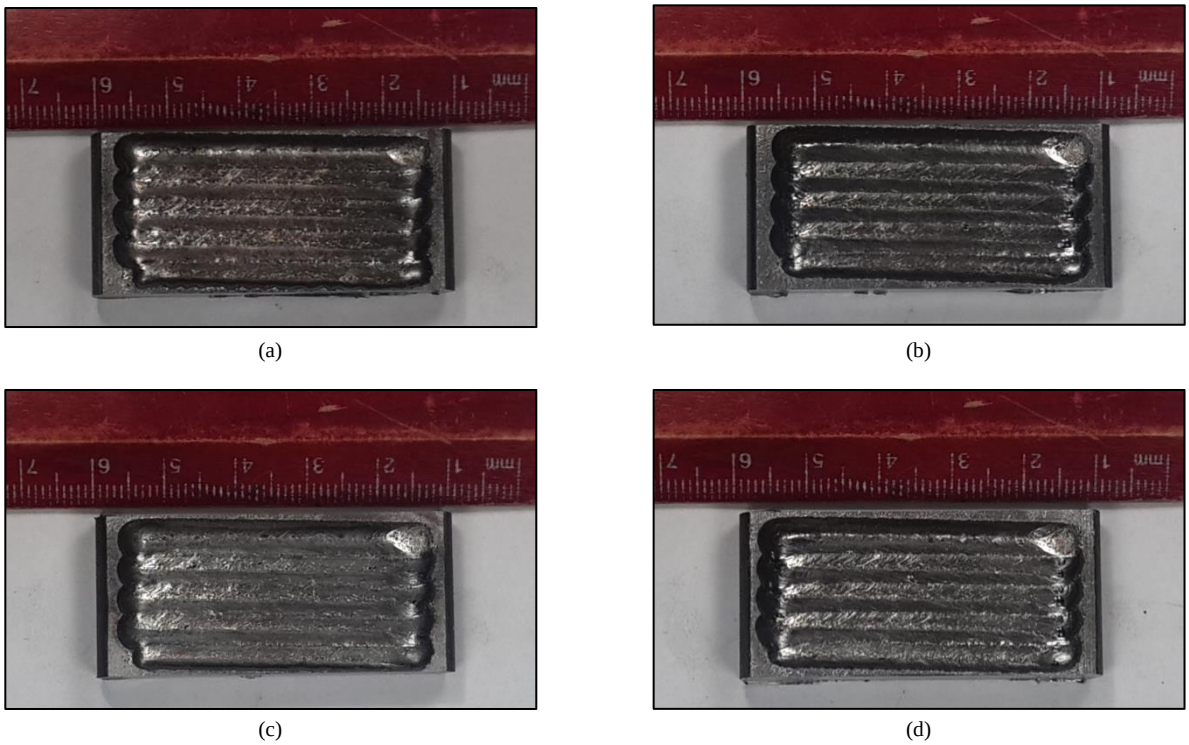

(a) (b)

(c) (d)

Figure 5.4.1. Single-layer clad deposit surfaces for: (a) unmodified AISI 410L; (b) AISI 410L-3.5Mn; (c) AISI 410L-5.5Ni; and (d) AISI 410L-3.5Mn-2.5Ni (all samples produced at a total feed rate of 30 g/min).

Figure 5.4.2 shows the surfaces of corresponding samples deposited with Si_3N_4 powder additions (contributing a maximum theoretical nitrogen content of 0.45 wt%), in accordance with the experimental procedure shown schematically in Figure 4.7.2. Considerably more nitrogen-induced porosity is evident, suggesting that the nitrogen solubility limit was exceeded during cladding. As predicted by Figure 5.3.5, the manganese-alloyed sample, Figure 5.4.2(b), has the highest nitrogen solubility limit of the samples evaluated and therefore the least amount of visible porosity. The majority of the pores seem to be associated with the interbead regions where cooler temperatures during cladding promote nitrogen degassing.

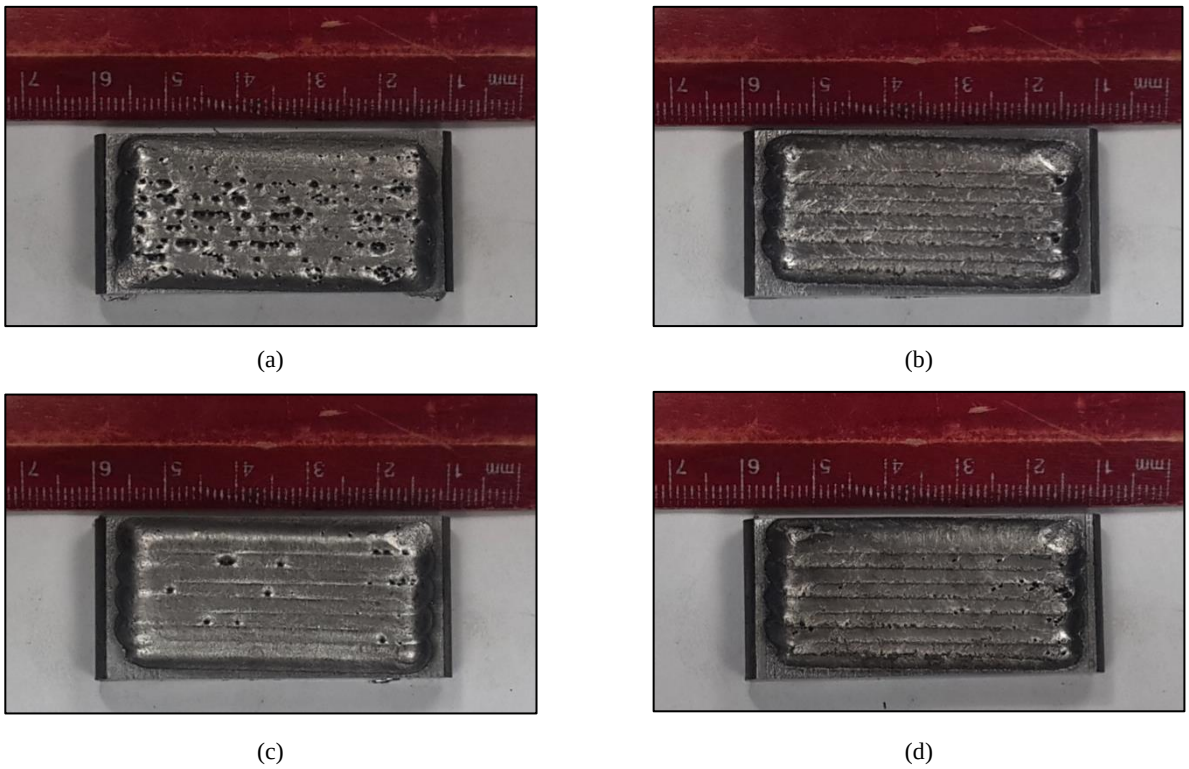

(a) (b)

(c) (d)

Figure 5.4.2. Two-layer clad deposit surfaces for: (a) AISI 410L-0.45N; (b) AISI 410L-3.5Mn-0.45N; (c) AISI 410L-5.5Ni-0.45N; and (d) AISI 410L-3.5Mn-2.5Ni-0.45N (all samples produced at a total feed rate of 15 g/min).

Figures 5.4.3 to 5.4.7 show the deposit microstructures after etching for the experimental alloys described in Figures 4.7.1 and 4.7.2. Figure 5.4.3 and 5.4.4 show the deposits made without any Si_3N_4 addition at a powder feed rate of 15 g/min at various magnifications. Figures 5.4.5, 5.4.6, and 5.4.7 show the deposits after Si_3N_4 addition (contributing a maximum theoretical nitrogen content of 0.45 wt%) at various magnifications, produced at powder feed rates of 15 g/min (Figures 5.4.5 and 5.4.6) and 30 g/min (Figure 5.4.7), respectively.

As shown in Figures 5.4.3(a) and 5.4.4(a), the microstructure of the unmodified AISI 410L deposit is largely ferritic with some martensite at the δ-ferrite grain boundaries in the more highly diluted first layer. Almost fully martensitic microstructures are obtained with the addition of 3.5 wt% manganese (singly or in combination with nickel), confirming the findings of Kemp *et al.* [1]. With the addition of 5.5 wt% nickel,

almost fully martensitic microstructures are achieved due to the suppression of δ-ferrite formation on cooling.

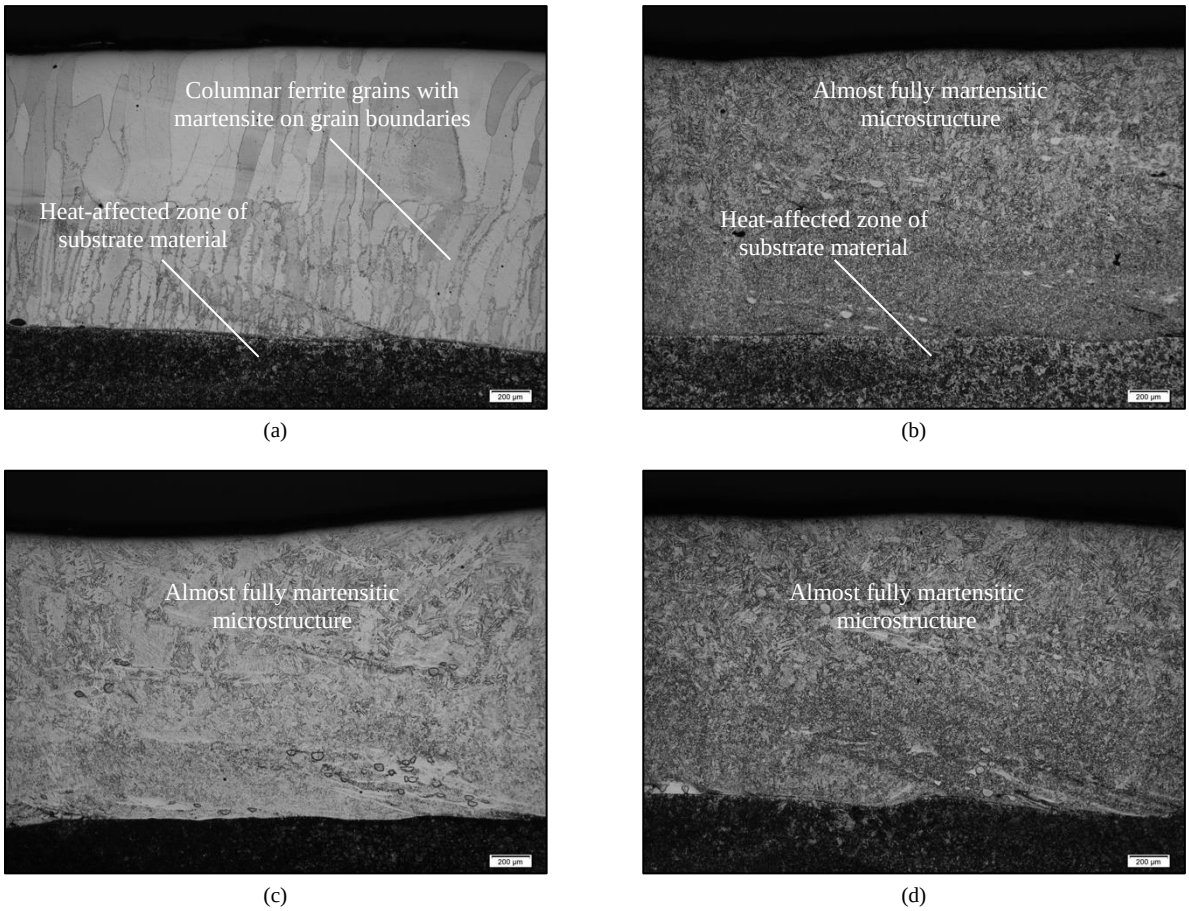

Figure 5.4.3. Optical photomicrographs of two-layer clad deposits for: (a) unmodified AISI 410L; (b) AISI 410L-3.5Mn; (c) AISI 410L-5.5Ni; and (d) AISI 410L-3.5Mn-2.5Ni (all samples produced at a total feed rate of 15 g/min).

Clad deposits produced using AISI 410L powder mixed with Si_3N_4 to a level corresponding to a maximum theoretical nitrogen content of 0.45 wt%, shown in Figures 5.4.2(a), 5.4.5(a), 5.4.6(a) and 5.4.7 (a) contain a large amount of porosity and microstructures consisting of columnar δ-ferrite grains and grain boundary martensite. The increase in martensite content on addition of Si_3N_4 to the powder feed suggests that some nitrogen pick-up had occurred, but it is evident that the nitrogen solubility limit had been exceeded on solidification, resulting in porosity. With the addition of 3.5 wt% manganese to this mixture, as shown in Figures 5.4.2(b), 5.4.5(b), 5.4.6(b) and 5.4.7 (b) the amount of porosity is reduced significantly and almost fully martensitic microstructures are obtained. This correlates well with the results shown in Figure 5.3.5, in which higher nitrogen solubility is predicted with the addition of manganese. Nitrogen in solid solution stabilises the austenite phase and suppresses δ-ferrite formation on cooling. The addition of nickel to the powder feed, shown in Figures 5.4.2(c), 5.4.5(c) 5.4.6(c) and 5.4.7 (c) promotes the formation of almost fully martensitic microstructures, but some porosity remains in the deposit. According to thermodynamic predictions, this sample is expected to have a lower nitrogen solubility limit (due to the positive interaction parameter between nickel and nitrogen) and therefore a greater tendency towards nitrogen-induced porosity

due to degassing during cladding. A similar trend is evident in samples alloyed with manganese and nickel, shown in Figures 5.4.2(d), 5.4.5(d) 5.4.6 (d) and 5.4.7(d).

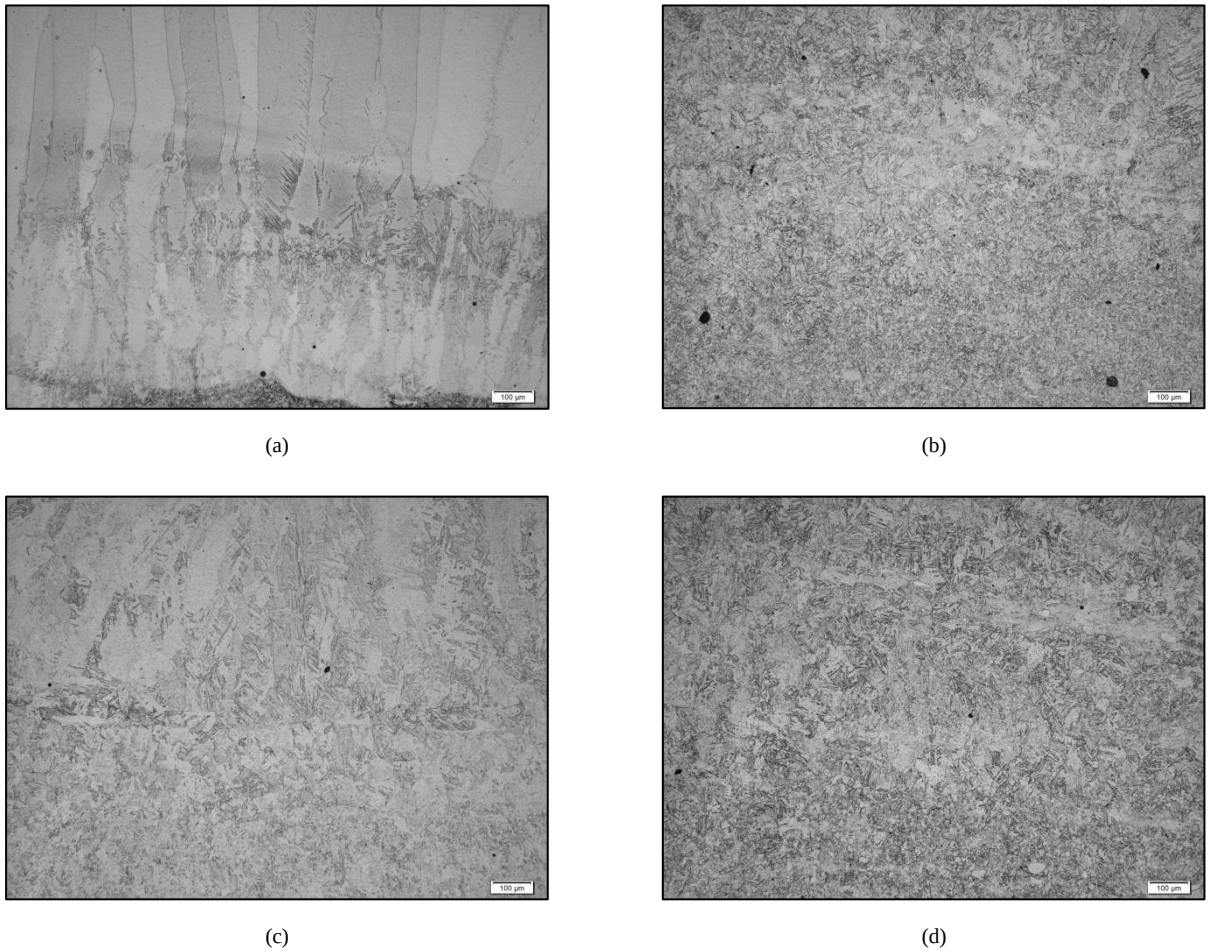

Figure 5.4.4. Optical photomicrographs at higher magnifications of the two-layer clad deposits for: (a) unmodified AISI 410L; (b) AISI 410L-3.5Mn; (c) AISI 410L-5.5Ni; and (d) AISI 410L-3.5Mn-2.5Ni (all samples produced at a total feed rate of 15 g/min).

Figure 5.4.8 shows the predicted amounts of high temperature austenite and δ-ferrite in the modified AISI 410L alloys at a range of temperatures from the liquidus to 1050°C. AISI 410L-0.45N solidifies as primary δ-ferrite and austenite only starts forming in the solid state at temperatures below about 1350°C. The addition of manganese (AISI 410L-3Mn-0.45N) does not change the primary solidification mode, but restricts the high temperature δ-ferrite phase field and expands the austenite stability range to higher temperatures. In this alloy austenite starts to form from δ-ferrite in the solid state at temperatures just below 1400°C. This deposit has a significantly higher nitrogen solubility which accounts for the wider austenite phase field (Figure 5.3.5). In steels alloyed with nickel and nitrogen (i.e. the AISI 410L-5.5Ni-0.45N and the AISI 410L-3Mn-2Ni-0.45N samples), austenitic solidification is promoted by the strong austenite-forming properties of nickel and the solidification mode appears to be a combination of austenitic and ferritic solidification, with austenite forming from the melt at temperatures just below the liquidus temperature. The addition of nickel to the clad deposit reduces the nitrogen solubility limit significantly (Figure 5.3.5),

suggesting that the presence of austenite during solidification does not compensate for the reduction in nitrogen solubility in nickel-alloyed deposits. Adding manganese and nickel in combination increases the nitrogen solubility somewhat, but the alloy still displays lower solubility for nitrogen than a corresponding alloy with the same manganese content and no nickel.

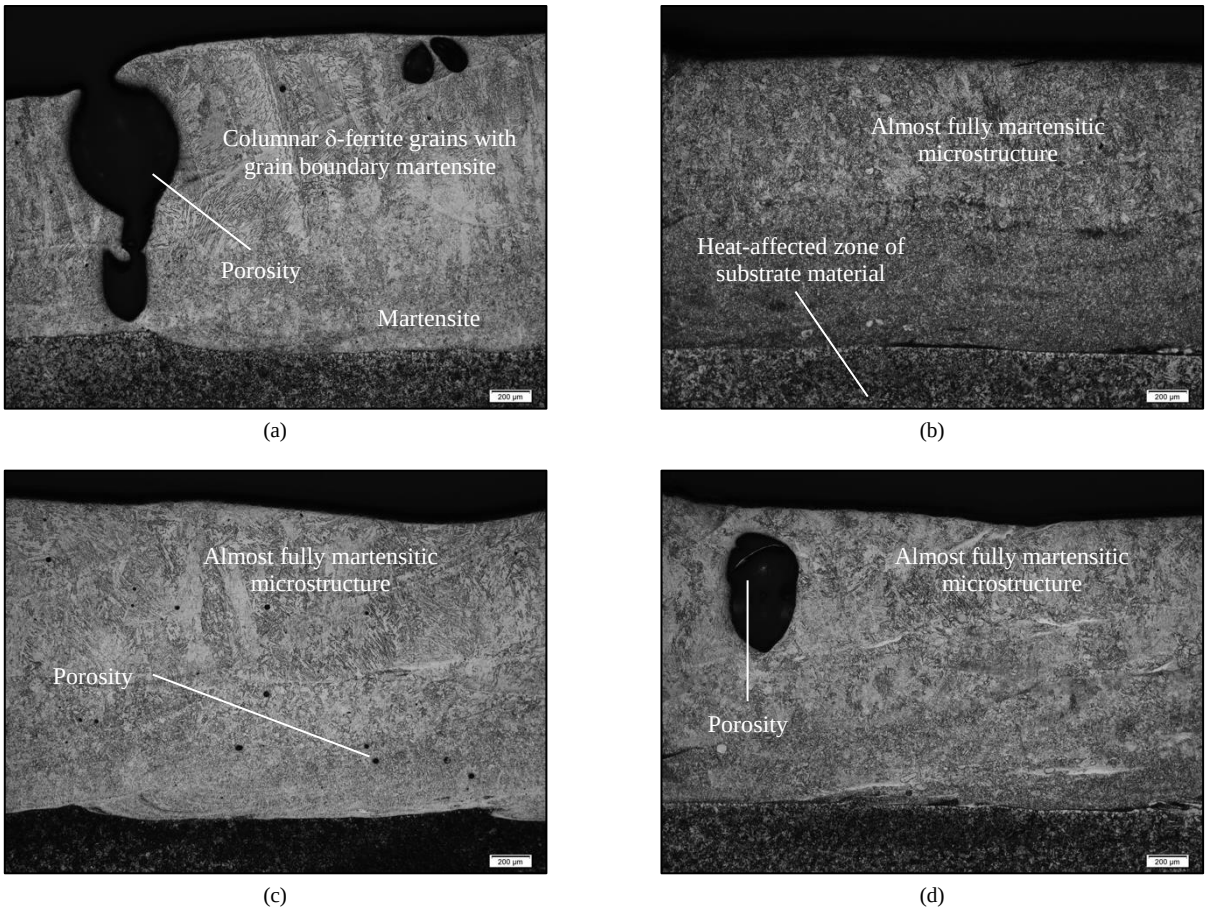

Figure 5.4.5. Optical photomicrographs of two-layer clad deposits for: (a) AISI 410L-0.45N; (b) AISI 410L-3.5Mn-0.45N; (c) AISI 410L-5.5Ni-0.45N; and (d) AISI 410L-3.5Mn-2.5Ni-0.45N (all samples produced at a total feed rate of 15 g/min).

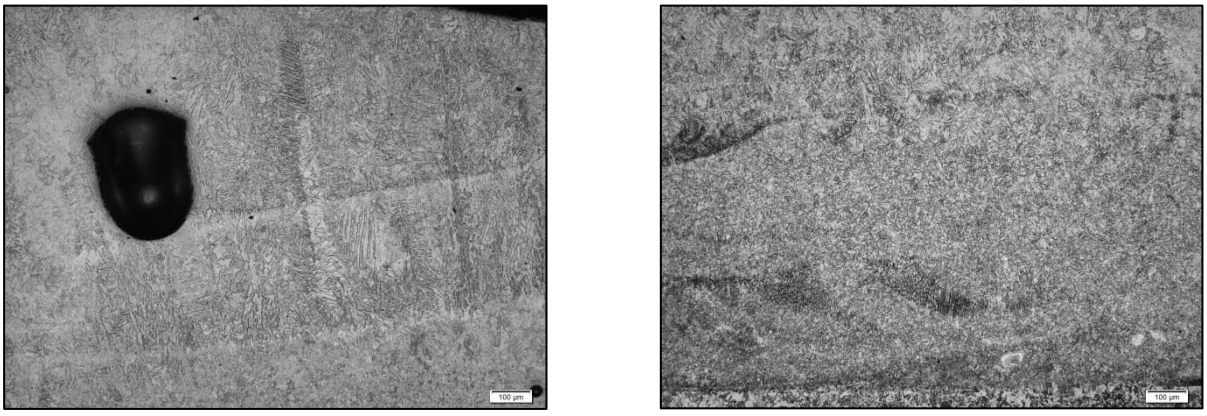

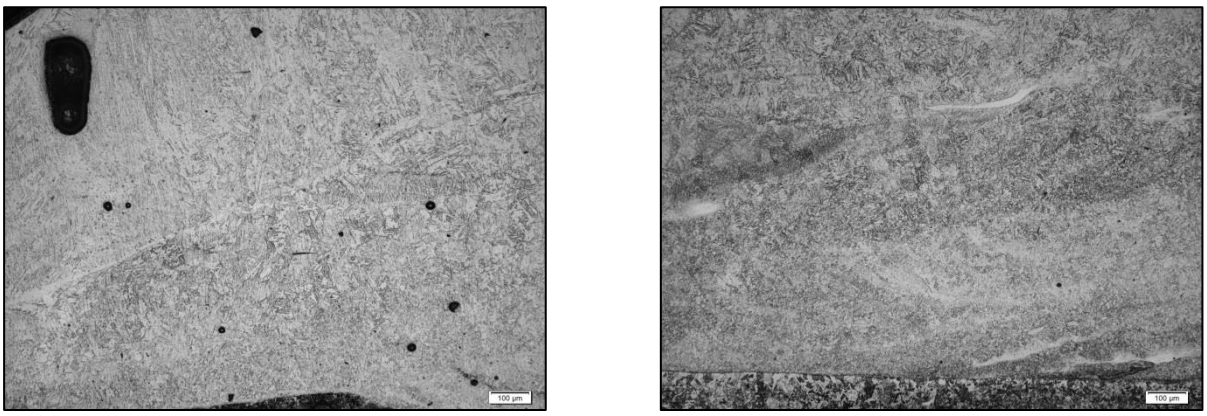

(c) (d)

Figure 5.4.6. Optical photomicrographs at higher magnifications of the two-layer clad deposits for: (a) AISI 410L-0.45N; (b) AISI 410L-3.5Mn-0.45N; (c) AISI 410L-5.5Ni-0.45N; and (d) AISI 410L-3.5Mn-2.5Ni-0.45N (all samples produced at a total feed rate of 15 g/min).

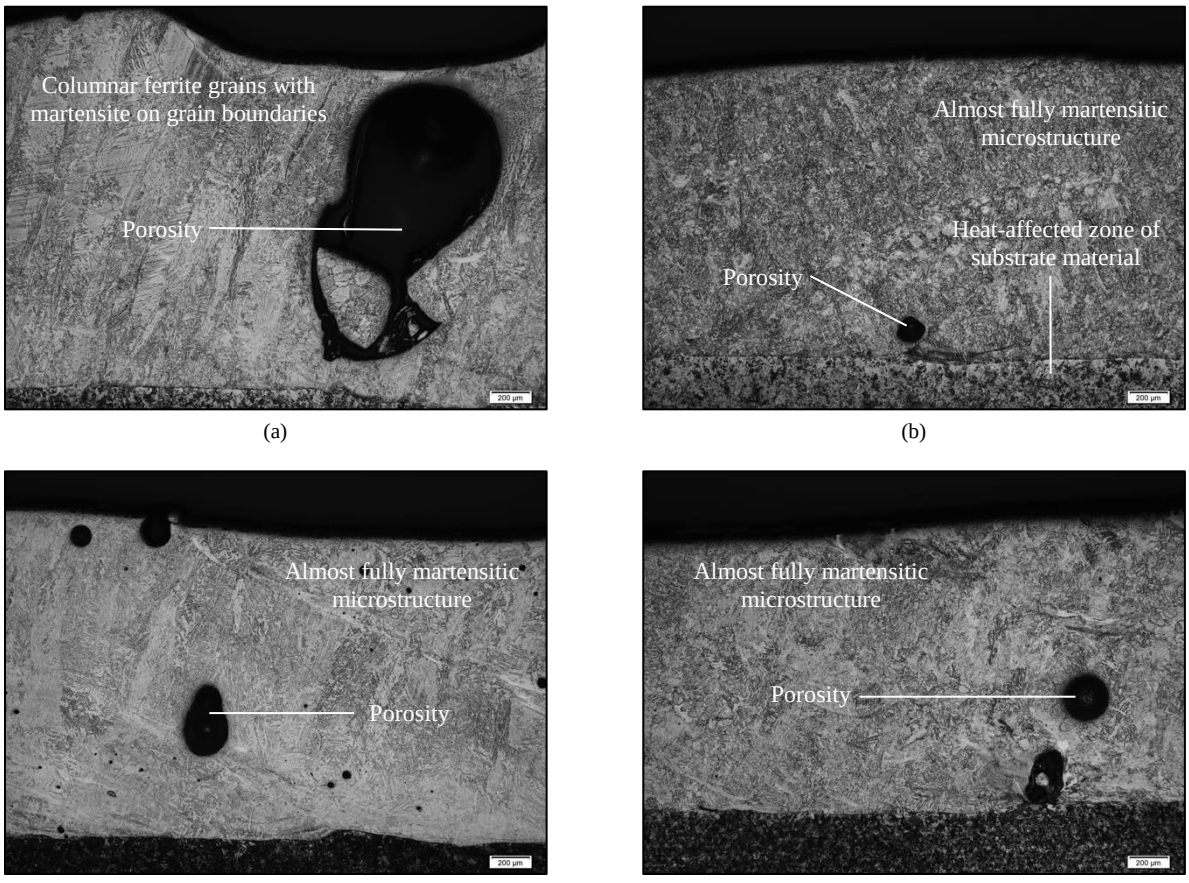

(a) (b)

(c) (d)

Figure 5.4.7. Optical photomicrographs of single-layer clad deposits for: (a) AISI 410L-0.45N; (b) AISI 410L-3.5Mn-0.45N; (c) AISI 410L-5.5Ni-0.45N; and (d) AISI 410L-3.5Mn-2.5Ni-0.45N (all samples produced at a total feed rate of 30 g/min).

Figure 5.4.9 shows the measured hardness of the nickel-alloyed AISI 410L-Ni and AISI 410L-Ni-Si-N deposits as a function of nickel content for samples prepared at total powder feed rates of 15 g/min and 30 g/min. Figure 5.4.10 shows the influence of manganese additions on the hardness of nickel-free AISI 410L-

Mn and AISI 410L-Mn-Si-N alloys, while Figure 5.4.11 shows the effect of manganese concentration on the hardness of nickel-containing AISI 410L-Mn-Ni and AISI 410L-Mn-Ni-Si-N alloys for different powder feed rates.

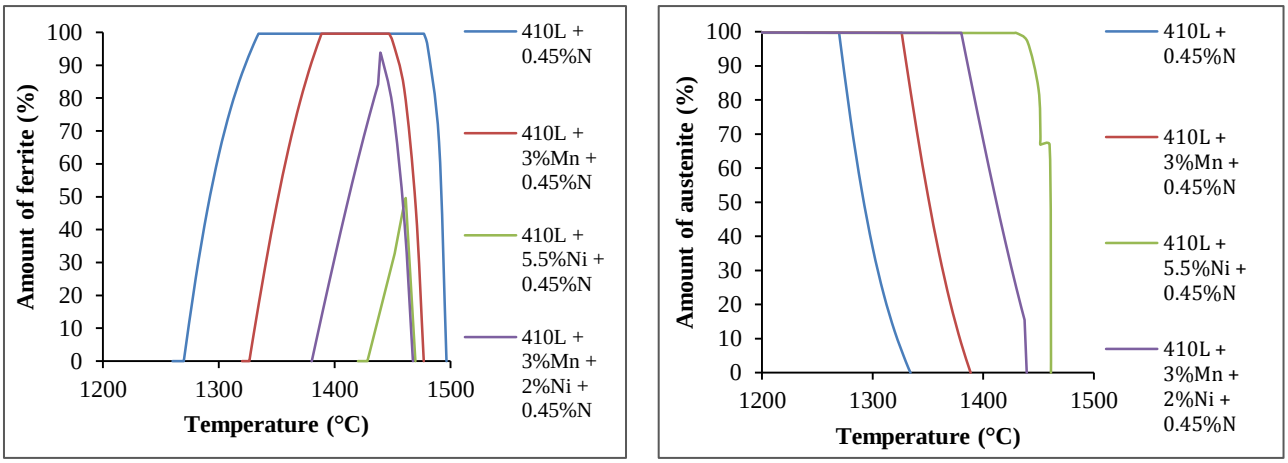

(a) (b)

Figure 5.4.8. Thermocalc™ prediction of the amounts of: (a) high temperature δ-ferrite; and (b) high temperature austenite present in modified AISI 410L alloys as a function of temperature during solidification.

Figure 5.4.9 shows that the addition of up to 2.5 wt% nickel to AISI 410L powder significantly increases the hardness of the deposit, even without any deliberate nitrogen addition. This can be attributed to expansion of the austenite phase field at the expense of δ-ferrite in the presence of nickel (nickel is a powerful austenite-forming element), which promotes the formation of more martensite on cooling to room temperature. Figure 5.3.1 suggests that the addition of more than 1 wt% nickel no longer affects the deposit austenite content at elevated temperatures, which explains why the measured hardness values in Figure 5.4.9 become independent of the nickel content at higher nickel concentrations. The addition of Si_3N_4 powder to the powder feed significantly increases the deposit hardness, suggesting that nitrogen is absorbed by the clad deposit on dissociation of Si_3N_4 during cladding. Nitrogen not only promotes the formation of more martensite on cooling, but is also an excellent interstitial solid solution strengthening element in stainless steel.

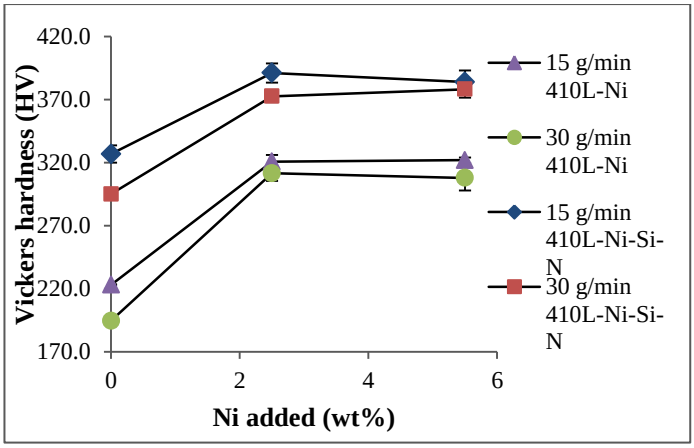

Figure 5.4.9. Hardness of nickel-alloyed AISI 410L-Ni and AISI 410L-Ni-Si-N deposits for total powder feed rates of 15 g/min and 30 g/min (with 95% confidence interval).

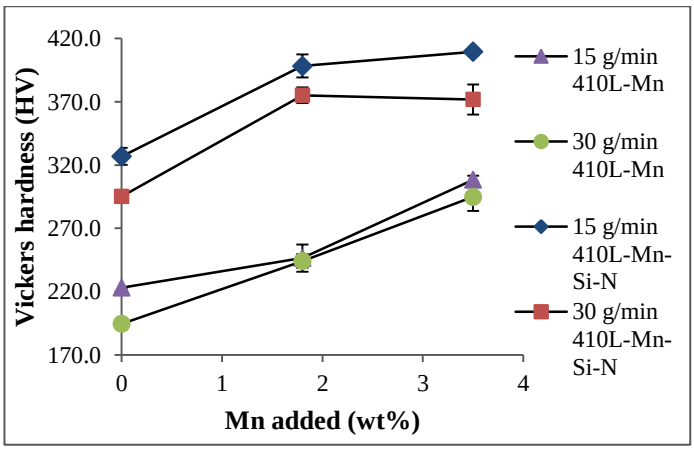

Figure 5.4.10. Hardness of manganese-alloyed AISI 410L-Mn and AISI 410L-Mn-Si-N deposits for total powder feed rates of 15 g/min and 30 g/min (with 95% confidence interval).

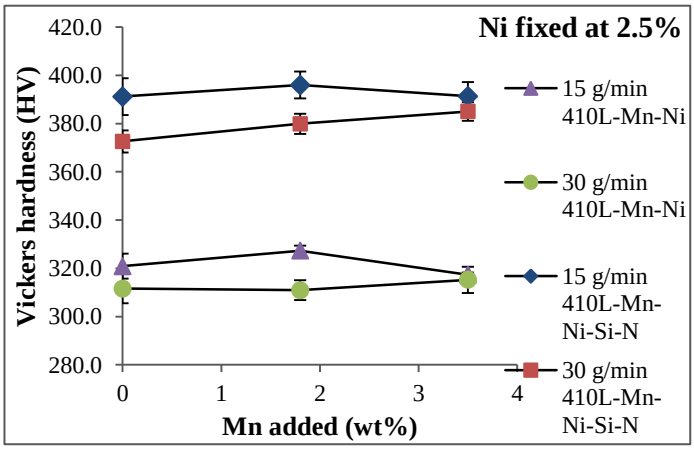

Figure 5.4.11. Hardness of Ni- and Mn-alloyed AISI 410L-Mn-Ni and AISI 410L-Mn-Ni-Si-N deposits as a function of manganese content, for total powder feed rates of 15 g/min and 30 g/min (with 95% confidence interval).

The cladded layers were produced as single and double layers as discussed in section 4.7.2. The same alloy was cladded as a single layer at a total feed rate 30 g/min and as a double layer at 15 g/min for each alloying system under investigation. The double-layer deposits consistently delivered a higher hardness and higher nitrogen content than the single-layer deposits throughout the results of Figures 5.4.9 to 5.4.14. This could be attributed to the higher cooling rate consequent to the lower overall heat input used to create the double layers.

The addition of manganese to the powder feed increases the deposit hardness significantly, as shown in Figure 5.4.10. Not only is manganese a strong solid solution strengthening element, but it also increases the solubility of nitrogen in stainless steel, allowing more nitrogen to be absorbed from the dissociated Si_3N_4 powder during cladding (and also to a lesser extent from the nitrogen shielding and carrier gas atmospheres). Since nitrogen is a strong austenite-former, the austenite phase field expands with the addition of manganese, promoting the formation of more martensite on cooling. The addition of manganese to the nickel-alloyed clad deposits has little effect on the hardness as nickel tends to counteract the beneficial influence of manganese on the nitrogen solubility limit as evident from Figure 5.4.11.

The nitrogen-alloyed deposit containing 3.5 wt% manganese displayed the highest hardness of the samples tested (410 HV for a feed rate of 15 g/min), compared with maximum hardness values of 384 HV and 391 HV measured in the AISI 410L-Ni-Si-N and AISI 410L-Mn-Ni-Si-N samples, respectively.

The increase in hardness of the cladded layers when nitrogen is dissolved in the structure can be ascribed to nitrogen forming an interstitial solid solution, effectively increasing the hardness of martensite. It also acts as a high-temperature austenite former (and stabiliser), leading to a lower delta ferrite volume percentage in the room-temperature microstructures of the cladded layers, assuming no residual austenite remains.

The measured nitrogen contents of the clad deposits (determined using inert gas fusion analysis techniques) are shown in Figures 5.4.12, 5.4.13 and 5.4.14. The highest nitrogen contents in the nickel-alloyed clad layers were obtained at a total powder feed rate of 15 g/min for the deposit with the highest nickel concentration, which correlates well with the maximum hardness values shown in Figures 4.5.9 and 4.5.11. The influence of powder feed rate on nitrogen absorption during cladding is considered in more detail in section 5.5.

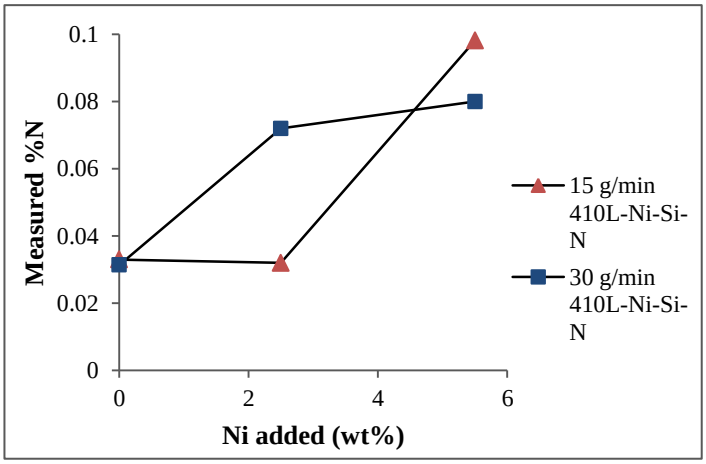

Figure 5.4.12. Measured nitrogen content in the AISI 410L-Ni-Si-N deposits as a function of nickel content and powder feed rate.

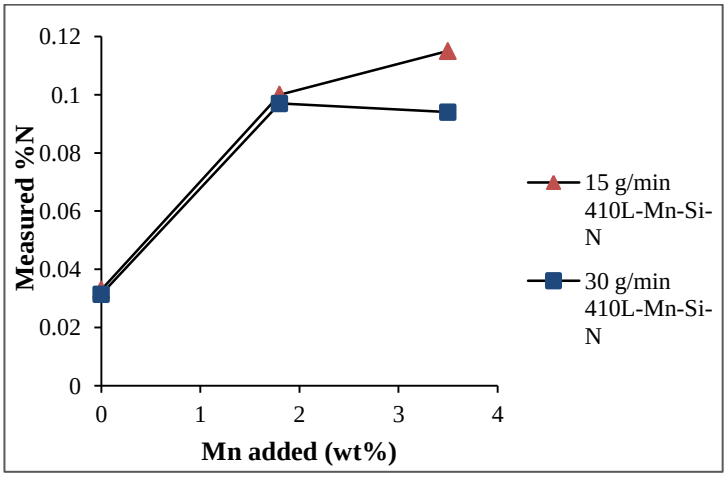

Figure 5.4.13. Measured nitrogen content in the AISI 410L-Mn-Si-N deposits as a function of manganese content.

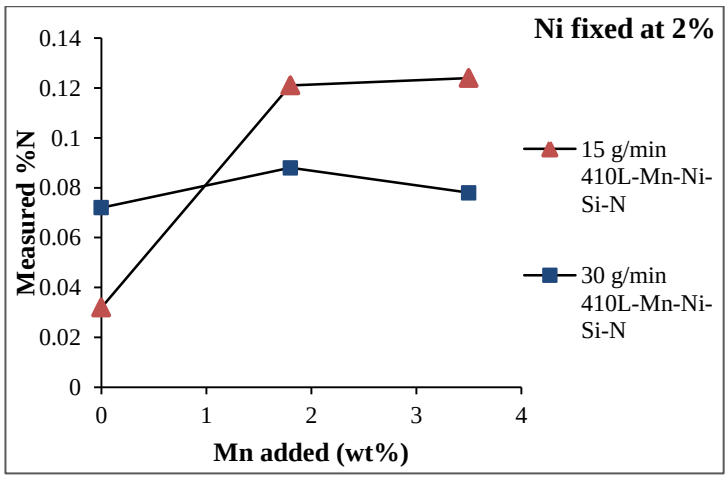

Figure 5.4.14. Measured nitrogen content in the AISI 410L-Mn-Ni-Si-N deposits as a function of manganese content.

The highest deposit nitrogen content (0.12 wt%) was measured in the manganese-alloyed AISI 410L-Mn-Si-N and AISI 410L-Mn-Ni-Si-N samples. This is in agreement with the findings of Huang *et al*. [2-7] (Table 2.3.3 in section 2.3.6). The lowest nitrogen content (0.1 wt%) was measured in the nickel-alloyed AISI 410L-Ni-Si-N alloys. This is consistent with the predicted nitrogen solubility limits shown in Figure 5.3.5. These results confirm that *in-situ* alloying with nitrogen by means of Si_3N_4 additions to the powder feed is possible, provided the nitrogen solubility limit in the steel is high enough to accommodate the additional nitrogen without promoting excessive porosity or retained austenite. Manganese additions proved to be particularly successful at increasing the nitrogen solubility limit in AISI 410L, and almost fully martensitic microstructures with hardness values in excess of 400 HV could be achieved by means of a 3.5 wt% manganese addition to nitrogen-alloyed AISI 410L.

5.5 EFFECT OF DILUTION ON CHEMICAL COMPOSITION

The tables below show the chemical analyses on cladded layers as discussed in section 5.4 of the study. Tables 5.5.1 and 5.5.2 correspond to the alloys prepared according to the methodology shown in Figure 4.7.1 at 15 and 30 g/min, respectively, and Tables 5.5.3 and 5.5.4 correspond to the alloys prepared according to the methodology shown in Figure 4.7.2 at 15 and 30 g/min respectively.

The tables give an indication of the effect of dilution between the metallurgical powders used and the partially melted medium-carbon steel substrate on the chemical analyses of the final cladded layers. Correlating the analysed compositions of cladded layers of pure 410L powder of Tables 5.5.1 and 5.5.2 with no further additives to the chemical composition of Table 4.2.1, which gave the nominal chemical composition of the AISI 410L powder used in this investigation, the chromium content seems too high if dilution is taken into account. Table 4.2.1 showed a chromium content of 12.1 wt% and a slightly lower concentration in the cladded layers is to be expected. This effect cannot be ascribed to any chromium in the medium-carbon steel substrate and is assumed to be a calibration error on the part of the analysis equipment used. Apart from this effect, the chromium contents seem to be reasonably consistent throughout Tables 5.5.1-5.5.4 with dilution not creating large fluctuations. According to Figure 2.3.3, chromium has a strong

effect on nitrogen solubility in stainless steel and a decrease in the chromium content would have resulted in a decrease in the nitrogen absorbed in the final cladded layers.

The manganese content is consistently higher than the content of the theoretical alloy systems. According to Table 4.2.1, the 410L powder used in the investigation had a manganese content of 0.61% and apart from the 410L cladded layers (with no additional additives) there seems to be an enrichment of manganese in all cladded layers in Tables 5.5.1-5.5.4 from the medium-carbon steel substrate at concentrations of 1-2 wt%. This again appears slightly too high and could be ascribed to calibration errors although the general trend of higher manganese levels seems to be consistent. Considering the effect of manganese on the solubility of nitrogen in stainless steel, this would have led to an increase in the absorbed nitrogen in the final cladded layers.

The nickel concentrations are on average lower than in the theoretical alloys by less than 1 wt%, which is to be expected as no nickel was reported in the nominal composition of Table 4.2.1. This would have decreased the high-temperature austenite formation of the alloy systems, which would have led to lower levels of nitrogen in the final cladded layers due to austenite's high solubility for nitrogen. In the case of fully austenitic high-temperature microstructures, this would have led to an increase in the nitrogen absorbed in the final cladded layers due to the positive interaction parameter between nickel and nitrogen.

In the alloy system AISI 410L-Ni-Mn of Tables 5.5.2 and 5.5.4 (last columns) there appears to be a higher nickel concentration than expected from the theoretical alloys which would lead to lower nitrogen absorption in the cladded layers. These high concentrations cannot, however, be accounted for and is assumed to be due to calibration errors.

Table 5.5.1. Chemical composition of the AISI 410L-Mn; AISI 410L-Ni-Mn; and AISI 410L-Ni alloy systems, prepared using laser powder cladding at a powder feed rate of 15 g/min (corresponding to Figure 4.7.1)

15 g/min Double Layers Without N							
	410L	410L + 1.8% Mn	410L + 3.5% Mn	410L + 2.5% Ni	410L + 5.5% Ni	410L + 1.8% Mn + 2.5% Ni	410L + 3.5% Mn + 2.5% Ni
Carbon (C)	0.02	0.03	0.02	0.017	0.017	0.024	0.032
Chromium (Cr)	12.9	12.6	12.4	12.8	12.5	12.3	12.2
Manganese (Mn)	0.62	2.71	5.55	0.63	0.61	3.05	5.82
Nickel (Ni)	0.18	0.18	0.17	1.69	4.51	2.18	2.11
Silicon (Si)	0.57	0.58	0.56	0.54	0.49	0.56	0.52
Nitrogen (N)	0.0404	0.039	0.0391	0.0392	0.0294	0.0402	0.033
Iron (Fe)	Balance	Balance	Balance	Balance	Balance	Balance	Balance

Figure 5.5.1 (a) - (d) is a collection of optical micrographs, taken from the samples prepared according to the alloy design methodology of Figures 4.7.1 and 4.7.2 showing the interface between the medium-carbon steel substrate and the cladded layers. Figure 5.5.1(a) is a double layer of the alloy system 410L-3.5Mn, deposited at a feed rate of 15 g/min, Figure 5.5.1(b) is a double layer of the alloy system 410L-3.5Mn-0.45N, deposited

at a feed rate of 15 g/min and Figures 5.5.1(c) and (d) represent a single layer of the alloy system 410L-1.8Mn-0.45N at different magnifications, deposited at a feed rate of 30 g/min.

Table 5.5.2. Chemical composition of the AISI 410L-Mn; AISI 410L-Ni-Mn; and AISI 410L-Ni alloy systems, prepared using laser powder cladding at a powder feed rate of 30 g/min (corresponding to Figure 4.7.1).

30 g/min Single Layers Without N							
	410L	410L + 1.8% Mn	410L + 3.5% Mn	410L + 2.5% Ni	410L + 5.5% Ni	410L + 1.8% Mn + 2.5% Ni	410L + 3.5% Mn + 2.5% Ni
Carbon (C)	0.018	0.023	0.025	0.023	0.023	0.017	0.017
Chromium (Cr)	12.9	12.6	12.3	12.6	12.4	12.3	12.1
Manganese (Mn)	0.66	3.17	5.51	0.66	0.61	3.35	6.42
Nickel (Ni)	0.19	0.18	0.18	2.6	5.09	2.66	2.59
Silicon (Si)	0.58	0.55	0.55	0.5	0.53	0.55	0.58
Nitrogen (N)	0.039	0.0369	0.0422	0.0363	0.0283	0.035	0.035
Iron (Fe)	Balance	Balance	Balance	Balance	Balance	Balance	Balance

Table 5.5.3. Chemical composition of the AISI 410L-Mn-Si-N; AISI 410L-Ni-Mn-Si-N; and AISI 410L-Ni-Si-N alloy systems, prepared using laser powder cladding at a powder feed rate of 15 g/min (corresponding to Figure 4.7.2).

15 g/min Double Layers With N							
	410L + 0.45% N	410L + 1.8% Mn + 0.45% N	410L + 3.5% Mn + 0.45% N	410L + 2.5% Ni + 0.45% N	410L + 5.5% Ni + 0.45% N	410L + 1.8% Mn + 2.5% Ni + 0.45% N	410L + 3.5% Mn + 2.5% Ni + 0.45% N
Carbon (C)	0.01	0.021	0.021	0.015	0.012	0.017	0.017
Chromium (Cr)	12.7	12.3	12.0	12.3	12.3	12.2	12.0
Manganese (Mn)	0.67	3.14	6.37	0.66	0.61	3.34	5.51
Nickel (Ni)	0.22	0.19	0.19	2.22	4.83	1.91	2.26
Silicon (Si)	0.89	0.78	0.85	0.82	0.79	0.8	0.8
Nitrogen (N)	0.0326	0.1	0.115	0.0318	0.0981	0.121	0.1243
Iron (Fe)	Balance	Balance	Balance	Balance	Balance	Balance	Balance

Table 5.5.4. Chemical composition of the AISI 410L-Mn-Si-N; AISI 410L-Ni-Mn-Si-N; and AISI 410L-Ni-Si-N alloy systems, prepared using laser powder cladding at a powder feed rate of 30 g/min (corresponding to Figure 4.7.2).

30 g/min Single Layers With N							
	410L + 0.45% N	410L + 1.8% Mn + 0.45% N	410L + 3.5% Mn + 0.45% N	410L + 2.5% Ni + 0.45% N	410L + 5.5% Ni + 0.45% N	410L + 1.8% Mn + 2.5% Ni + 0.45% N	410L + 3.5% Mn + 2.5% Ni + 0.45% N
Carbon (C)	0.012	0.028	0.028	0.022	0.013	0.018	0.023
Chromium (Cr)	12.6	12.1	12.1	12.1	12.0	12.1	11.9
Manganese (Mn)	0.64	3.13	5.14	0.64	0.61	3.41	5.46
Nickel (Ni)	0.18	0.18	0.18	2.49	5.14	2.4	2.65
Silicon (Si)	0.82	0.82	0.7	0.75	0.83	0.65	0.65
Nitrogen (N)	0.0811	0.0971	0.0943	0.0721	0.0801	0.0875	0.0782
Iron (Fe)	Balance	Balance	Balance	Balance	Balance	Balance	Balance

.

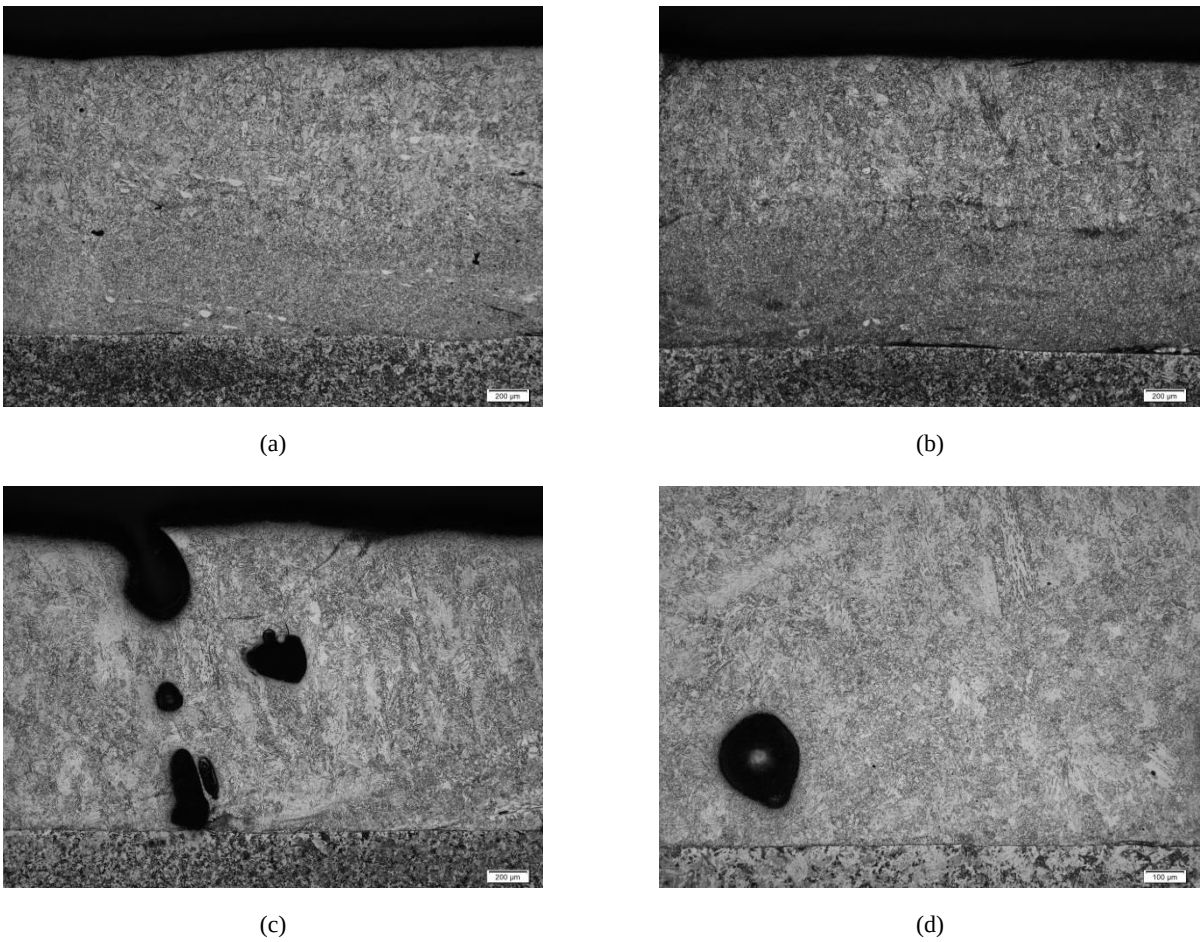

(a) (b)

(c) (d)

Figure 5.5.1. Optical micrographs showing the interface between the medium-carbon steel substrate and cladded layers of the (a) 410L-3.5Mn (deposited at a feed rate of 15g/min); (b) 410L-3.5Mn-0.45N (15 g/min); (c) 410L-1.8Mn-0.45N (30 g/min); and 410-1.8Mn-0.45N (30 g/min) (at a higher magnification), alloying systems.

In the micrographs of Figure 5.5.1, there is an absence of the typical wave-like dilution patterns between clad layers and substrate material typical of the laser cladding process, as illustrated in Figure 2.1.6. This indicates that very low penetration depths were achieved during laser cladding, leading to low, and even negligible dilution levels. The chromium values from the chemical analyses of Tables 5.5.1-5.5.4 confirm that dilution levels were extremely low as they were fairly consistent at an average of about 12.3% Cr, which does not deviate far from the original Cr content of the 410L powder given in Table 4.2.1 as 12.1% Cr. If calibration of the measuring equipment is taken into account, the difference between the average of the analysed values and the original analysis of Table 4.2.1 also becomes negligible. Further dilution would have resulted in a chromium level below that required for passivity in a stainless steel.

5.6 LASER PARAMETER OPTIMISATION FOR THE CLADDING OF AISI 410L-Si-N ALLOYS

The laser parameters used to deposit the clad layers described in sections 5.2 and 5.4 were not optimised with regards to clad dimensions, dilution levels or surface appearance. Once established that martensitic structures with nitrogen levels of 0.08 wt% and above could be obtained using modified AISI 410L powders,

an attempt was made to optimise the laser parameters and gain an understanding of the influence of various process parameters on the deposit quality. To this effect Si_3N_4 powder was added to the AISI 410L powder feed (yielding a calculated maximum nitrogen content of 0.4 wt%) and variations in dilution, clad height, bead width and porosity content were studied as a function of laser power, powder feed rate and cladding speed for single- and multi-layer deposits. The repeatability of the parameter optimisation experiments is considered in more detail in Appendix A3. The results obtained for single-layer deposits were generally found to be repeatable, but a high degree of scatter was observed during the multi-layer parameter optimisation experiments.

5.6.1 Single-track parameter optimisation

During single-track cladding, the aim is to deposit a single clad layer with the desired clad dimensions, quality and properties. This requires high powder feed rates to ensure the deposition of sufficient cladding material, and strict control over the level of dilution with the substrate material. Figure 5.6.1 shows the influence of measured laser power on the level of dilution for different cladding speeds at set powder feed rates. For a given powder feed rate, an increase in measured laser power typically leads to higher levels of dilution. This can be attributed to an increase in the specific energy per unit mass at higher laser powers. A larger volume of the substrate material melts at higher laser powers and dilution increases.

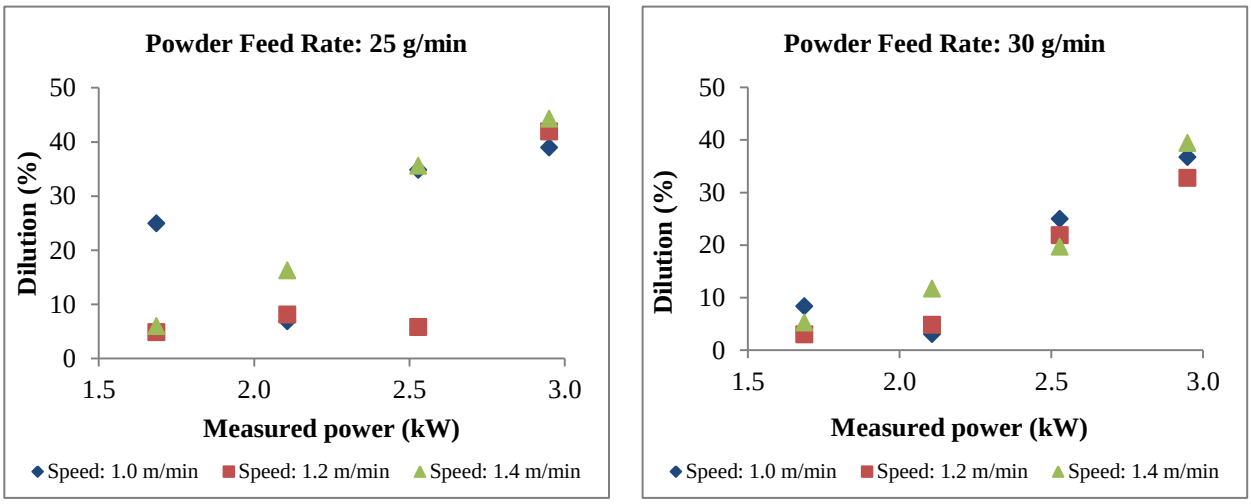

(a) (b)

Figure 5.6.1. Relationship between the dilution levels (%) of single-track deposits and measured laser power (kW) for different cladding speeds (m/min) at powder feed rates of: (a) 25 g/min; and (b) 30 g/min.

Figure 5.6.2 shows the influence of powder feed rate on the level of dilution for different cladding speeds at four laser power settings. In (a) – (d) of Figure 5.62, the level of dilution tends to decrease with an increase in powder feed rate. The laser power is increasingly consumed by powder entering the melt pool as the powder feed rate increases. This reduces the specific energy per unit mass available to melt the substrate material, resulting in lower dilution levels. These results are in good agreement with the findings of Qian *et al.* [8] and Pelletier and Sahour [9] who reported a reduction in percentage dilution with an increase in powder feed rate during laser cladding.

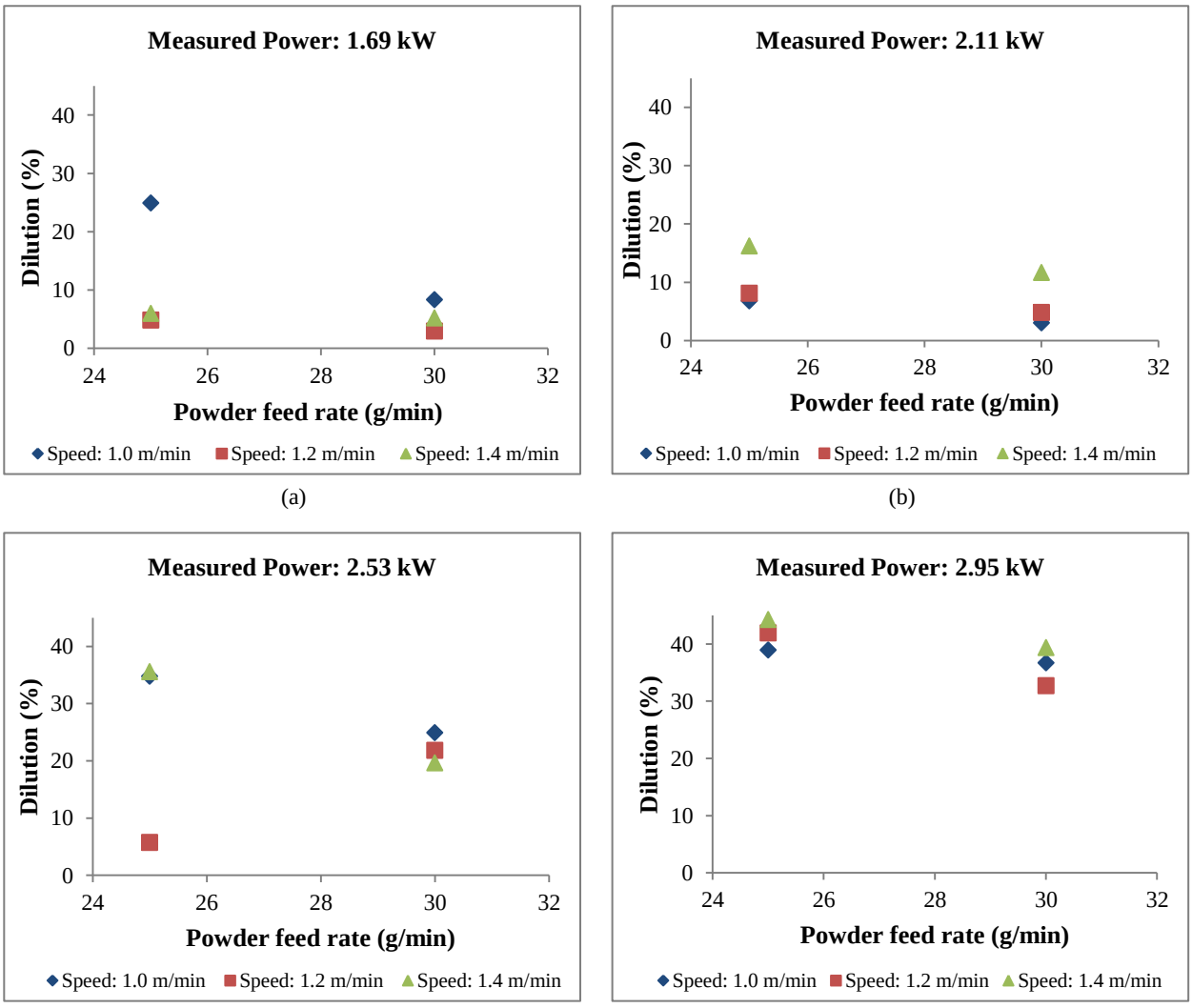

Figure 5.6.2. Relationship between the dilution levels (%) of single-track deposits and powder feed rate (g/min) for different cladding speeds (m/min) at measured laser power levels of: (a) 1.69 kW; (b) 2.11 kW; (c) 2.53 kW; and (d) 2.95 kW.

Figure 5.6.3 shows the influence of cladding speed on dilution for different measured laser powers. A marginal increase in the level of dilution is evident with an increase in cladding speed. Even though only a single parameter was changed during the experiment, complex interactions exist and the effect appears negligible. A faster cladding speed at a constant powder feed rate results in less powder being deposited per unit area. This increases the specific energy per unit mass and promotes higher levels of dilution between the powder and the substrate material. This is in agreement with the findings of Qian *et al.* [8] who concluded that dilution is more dependent on the amount of laser power absorbed by the volume of deposited powder than on the interaction time.

As shown in Figure 5.6.3, the change in dilution with cladding speed is, however, almost negligible within the range investigated, suggesting that the interaction time between the laser beam and the substrate may have played a more important role than proposed by Qian *et al.* [8]. These results suggest that dilution can be

controlled to a small extent in single-layer deposits by increasing the powder feed rate and reducing the laser power, provided the desired clad dimensions and quality are attained and the powder is adequately melted and fused to the substrate.

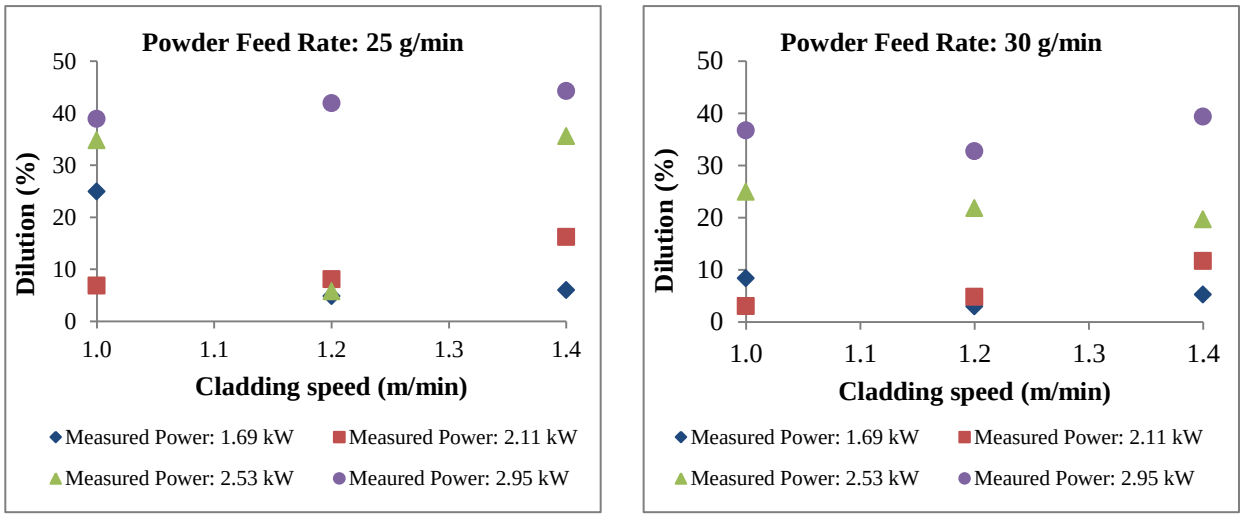

(a) (b)

Figure 5.6.3. Relationship between the dilution levels (%) of single-track deposits and cladding speed (m/min) for different laser power levels (kW) at powder feed rates of: (a) 25 g/min; and (b) 30 g/min.

Figure 5.6.4 shows the influence of measured laser power on the clad height of single-track deposits for different cladding speeds. It is evident that the clad height increases with an increase in the measured laser power at a constant powder feed rate. This can be attributed to an increase in powder efficiency (i.e. the ratio between the amount of powder melted by the laser beam to the amount of powder delivered by the powder feeder) as the laser power increases. More heat is available at higher power levels and the laser beam therefore melts more powder during laser cladding. This results in an increase in the clad height of the deposit.

Cladding speed appears to play an important role in determining clad height, with faster cladding speeds leading to reduced clad heights. This is confirmed by Figure 5.6.5, which highlights the influence of cladding speed on the clad height of single-track deposits for four different laser power settings at a constant powder feed rate. The decrease in clad height with an increase in cladding speed can be attributed to the lower volume of powder delivered per substrate unit area. Less powder is melted and therefore increasing cladding speeds also leads to increased dilution, as shown earlier in Figure 5.6.3.

Figure 5.6.6 shows the influence of powder feed rate on the clad height of single-track deposits for different cladding speeds at four laser powers. As the feed rate increases, the clad height also increases. Additional laser energy is consumed by the higher volume of powder entering the laser beam, resulting in an increase in clad height and a corresponding decrease in dilution, as observed in Figure 5.6.2. This is in agreement with the published findings of several authors [9-12].

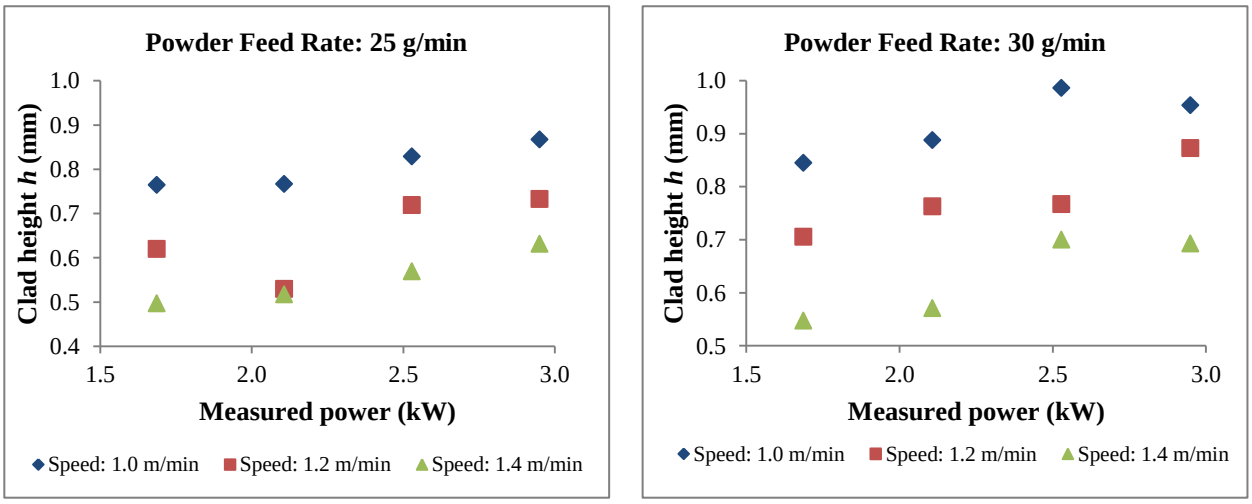

(a) (b)

Figure 5.6.4. Relationship between the clad height *h* (mm) of single-track deposits and measured laser power (kW) for different cladding speeds (m/min) at powder feed rates of: (a) 25 g/min; and (b) 30 g/min.

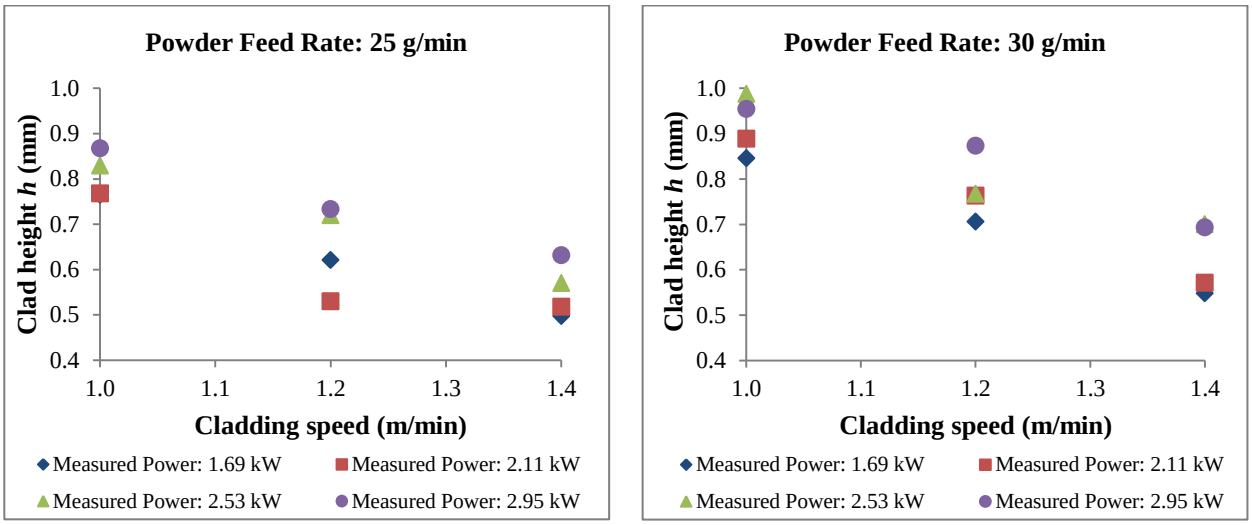

(a) (b)

Figure 5.6.5. Relationship between clad height *h* (mm) of single-track deposits and cladding speed (m/min) for different laser power levels (kW) and powder feed rates of: (a) 25 g/min; and (b) 30 g/min.

Figure 5.6.7 shows the influence of the combined parameter *F*/*S* (g/m), which represents the powder deposition rate (powder feed rate/cladding speed), on the clad height of single-track deposits for different laser power levels. An increase in the parameter *F*/*S*, corresponding to either an increase in the powder feed rate or a decrease in the cladding speed, consistently increases the clad height of the deposit. This is in agreement with the findings of De Oliveira *et al.* [12] and confirms that the parameter *F*/*S* provides a useful way of characterising the effect of powder feed rate and cladding speed on the clad height of deposited layers during laser cladding.

Laser cladding parameters also affect the width of the clad layer. Figure 5.6.8 shows the influence of laser power on the width of single-track deposits for different cladding speeds at fixed powder feed rates. The width of the deposits appears to increase with an increase in measured laser power. This can be attributed to an increase in specific energy per unit mass, resulting in higher powder efficiencies. At a set powder feed

rate, the increase in temperature associated with an increase in laser power causes a higher volume fraction of the powder entering the laser beam to melt and a wider clad layer develops. The formation of a wider clad bead is also facilitated by an increase in the wettability of the molten deposit (or a decrease in viscosity) as the laser power increases. This agrees with the findings of de Oliveira *et al.* [12] and suggests that the width of a single-track deposit is dependent on more variables than the laser spot size alone, as put forward by Chryssolouris *et al.* [10].

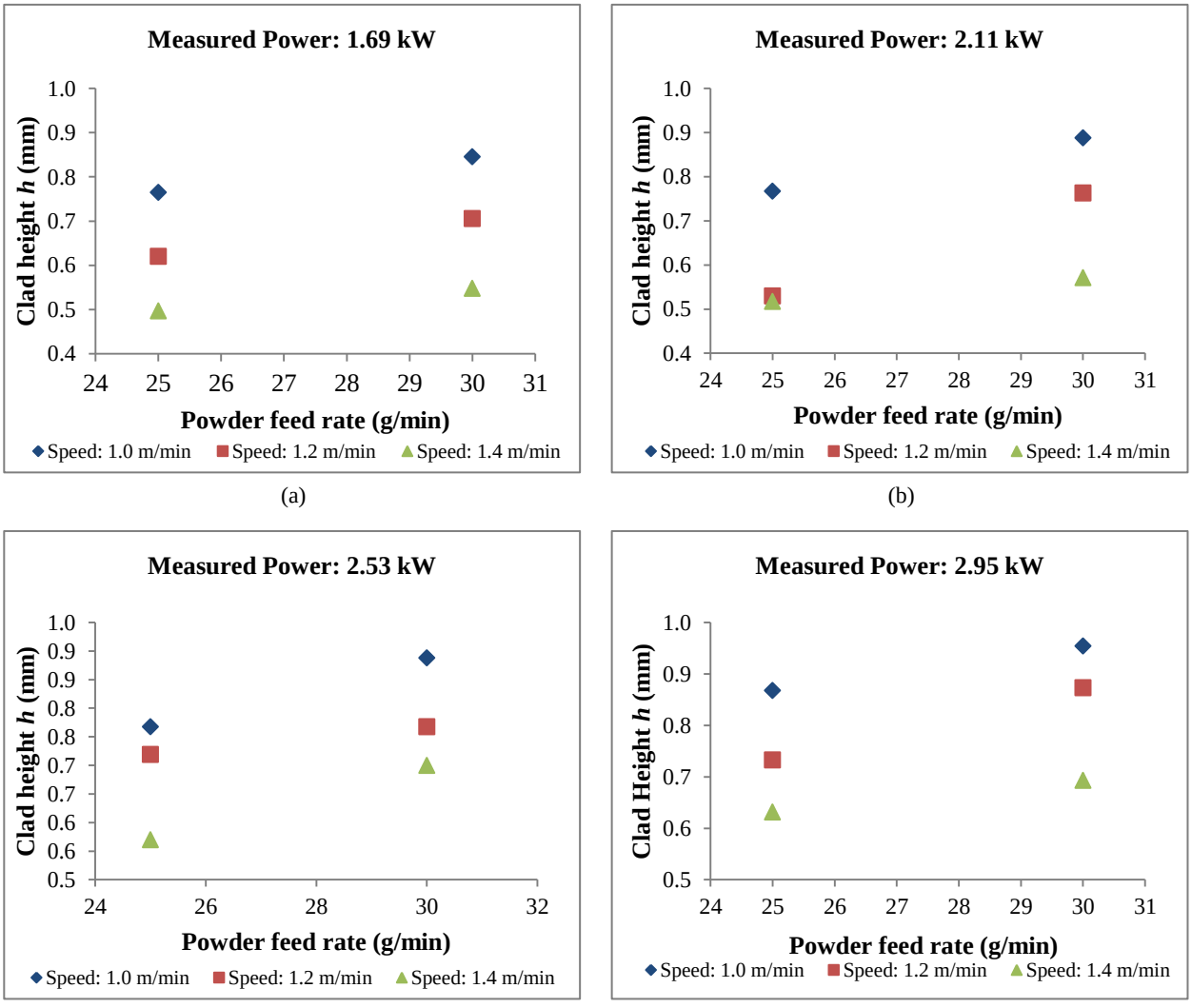

Figure 5.6.6. Relationship between clad height *h* (mm) of single-track deposits and powder feed rate (g/min) for different cladding speeds at measured laser power levels of: (a) 1.69 kW; (b) 2.11 kW; (c) 2.53 kW; and (d) 2.95 kW.

Figure 5.6.9 shows the influence of cladding speed on the width of a single-track deposit at set powder feed rates for different laser power settings. The clad width tends to decrease slightly with an increase in cladding speed. At a given powder feed rate, this can be attributed to a reduction in the amount of powder deposited per unit area and a decrease in the wetting characteristics of the deposit as the cladding speed increases [13]. The influence of cladding speed on clad width is, however, so small that it can safely be ignored during the planning of laser cladding operations, suggesting that optimisation of the cladding speed should rather be focused on achieving the desired clad height and level of dilution.

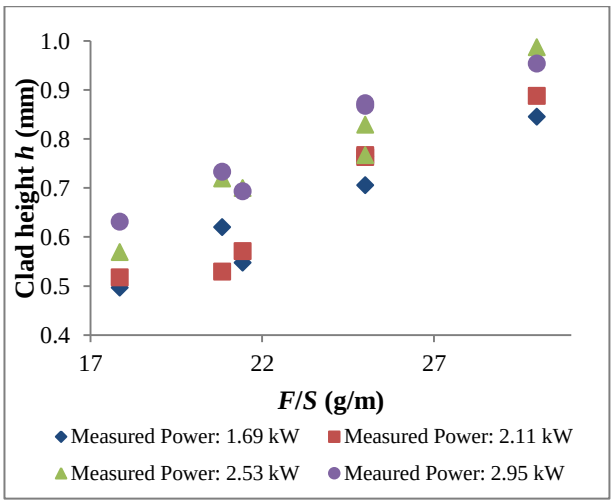

Figure 5.6.7. Relationship between clad height *h* (mm) of single-track deposits and the combined parameter *F*/*S* (g/m) for four different laser power levels (kW) during cladding.

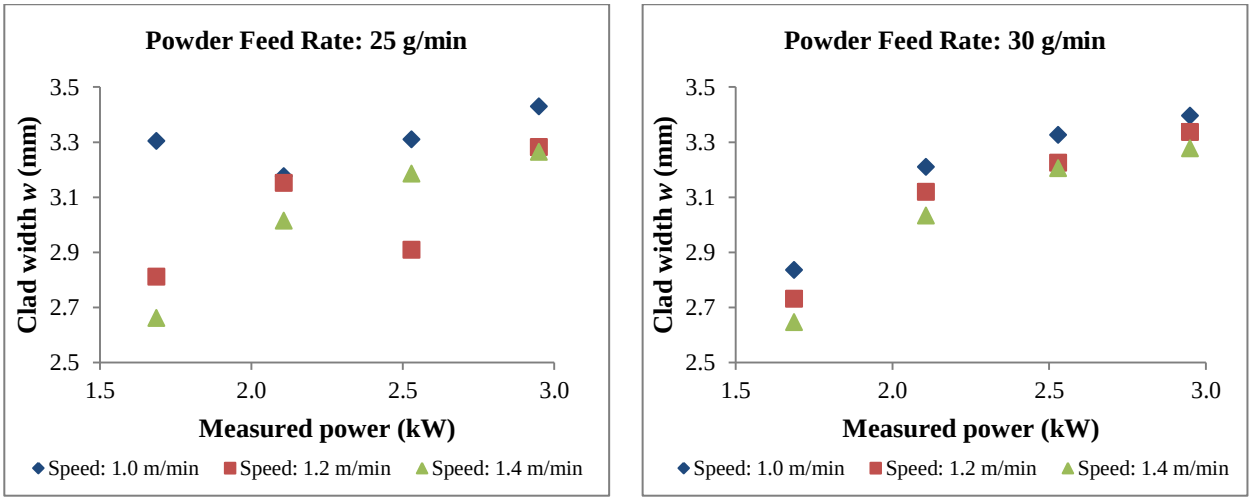

(a) (b)

Figure 5.6.8. Relationship between clad width *w* (mm) of single-track deposits and measured laser power (kW) for different cladding speeds at powder feed rates of: (a) 25 g/min; and (b) 30 g/min.

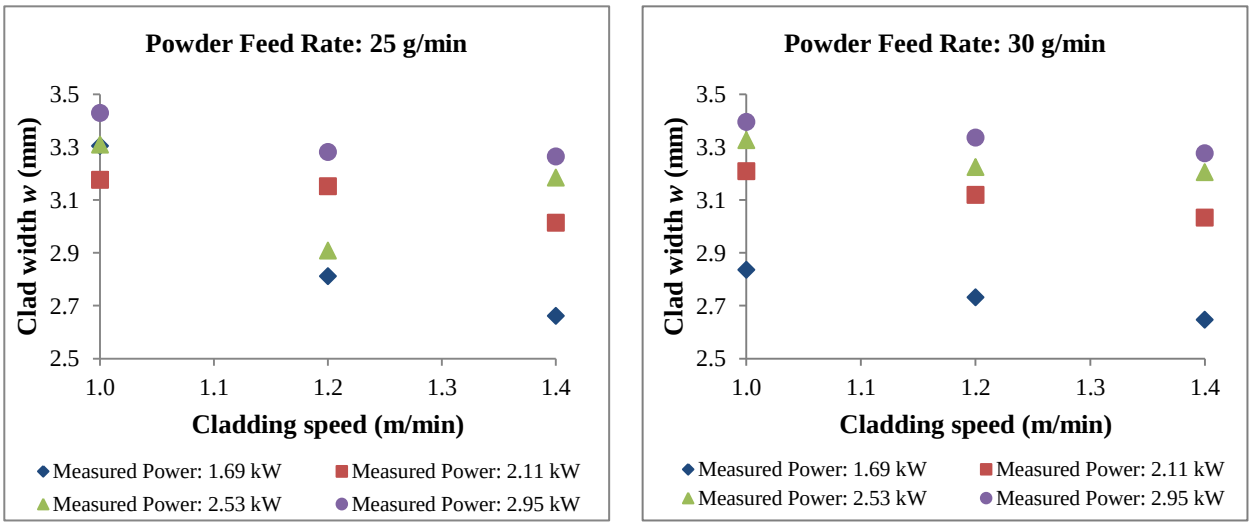

(a) (b)

Figure 5.6.9. Relationship between clad width *w* (mm) of single-track deposits and cladding speed (m/min) for different laser power levels (kW) at powder feed rates of: (a) 25 g/min; and (b) 30 g/min.

Figure 5.6.10 shows the influence of the combined parameter $P/S^{1/2}$ ($Ws^{1/2}mm^{-1/2}$) on clad width for different powder feed rates, where P represents the laser power and S the cladding speed. With an increase in the parameter $P/S^{1/2}$, corresponding to either an increase in laser power or a decrease in cladding speed, the clad width increases. This agrees with the findings of De Oliveira *et al.* [12] who originally proposed the combined parameter to describe the influence of cladding parameters on the width of the deposit.

5.6.2 Multi-track parameter optimisation

During multi-track parameter optimisation, the decision was taken not to consider the influence of laser cladding parameters on dilution and clad dimensions. This decision was based on the findings of Sun *et al.* [11] who demonstrated linear increases in the clad height and dilution levels of multi-track deposits with increases in the clad height and dilution levels of the individual clad layers making up the composite clad deposit. The conclusions drawn from single-track deposits, described in section 5.6.1, therefore similarly apply to multi-track deposits.

On the other hand, in multi-layered deposits the properties and composition of the first clad layer will be strongly affected by dilution with the substrate material, but subsequent layers are likely to be more highly alloyed and closer in composition to the modified AISI 410L powders used. Nitrogen pick-up from underlying layers may result in higher melt nitrogen contents and the risk of nitrogen degassing is therefore higher during multi-layer cladding. For this reason multi-track parameter optimisation focused on reducing the volume percentage porosity observed in multi-layer AISI 410L-Si-N deposits, rather than optimising clad dimensions. Si_3N_4 powder was added to the AISI 410L powder feed (yielding a calculated maximum nitrogen content of 0.4 wt%) and variations in porosity content were examined as a function of laser power, powder feed rate and cladding speed.

Figure 5.6.11 shows the influence of measured laser power on the observed volume percentage porosity in multi-track deposits for different cladding speeds at set powder feed rates. Cladding at a laser power of 1.69 kW resulted in discontinuous beads for a powder feed rate of 30 g/min and the results are therefore not included in Figure 5.6.11.

The amount of porosity generally increased with an increase in laser power. The nitrogen content of these clad layers exceeded the nitrogen solubility limit in the solid state and, as discussed in section 5.3, nitrogen was rejected to the liquid phase during solidification. On cooling nitrogen desorption occurred through N_2 bubble formation. The increase in porosity at higher laser powers can be attributed to higher levels of dilution with the underlying nitrogen-enriched clad layers and higher clad heights (as shown in Figure 5.4.5). An increase in clad height increases the risk of porosity by increasing the distance that nucleated nitrogen bubbles must travel to reach the clad surface. If these nitrogen bubbles are trapped by the advancing solidification front, the clad layer will contain gas porosity. This can be offset to some extent by the increase in specific energy per unit mass at higher laser powers, which results in a longer thermal cycle that allows more time for nitrogen bubbles to escape.

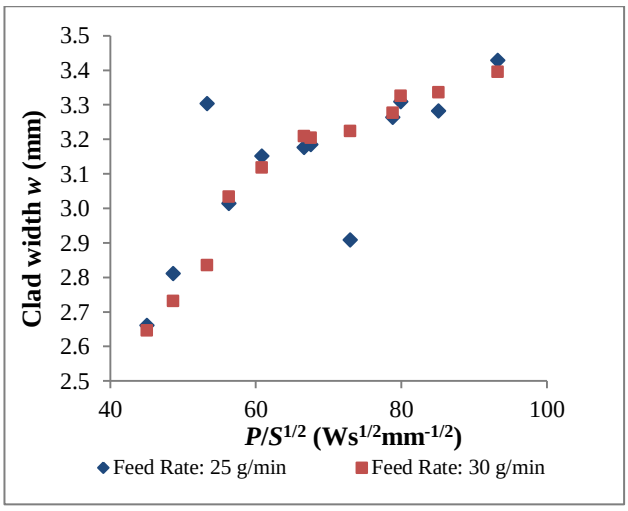

Figure 5.6.10. Relationship between clad width *w* (mm) of single-track deposits and the combined parameter $P/S^{1/2}$ ($Ws^{1/2}mm^{-1/2}$) for four different laser power levels (kW) during laser cladding.

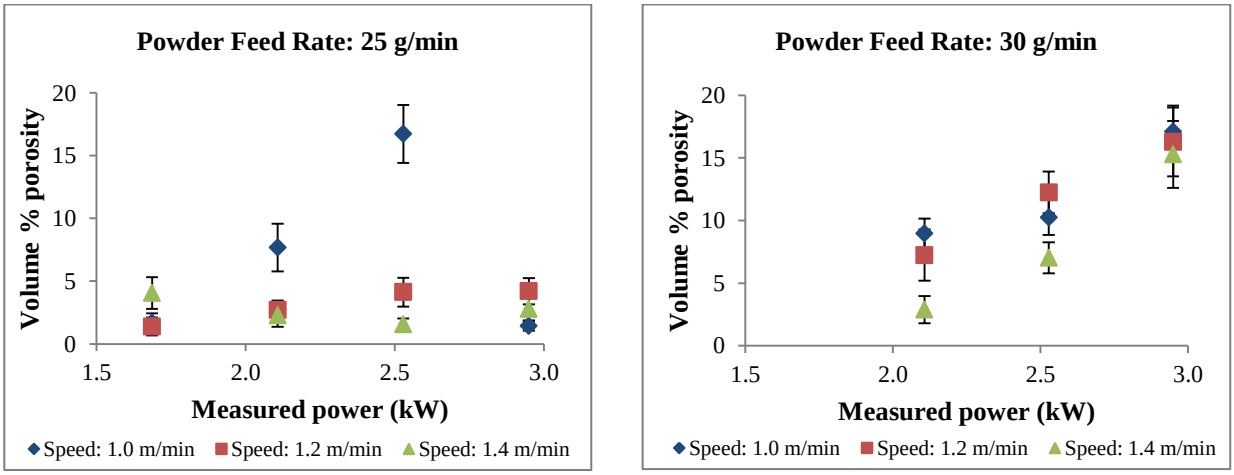

(a) (b)

Figure 5.6.11. Relationship between observed volume % porosity in multi-track deposits and the measured laser power (kW) for different cladding speeds at powder feed rates of: (a) 25 g/min; and (b) 30 g/min.

Figures 5.6.12 and 5.6.13 show the influence of powder feed rate and cladding speed on the observed volume percentage porosity in multi-track deposits. Although a clear trend is not always evident, the amount of porosity appears to increase with an increase in the powder feed rate, and to decrease with an increase in cladding speed. This is consistent with the observed influence of these parameters on the clad height. As shown in Figures 5.6.5 and 5.6.6, the clad height increases as the powder feed rate increases (at a constant cladding speed). At a constant powder feed rate, the clad height increases with a reduction in cladding speed. As explained earlier, this raises the risk of entrapment of nitrogen bubbles by the advancing solidification front.

Figure 5.6.14 shows the influence of the combined parameter *F*/*S* (or the deposition rate) on the observed percentage porosity in the clad layers. Although considerable scatter is evident, an increase in *F*/*S* appears to promote the formation of more porosity in the clad layers. This corresponds well with the reported relationship between *F*/*S* and the clad height, as shown in Figure 5.6.7. This confirms the link between

volume percentage porosity and clad height and highlights the importance of controlling the deposition rate during laser cladding.

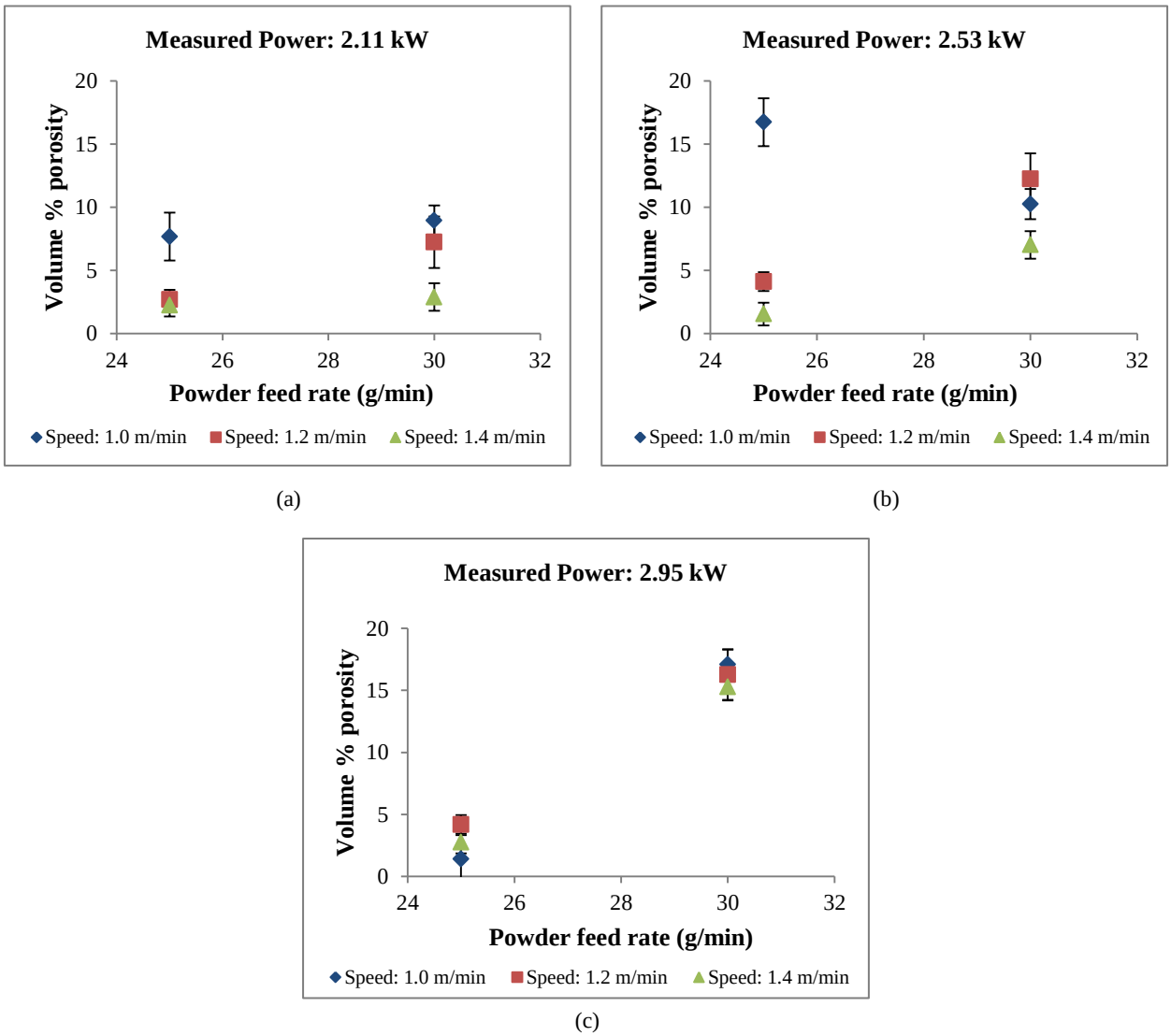

Figure 5.6.12. Relationship between observed volume % porosity in multi-track deposits and the powder feed rate (g/min) for different cladding speeds at measured laser power levels of: (a) 2.11 kW; (b) 2.53 kW; and (c) 2.95 kW.

As described in section 2.1.4, Sexton and Byrne [14] reported that the aspect ratio *w*/*h* (clad width/clad height) of the clad deposit is important, especially in the case of interbead porosity. In this type of porosity, bubbles are trapped between overlapping beads and are not always the product of gas evolution from a chemical reaction.

Interbead porosity is most often observed when the aspect ratio of an individual bead is less than or equal to five, i.e. $w/h \leq 5$. Figure 5.6.15 shows the influence of the aspect ratio *w*/*h* of individual deposits on the observed percentage porosity in multi-track deposits. Although no immediate trend is apparent, a shift in the general observed porosity behaviour seems to occur at *w*/*h* values of around 5. Below this threshold, porosity contents are widely scattered as both interbead porosity and pores due to N_2 gas evolution occur. Above the threshold value, the observed percentage porosity seems to be confined to a smaller range of values, attributable only to N_2 gas evolution.

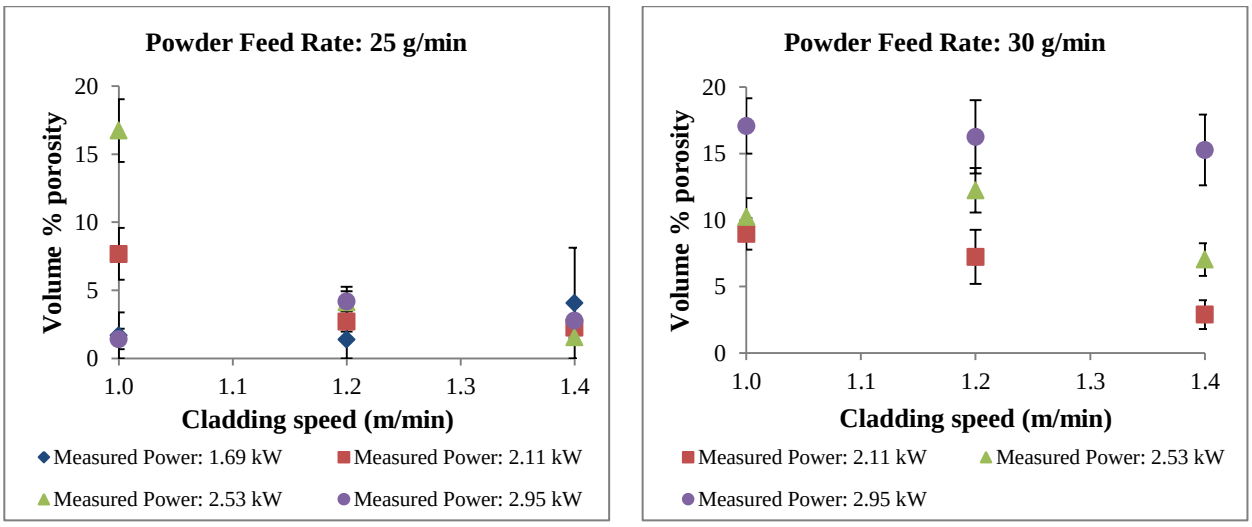

(a) (b)

Figure 5.6.13. Relationship between observed volume % porosity in multi-track deposits and the cladding speed (m/min) for different laser power levels (kW) at powder feed rates of: (a) 25 g/min; and (b) 30 g/min.

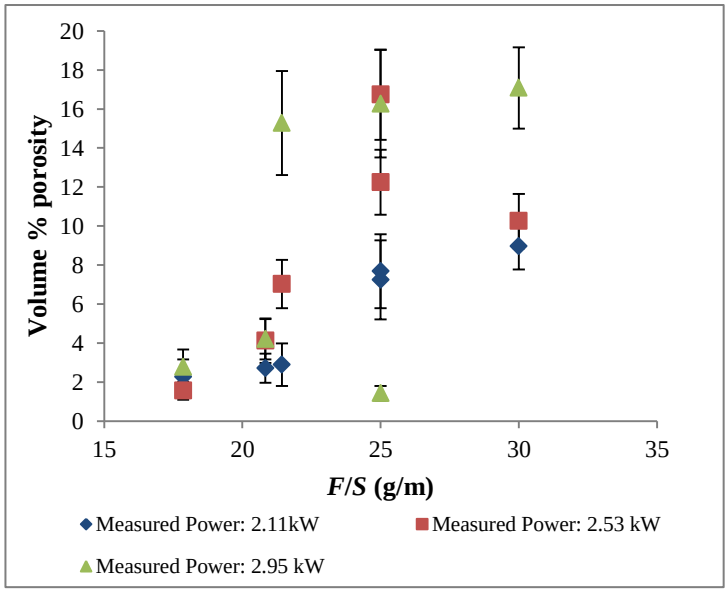

Figure 5.6.14. Relationship between observed volume % porosity in multi-track deposits and the combined parameter *F*/*S* (g/m) at four different laser power levels (kW) during cladding.

Figure 5.6.16 shows examples of bead surfaces to illustrate the influence of aspect ratio *w*/*h* on the observed porosity after laser cladding. Table 5.6.1 shows the laser parameters and process variables used to produce these deposits. Figure 5.6.16(a) shows the surface of a deposit with an aspect ratio of 5.9 (above the threshold value). Little porosity is evident. Figure 5.6.16(b) shows the surface of a deposit with an aspect ratio of 4.2 (below the threshold value). Severe interbead porosity is evident.

Interbead porosity may be augmented by N_2 gas evolution through nitrogen build-up in the interbead regions between successive beads during laser cladding with nitrogen-alloyed material. The first nitrogen-containing bead in a multi-track deposit only experiences dilution with the substrate material, which in this case is a

medium-carbon steel with low residual nitrogen content. With 50% overlap, consecutive beads experience dilution with the substrate material and half of the first bead, as shown schematically in Figure 5.6.17.

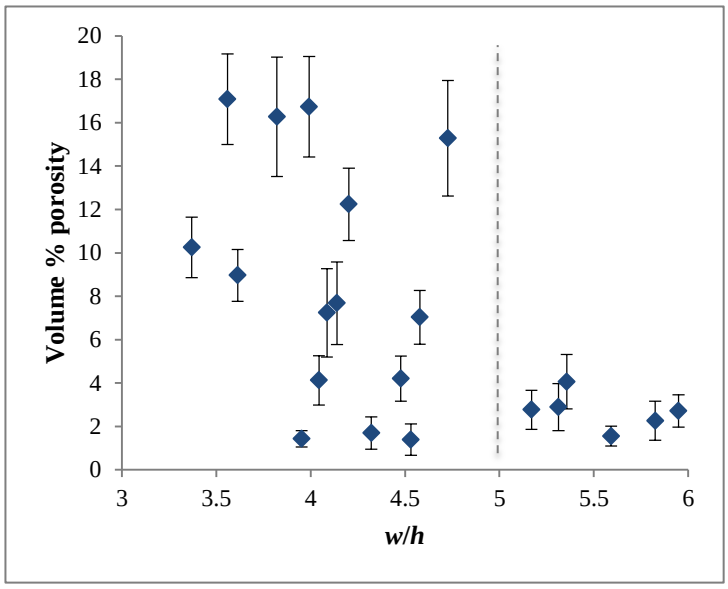

Figure 5.6.15. Relationship between observed % porosity in multi-track deposits and the aspect ratio *w*/*h* of individual beads during laser cladding.

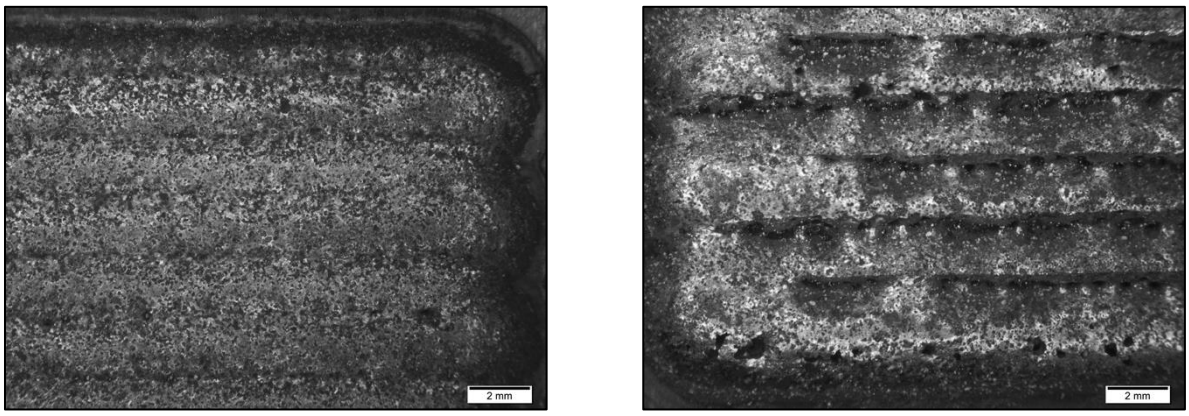

(a) (b)

Figure 5.6.16. Influence of aspect ratio *w*/*h* on porosity observed on the surfaces of AISI 410L-Si-N alloys (for a theoretical nitrogen content of 0.4 wt%) for: (a) *w*/*h* > 5; and (b) *w*/*h* < 5.

Since the nitrogen-alloyed clad layers have higher nitrogen contents than the substrate material, subsequent beads will have higher nitrogen levels than the first bead, especially in the interbead regions where the effect of dilution with the substrate material is minimised. The nitrogen solubility limit is exceeded to a greater extent in these interbead areas and higher volume percentages porosity are observed. This is illustrated in Figures 5.6.18(a) and (b). Little porosity is evident in the interbead regions of the first run, but during multi-track cladding, interbead porosity is increasingly observed between successive beads. This effect is even more pronounced in multi-layer deposits. Once the first layer had been deposited, subsequent layers are diluted not only with nitrogen-containing cladding material, but also with the underlying nitrogen-alloyed layer. This leads to more nitrogen pick-up and a higher risk of porosity.

Table 5.6.1. Laser parameters and process variables for clad deposits with aspect ratios greater than 5 and less than 5, corresponding to the surface images of Figure 5.6.16.

Parameter	$w/h > 5$	$w/h < 5$
Measured laser power (kW)	2.11	2.53
Cladding speed (m/min)	1.2	1.2
Powder feed rate (g/min)	25	30
Deposition rate (g/m)	21	25
Clad height (mm)	0.53	0.77
Aspect ratio w/h	5.9	4.2
Volume % porosity observed	2.7	12.2

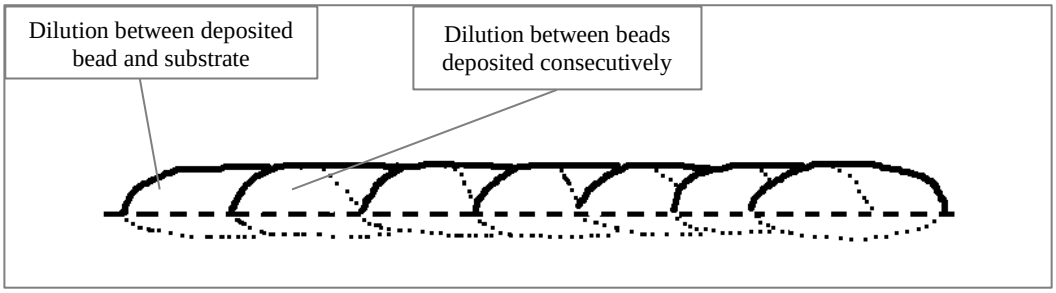

Figure 5.6.17. Schematic illustration of dilution between the initial bead and the substrate material, and dilution between consecutively deposited beads in multi-track laser cladding.

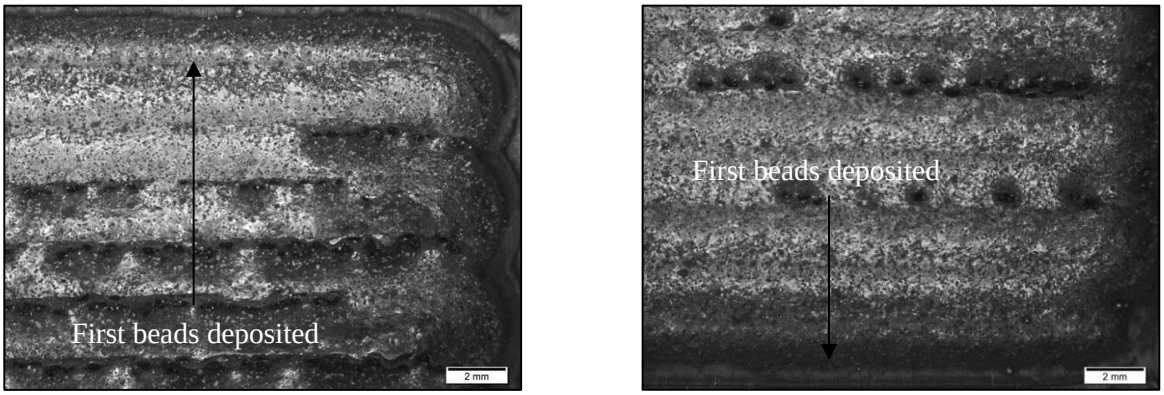

(a) (b)

Figure 5.6.18. Surfaces of multi-track deposits showing little evidence of interbead porosity in the first beads, and increasing interbead porosity in successive runs, for aspect ratios of: (a) 4.2; and (b) 3.6.

5.7 REFERENCES

[1] Kemp, M. Van Bennekom, A., Robinson, F.P.A. *Evaluation of the corrosion and mechanical properties of a range of experimental Cr-Mn stainless steels.* Materials Science and Engineering A, vol. 199, no. 2. 1995. pp. 183-194.

[2] Huang, C.-C., Tsai, W.-T., Lee, J.-T. *Laser surface alloying of carbon steel with Fe-Cr-Si_3N_4 powders.* Scripta Metallurgica et Materialia, vol. 30, no. 11. 1994. pp. 1461-1466.

[3] Huang, C.-C., Tsai, W.-T., Lee, J.-T. *Effects of N and Mo on the electrochemical behavior of laser-alloyed stainless steels in a 3.5 wt.% NaCl solution.* Materials Chemistry and Physics, vol. 42, no. 4. 1995. pp. 280-284.

[4] Huang, C.-C., Tsai, W.-T., Lee, J.-T. *Microstructure and electrochemical behavior of laser treated Fe-Cr and Fe-Cr-Si-N surface alloyed layers on carbon steel.* Materials Science and Engineering A, vol. 190, no. 1-2. 1995. pp. 199-205.

[5] Huang, C.-C., Tsai, W.-T., Lee, J.-T. *Microstructure and electrochemical behavior of laser cladded Fe-Cr-Mo-Si-N surface alloys on carbon steel.* Materials Science and Engineering A, vol. 196, no. 1-2. 1995. pp. 243-248.

[6] Huang, C.-C., Tsai, W.-T., Lee, J.-T. *The effect of silicon nitride on the laser surface alloying with Fe-Cr-Si_3N_4 powders.* Scripta Metallurgica et Materialia, vol. 32, no. 9. 1995. pp. 1465-1470.

[7] Huang, C.-C., Tsai, W.-T., Lee, J.-T. *Surface modification of carbon steel with laser treated nitrogen-containing stainless steel layers.* Surface and Coatings Technology, vol. 79, no. 1-3. 1996. pp. 67-70.

[8] Qian, M., Lim, L.C., Chen, Z.D., Chen, W.I. *Parametric studies of laser cladding process.* Journal of Materials Processing Technology, vol. 63, no. 1-3. 1997. pp. 590-593.

[9] Pelletier, J.M., Sahour, M.C., Pilloz, M., Vannes, A.B. *Influence of processing conditions on geometrical features of laser claddings obtained by powder injection.* Journal of Materials Science, vol. 28, no. 19. 1993. pp. 5184-5188.

[10] Chryssolouris, G., Zannis, S., Tsirbas, K., Lalas, C. *An experimental investigation of laser cladding.* CIRP Annals - Manufacturing Technology, vol. 51, no. 1. 2002. pp. 145-148.

[11] Sun, S., Durandet, Y., Brandt, M. *Parametric investigation of pulsed Nd:YAG laser cladding of Stellite 6 on stainless steel.* Surface and Coatings Technology, vol. 194, no. 2-3. 2005. pp. 225-231.

[12] De Oliveira, U., Ocelík, V., De Hosson, J.Th.M. *Analysis of coaxial laser cladding processing conditions.* Surface and Coatings Technology, vol. 197, no. 2-3. 2005. pp. 127-136.

[13] Yellup, J.M. *Laser cladding using the powder blowing technique.* Surface and Coatings Technology, vol. 71, no. 2. 1995. pp. 121-128.

[14] Sexton, C.L., Byrne, G., Watkins, K.G. *Alloy development by laser cladding: An overview.* Journal of Laser Applications, vol. 13, no. 2. 2001. pp. 2-11.

CHAPTER 6

CONCLUSIONS AND RECOMMENDATIONS

6.1 CONCLUSIONS

- The results obtained during the course of this investigation confirmed that *in-situ* alloying of low-carbon AISI 410L martensitic stainless steel with nitrogen during Nd-YAG laser cladding is possible, although modification of the chemical composition of the clad deposit is required to increase the nitrogen solubility limit, to ensure fully martensitic microstructures and to prevent the formation of nitrogen-induced porosity.

- The amount of nitrogen that can be absorbed from nitrogen-rich shielding and carrier gas during Nd-YAG laser cladding is limited. Cladding in a nitrogen-rich atmosphere yielded a maximum clad nitrogen content of 0.04 wt%, only marginally higher than the nitrogen content of an AISI 410L deposit produced in argon (0.03 wt%). Published literature ascribed the poor nitrogen absorption from nitrogen-containing atmospheres during Nd-YAG laser cladding to the short thermal cycle and to suppression of plasma formation above the weld pool.

- The addition of Si_3N_4 to the AISI 410L powder feed as an alternative source for nitrogen facilitated the formation of martensitic microstructures, increased the clad nitrogen content (to a maximum of 0.064 wt% nitrogen) and raised the deposit hardness. Higher nitrogen contents in the clad deposit, however, promoted the formation of unwanted nitrogen-induced porosity. In order to successfully alloy AISI 410L stainless steel with nitrogen during laser cladding, the nitrogen solubility limit of the deposit has to be increased to suppress porosity formation.

- Thermodynamic modelling revealed that the addition of manganese to AISI 410L powder increases the nitrogen solubility limit in AISI 410L due to its negative interaction parameter with nitrogen. Although nickel is known to reduce the nitrogen solubility in stainless steel, it acts as a powerful austenite-former and enlarges the austenite phase field at the expense of δ-ferrite. Austenite has a higher solubility for nitrogen than δ-ferrite, and the presence of austenite at higher temperatures facilitates the formation of martensite in the room temperature deposit. High nickel concentrations in AISI 410L tend to alter the solidification mode from ferritic to mixed austenitic-ferritic.

- The addition of up to 3.5 wt% manganese to an AISI 410L powder feed containing Si_3N_4 significantly increased the nitrogen solubility in the deposit. A martensitic microstructure with 0.12 wt% nitrogen and a peak hardness of 410 HV could be achieved without any adverse increase in porosity in the clad layer. The clad nitrogen content easily exceeded the minimum requirement of 0.08 wt%.

- The addition of up to 5.5 wt% nickel, or combinations of nickel and manganese, to the powder feed raised the deposit nitrogen content, but not to the same extent as those deposits alloyed with manganese only. Although nickel reduces the nitrogen solubility in stainless steel, the austenite phase field expands in the presence of nickel, and the solidification mode changes from primary ferritic to austenitic-ferritic. Less nitrogen is rejected to the liquid phase on solidification, resulting in higher nitrogen contents in the room temperature deposits.

- Laser parameter optimisation revealed that the amount of dilution during single-track laser cladding is mainly influenced by the specific energy per unit mass delivered by the laser beam. The clad height is strongly influenced by the powder deposition rate, whereas the bead width is influenced by the wettability of the deposits during laser cladding. During multi-track cladding, the observed percentage porosity is mainly determined by the aspect ratio of the individual beads making up the clad layer, the deposition rate and the clad height. High deposition rates result in thicker deposited layers, effectively increasing the distance that N_2 gas bubbles have to travel to escape to the atmosphere, while an aspect ratio greater than five promotes interbead porosity. The results suggest that *in-situ* nitrogen alloying during laser cladding should preferably be performed at low deposition rates to ensure higher clad nitrogen contents and hardness, lower clad heights, less dilution and less porosity.

6.2 RECOMMENDATIONS FOR FUTURE WORK

This investigation examined the feasibility of *in-situ* nitrogen alloying by means of nitrogen-rich shielding and carrier gas atmospheres and Si_3N_4 additions to the stainless steel powder feed. The clad deposit can potentially also be alloyed with nitrogen using pre-nitrided stainless steel powder (this entails an additional nitriding step prior to cladding) or by mixing nitrided ferromanganese into the powder feed. Ferromanganese powder holds promise in this application as it introduces nitrogen while simultaneously increasing the deposit manganese content to raise the nitrogen solubility limit. These avenues should be investigated to identify the most optimal and cost effective method of *in-situ* nitrogen alloying.

No attempt was made during the course of this investigation to quantify the amounts of martensite, retained austenite and δ-ferrite in the clad microstructures. More detailed microstructural examination of the deposited layers was considered outside the scope of this exploratory study. Once the cladding process has been optimised, however, the deposit microstructures should be studied in more detail to determine the amounts of δ-ferrite and retained austenite after cladding. The wear properties, corrosion resistance and high temperature properties of the nitrogen-alloyed clad layers also have to be established before the process can be successfully commercialised.

APPENDIX A1 – SAMPLE CALCULATION

In order to achieve a maximum theoretical nitrogen content of **0.1 wt**%, a 100 g powder sample should contain 0.1 g nitrogen. The amount of Si_3N_4 that has to be added to a 100 g powder samples to deliver a maximum theoretical nitrogen content of 0.1 wt% can be calculated as follows:

$$n_{\mathrm{N}} = \frac{m_{\mathrm{N}}}{M_{\mathrm{N}}} = \frac{0.1\ \mathrm{g}}{14.007\ \mathrm{g/mol}}$$

$$\therefore\ n_N = 0.0071\ \mathrm{mol\ N}$$

$$n_{\mathrm{Si}} = 0.0071 \cdot \frac{3}{4} = 0.0054\ \mathrm{mol\ Si}$$

$$m_{\mathrm{Si}} = n_{\mathrm{Si}} \cdot M_{\mathrm{Si}} = (0.0054)(28.085)$$

$$m_{\mathrm{Si}} = 0.15\ \mathrm{g\ Si}$$

$$m_{\mathrm{Si_3N_4}} = m_{\mathrm{Si}} + m_N = 0.15\ \mathrm{g} + 0.1\ \mathrm{g}$$

$$\boldsymbol{m_{\mathrm{Si_3N_4}} = 0.25\ \mathrm{g}}$$

where: n_{N} and n_{Si} are the number of moles of nitrogen and silicon in a 100 g powder sample, respectively,
M_{N} and M_{Si} are the atomic weights of nitrogen and silicon,
m_{N} and m_{Si} are the number of grams of nitrogen and silicon in a 100 g powder sample, and
m_{Si3N4} is the number of grams of Si_3N_4 powder that has to be added to a 100 g powder sample to yield a maximum theoretical nitrogen content of 0.1 wt%.

To achieve a maximum theoretical deposit nitrogen content of 0.1 wt%, a 100 g powder sample should therefore consist of 99.75 g of AISI 410L powder and 0.25 g Si_3N_4 powder.

APPENDIX A2 – LASER CLADDING PARAMETERS

Table 1. Laser cladding parameters and process variables for AISI 410L single-track deposits mixed with Si_3N_4 powder to yield a theoretical nitrogen content of 0.4 wt%.

No.	Nozzle	Powder	Spot size (mm)	Measured laser power (kW)	Set laser power (kW)	Cladding speed (m/min)	Powder feed rate 410L (rpm)	Powder feed rate Si_3N_4 (rpm)	Total powder feed rate (g/min)	Shielding and carrier gas	Carrier gas flow rate (L/min)	Shielding gas flow rate (L/min)	Depth of penetration *b* (µm)	Clad height *h* (µm)	Clad width *w* (µm)	Dilution (%)
1	Discontinuous co-axial	410 + Si_3N_4	4	1.69	20	1.0	7.7	1.5	25	N_2	3	5	253.9	764.5	3303.9	24.9
2	Discontinuous co-axial	410 + Si_3N_4	4	2.11	2.5	1.0	7.7	1.5	25	N_2	3	5	56.3	767.3	3176.2	6.8
3	Discontinuous co-axial	410 + Si_3N_4	4	2.53	3.0	1.0	7.7	1.5	25	N_2	3	5	442.0	829.1	3309.4	34.8
4	Discontinuous co-axial	410 + Si_3N_4	4	2.95	3.5	1.0	7.7	1.5	25	N_2	3	5	553.2	867.5	3428.8	38.9
5	Discontinuous co-axial	410 + Si_3N_4	4	1.69	2.0	1.2	7.7	1.5	25	N_2	3	5	31.6	620.4	2811.1	4.8
6	Discontinuous co-axial	410 + Si_3N_4	4	2.11	2.5	1.2	7.7	1.5	25	N_2	3	5	46.7	529.8	3151.5	8.1
7	Discontinuous co-axial	410 + Si_3N_4	4	2.53	3.0	1.2	7.7	1.5	25	N_2	3	5	43.9	719.3	2908.6	5.8
8	Discontinuous co-axial	410 + Si_3N_4	4	2.95	3.5	1.2	7.7	1.5	25	N_2	3	5	529.1	733.0	3281.9	41.9
9	Discontinuous co-axial	410 + Si_3N_4	4	1.69	2.0	1.4	7.7	1.5	25	N_2	3	5	31.6	496.9	2661.5	6.0
10	Discontinuous co-axial	410 + Si_3N_4	4	2.11	2.5	1.4	7.7	1.5	25	N_2	3	5	100.2	517.5	3014.2	16.2
11	Discontinuous co-axial	410 + Si_3N_4	4	2.53	3.0	1.4	7.7	1.5	25	N_2	3	5	314.7	569.6	3185.0	35.6
12	Discontinuous co-axial	410 + Si_3N_4	4	2.95	3.5	1.4	7.7	1.5	25	N_2	3	5	501.0	631.4	3264.1	44.2
13	Discontinuous co-axial	410 + Si_3N_4	4	1.69	2.0	1.0	9.3	1.8	30	N_2	3	5	76.9	845.5	2835.8	8.3
14	Discontinuous co-axial	410 + Si_3N_4	4	2.11	2.5	1.0	9.3	1.8	30	N_2	3	5	27.8	888.1	3209.2	3.0
15	Discontinuous co-axial	410 + Si_3N_4	4	2.53	3.0	1.0	9.3	1.8	30	N_2	3	5	328.1	986.9	3325.8	24.9
16	Discontinuous co-axial	410 + Si_3N_4	4	2.95	3.5	1.0	9.3	1.8	30	N_2	3	5	553.2	954.0	3395.8	36.7
17	Discontinuous co-axial	410 + Si_3N_4	4	1.69	2.0	1.2	9.3	1.8	30	N_2	3	5	21.7	705.5	2731.5	3.0
18	Discontinuous co-axial	410 + Si_3N_4	4	2.11	2.5	1.2	9.3	1.8	30	N_2	3	5	38.4	763.2	3118.6	4.8
19	Discontinuous co-axial	410 + Si_3N_4	4	2.53	3.0	1.2	9.3	1.8	30	N_2	3	5	214.1	767.3	3224.3	21.8
20	Discontinuous co-axial	410 + Si_3N_4	4	2.95	3.5	1.2	9.3	1.8	30	N_2	3	5	424.5	873.0	3336.3	32.7
21	Discontinuous co-axial	410 + Si_3N_4	4	1.69	2.0	1.4	9.3	1.8	30	N_2	3	5	30.1	547. 7	2646.4	5.2
22	Discontinuous co-axial	410 + Si_3N_4	4	2.11	2.5	1.4	9.3	1.8	30	N_2	3	5	75.5	571.0	3033.5	11.7
23	Discontinuous co-axial	410 + Si_3N_4	4	2.53	3.0	1.4	9.3	1.8	30	N_2	3	5	171.2	700.0	3204.8	19.7
24	Discontinuous co-axial	410 + Si_3N_4	4	2.95	3.5	1.4	9.3	1.8	30	N_2	3	5	450.2	693.2	3276.4	39.4

Table 2. Laser cladding parameters and process variables for AISI 410L multi-track deposits mixed with Si_3N_4 powder to yield a theoretical nitrogen content of 0.4 wt%.

No.	Nozzle	Powder	Spot size (mm)	Measured laser power (kW)	Set laser power (kW)	Cladding speed (m/min)	Powder feed rate 410L (rpm)	Powder feed rate Si_3N_4 (rpm)	Total powder feed rate (g/min)	Shielding and carrier gas	Carrier gas flow rate (L/min)	Shielding gas flow rate (L/min)	Average volume % porosity observed	95% confidence interval
1	Discontinuous co-axial	410 + Si_3N_4	4	1.69	20	1.0	7.7	1.5	25	N_2	3	5	1.7	1.5
2	Discontinuous co-axial	410 + Si_3N_4	4	2.11	2.5	1.0	7.7	1.5	25	N_2	3	5	7.7	3.8
3	Discontinuous co-axial	410 + Si_3N_4	4	2.53	3.0	1.0	7.7	1.5	25	N_2	3	5	16.7	4.6
4	Discontinuous co-axial	410 + Si_3N_4	4	2.95	3.5	1.0	7.7	1.5	25	N_2	3	5	1.4	0.8
5	Discontinuous co-axial	410 + Si_3N_4	4	1.69	2.0	1.2	7.7	1.5	25	N_2	3	5	1.4	1.4
6	Discontinuous co-axial	410 + Si_3N_4	4	2.11	2.5	1.2	7.7	1.5	25	N_2	3	5	2.7	1.5
7	Discontinuous co-axial	410 + Si_3N_4	4	2.53	3.0	1.2	7.7	1.5	25	N_2	3	5	4.1	2.3
8	Discontinuous co-axial	410 + Si_3N_4	4	2.95	3.5	1.2	7.7	1.5	25	N_2	3	5	4.2	2.2
9	Discontinuous co-axial	410 + Si_3N_4	4	1.69	2.0	1.4	7.7	1.5	25	N_2	3	5	4.1	2.5
10	Discontinuous co-axial	410 + Si_3N_4	4	2.11	2.5	1.4	7.7	1.5	25	N_2	3	5	2.3	1.8
11	Discontinuous co-axial	410 + Si_3N_4	4	2.53	3.0	1.4	7.7	1.5	25	N_2	3	5	1.6	0.9
12	Discontinuous co-axial	410 + Si_3N_4	4	2.95	3.5	1.4	7.7	1.5	25	N_2	3	5	2.8	1.8
13	Discontinuous co-axial	410 + Si_3N_4	4	1.69	2.0	1.0	9.3	1.8	30	N_2	3	5	0.0	0.0
14	Discontinuous co-axial	410 + Si_3N_4	4	2.11	2.5	1.0	9.3	1.8	30	N_2	3	5	9.0	2.4
15	Discontinuous co-axial	410 + Si_3N_4	4	2.53	3.0	1.0	9.3	1.8	30	N_2	3	5	10.2	2.8
16	Discontinuous co-axial	410 + Si_3N_4	4	2.95	3.5	1.0	9.3	1.8	30	N_2	3	5	17.1	4.2
17	Discontinuous co-axial	410 + Si_3N_4	4	1.69	2.0	1.2	9.3	1.8	30	N_2	3	5	0.0	0.0
18	Discontinuous co-axial	410 + Si_3N_4	4	2.11	2.5	1.2	9.3	1.8	30	N_2	3	5	7.2	4.1
19	Discontinuous co-axial	410 + Si_3N_4	4	2.53	3.0	1.2	9.3	1.8	30	N_2	3	5	12.2	3.3
20	Discontinuous co-axial	410 + Si_3N_4	4	2.95	3.5	1.2	9.3	1.8	30	N_2	3	5	16.3	5.5
21	Discontinuous co-axial	410 + Si_3N_4	4	1.69	2.0	1.4	9.3	1.8	30	N_2	3	5	0.0	0.0
22	Discontinuous co-axial	410 + Si_3N_4	4	2.11	2.5	1.4	9.3	1.8	30	N_2	3	5	2.9	2.2
23	Discontinuous co-axial	410 + Si_3N_4	4	2.53	3.0	1.4	9.3	1.8	30	N_2	3	5	7.0	2.5
24	Discontinuous co-axial	410 + Si_3N_4	4	2.95	3.5	1.4	9.3	1.8	30	N_2	3	5	15.3	5.3

APPENDIX A3 - REPEATABILITY

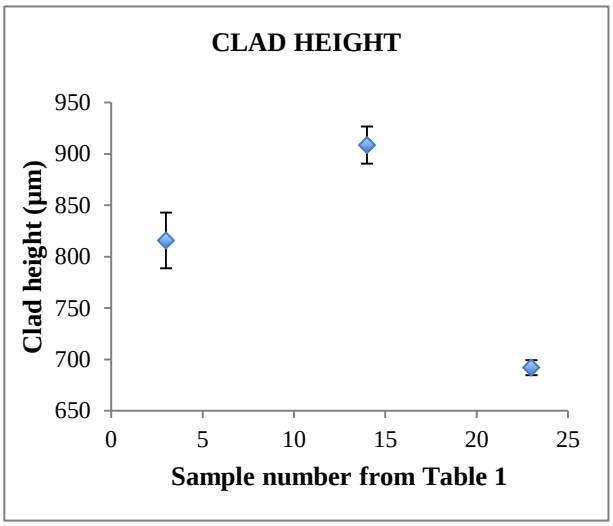

Repeatability of clad height *h*.

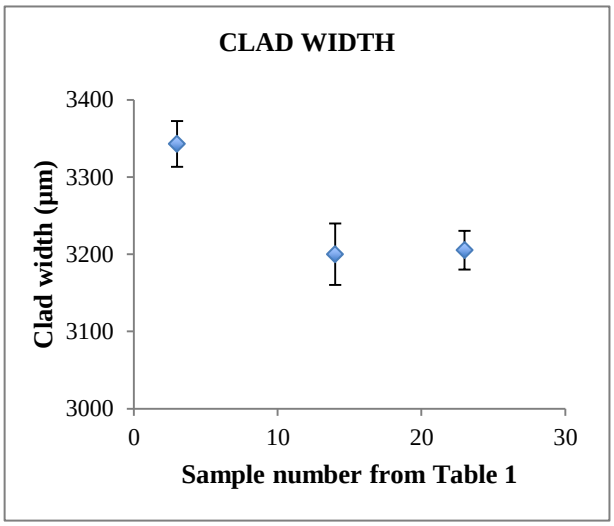

Repeatability of clad width *w*.

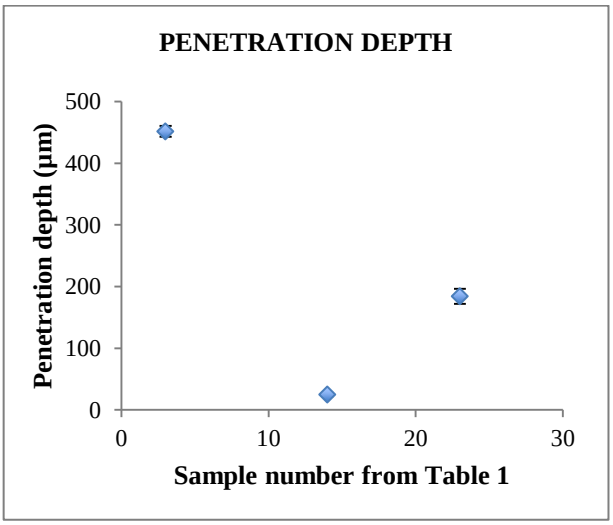

Repeatability of penetration depth *b*.

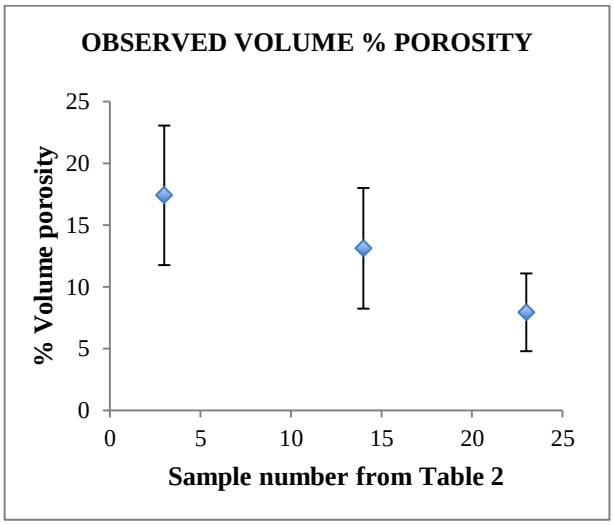

Repeatability of observed volume % porosity.

To prove repeatability of the results obtained in this study, it would have been impractical to repeat the entire factorial matrix as set out in the Experimental Procedure in Chapter 4. It was therefore decided that for each geometric variant, three different measurements would be repeated three times and the 95% confidence of each point determined. For each of the figures above, the data points shown were randomly selected from the factorial matrix from a low set of numbers, a medium set of numbers, and a high set of numbers. Three different cladded layers were produced for each data point represented in the figures above and the appropriate measurements were carried out. Where the 95% confidence intervals, or error bars, extended across a wide range, a larger variance was inherent in the results. In such cases there were considerable overlap between the confidence intervals of consecutive results and the values and trends observed in the curves, although still indicative, became less significant. For clad height, clad width, and penetration depth, there seem to be good repeatability inherent in the final results as the confidence intervals are narrow with

little overlap. In case of observed volume % porosity, the 95% confidence intervals fall within a wide range as volume % porosity is more difficult to measure accurately in the absence of x-ray techniques. This lead to large scatter in the final results.